Low-Cycle Fatigue Behavior of Welded Steel Butt-Joints

The Faculty of Engineering and Science

Design of Mechanical Systems 4. semester

Master's Thesis

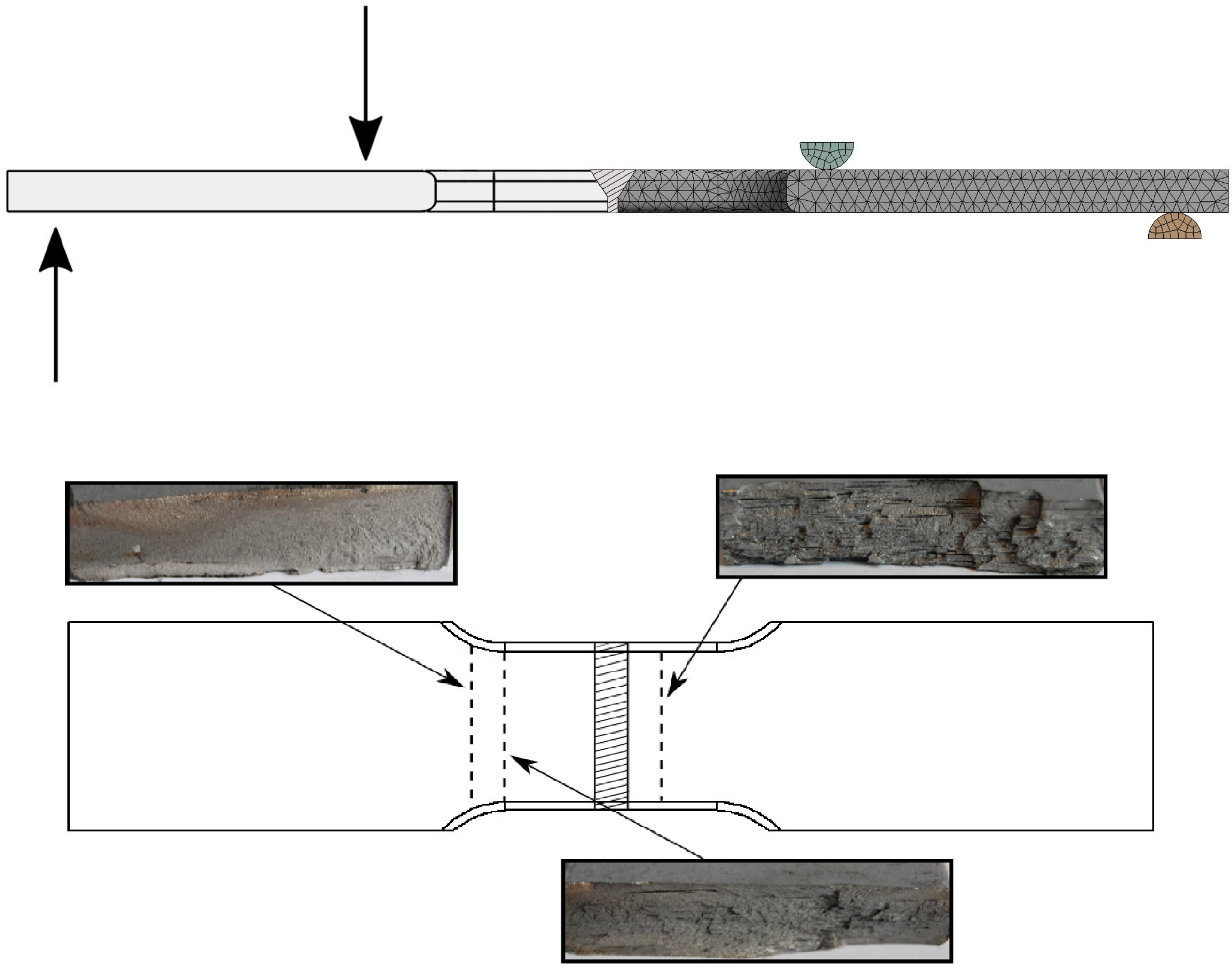

Mads Møller Christensen

Christoffer Gundersen

Jesper Søholm

AALBORG UNIVERSITET

The Faculty of Engineering and Science
Design of Mechanical Systems

Fibigerstræde 16, 9220 Aalborg Øst

Tlf. 9940 3005

Title: Low-Cycle Fatigue Behavior of Welded Steel Butt-Joints

Period of Project:
1st of February, 2019 -
3rd of July, 2019

Project Group:

Mads Møller Christensen
Christoffer Gundersen
Jesper Søholm

Supervisor:

Jan Schjødt-Thomsen

Synopsis

The objective of this project is to evaluate low-cycle fatigue life of butt-welded steel specimen. Test specimen are provided at start of the project and utilized for four point bending fatigue tests. To conduct the fatigue tests, the servo-hydraulic testing machine Schenk 400 kN at Aalborg University is utilized. The tests are set up in a fully reversed cyclic loading scenario, where $R = -1$ and no mean stress is present.
Strain gauges are attached to the specimen to validate a FE-model, which is utilized to convert the acquired displacement-life data to strain- and stress-life data. The converted data is utilized to investigate whether current fatigue models for non-welded specimen can be utilized for butt-welded specimen. This includes simple approximations for fatigue properties based on monotonic material data.
Due to difficulties with respect to geometry and provided material, new tests are deemed necessary to evaluate the LCF behavior of butt-welded steel specimen.

Report Page: 1 - 68
Appendix Page: A69 - A78
Total Page: 88
Finished: 03-06-2019

Preface

This project is a Master's Thesis, developed by three 4th semester master students of Design of Mechanical Systems, Faculty of Engineering and Science, board of Studies for Industry and Global Business Development at Aalborg University. The project addresses low-cycle fatigue behavior of butt-welded steel specimen. The object is to acquire data, which is compared to well-established fatigue models and models proposed through scientific papers. To achieve this, the following topics are addressed; low-cycle fatigue experimental work, analytic models and Finite Element methods.

Reading Guide

Throughout the report the source references will be gathered in a bibliography in the end of the report. In this report the references will be established according to the Vancouver system. This means that references will be specified with a number as [1]. This reference directs to the bibliography in which author, title, year of publication and edition or URL with a timestamp is specified. In this report tables and figures will be referred to. These are numbered according to the chapter and section in which they are used. Descriptions of the tables and figures can be found under each figure and table.

The following software are utilized in the project.

- Maple
- MatLab
- Excel
- SolidWorks
- ANSYS Workbench
- Abaqus

Mads Møller Christensen
Christoffer Gundersen
Jesper Søholm

Abstract

Dette er et afgangsprojekt af tre 4. semester studerende på kandidat uddannelsen Design af mekaniske systemer (DMS), på det ingeniør- og Naturvidenskabelige fakultet, Studienævn for Industri og Global Forretningsudvikling. Specialet omhandler en undersøgelse af udmattelsesevnerne hos stumpsømssvejste emner, hvor fokus er inden for lav-cyklus udmattelse, betegnet som "Low-cycle fatigue" på engelsk. Emnerne har typisk en levetid mellem $N = 1$ cyklus til $N = 10^4$. For at undersøge levetiden af de svejste emner i dette område er der anvendt en række ingenørmæssige værktøjer, hvilket gælder Finite Element Method, analytiske modeller, samt evaluering af eksperimentielt data, hvor der tages højde for standard afvigelser.

Projektet udspringer af tidligere studerende fra Aalborg Universitets arbejde, som ikke nåede at teste emnerne. Grundet dette er nogle af emnerne færdigproduceret ved start af dette speciale, hvor resten skal bearbejdes herefter. Grudet en dårlig defineret geometri af emnerne under produktionen afviger dimensioner af emnerne med ± 2 mm i visse tilfælde, hvilket påvirker den eksperimentielle data, samt præcisionen af Finite Element modellen. Emnerne er testet i fire punkts bøjning ved brug af Schenk 400 kN ved Aalborg Universitet, hvilket er en servo-hydraulisk maskine. Maskinen påsættes et fikstur, hvori emnerne efterfølgende indsættes og belastes. Under selve testene er diverse tøjninger målt ved brug af strain gauges for senere at kunne validere den opstillede Finite Element model.

Finite Element modellen er baseret på to emner; de færdigproducerede ved start af projektet og de efterbehandlede, hvor en afvigelse i bredden er tilstede. Derudover er der inkluderet diverse ikke-lineariteter, da disse er nødvendige for at kunne lave en tilfredsstillende model. Dette skyldes at det lav-cykliske udmattelsesområde er domineret af plastiske tøjninger, hvormed disse ikke-lineariteter skal tages højde for. I projektet er der ingen materiale tilgængelig for træktest, hvormed de monotoniske materiale egenskaber ikke kan bestemmes. Af denne grund anvendes den tidligere gruppes resultater, som er baseret på materiale af samme batch.

Når Finite Element modellen er valideret gennem resultaterne af strain gauge ved samme belastning, anvendes modellen til at konverterer det eksperimentielle data fra Schenk 400 kN til henholdsvis spænding- og tøjnings-cyklus grafer. Her sammenlignes resultaterne med diverse analytiske modeller for at vurdere hvorvidt disse modeller kan beskrive udmattelseslevetiden på et stumpsømssvejst emne. De analytsike modeller er baseret på monotonske materiale egenskaber til at bestemme udmattelsesegenskaberne, hvormed afvigelser er forventet inden de kan sammenlignes.

Grundet diverse problematikker angående de fremstillede emner opstår udmattelsesbruddet ikke i den varmepåvirkede zone eller svejsningen. Bruddene opstår i rundingerne og områder, hvor perlit bånd er tilstede, hvilket er uønsket for projektet. Grunden til brudlokalitionerne undersøges af denne grund for at kunne fastslå årsagen til brudlokaliteterne, hvorved det vil være muligt at teste udmattelsesopførslen af stumpsømssvejste emner i et nyt projekt.

Contents

1 Introduction **1**
1.1 The Test Specimen . . . 2
1.1.1 Test Specimen Type 1 . . . 3
1.1.2 Test Specimen Type 2 . . . 3
1.2 Welding Process . . . 4
1.2.1 MIG/MAG Welding . . . 5
1.2.2 Heat Affected Zone . . . 5
1.2.3 Residual Stresses . . . 6
1.2.4 Highlighting Weld and HAZ . . . 6
1.3 Material Data . . . 7

2 Analytic Models **9**
2.1 Applied Fatigue Models . . . 9
2.1.1 The Ramberg-Osgood Relationship . . . 9
2.1.2 The Basquin-Manson-Coffin Model . . . 10
2.1.3 The Smith-Watson-Topper Model . . . 11
2.1.4 Notch Effect . . . 12
2.2 Models by Scientific Paper . . . 13
2.2.1 LCF Study of S355 . . . 13
2.2.2 LCF Study of Welded T-Joint . . . 13
2.2.3 Hardness Models . . . 14
2.3 Analytic Determination of Fatigue Properties and Strain-Life . . . 17

3 Experiments **19**
3.1 Load Scenario . . . 19
3.2 Schenk 400 kN . . . 20
3.2.1 Data Sampling . . . 22
3.2.2 Choice of Control . . . 22
3.2.3 Uncertainty Assessment . . . 23
3.3 Strain Gauge Experiments . . . 23
3.3.1 Data Processing . . . 24
3.3.2 Errors During Testing . . . 25
3.3.3 Uncertainty Assessment . . . 25
3.4 Experimental Results . . . 26
3.4.1 Schenk 400 kN Results . . . 26
3.4.2 Strain Gauge Results . . . 28
3.5 Video Documentation of Experiments . . . 30
3.6 Failure Regions . . . 30
3.7 Microstructure Study . . . 32
3.7.1 Equipment and Preparation of Specimen . . . 33
3.7.2 Microstructure of Specimen . . . 33
3.8 Brinell Hardness . . . 34

3.8.1 Experimental Testing 35

4 Finite Element Model **37**

4.1 Finite Element Theory 37

4.1.1 Non-Linearities 38

4.1.2 Structural Non-Linearities 39

4.1.3 Newton-Raphson Solution Method 40

4.2 Initial Finite Element Analysis 42

4.2.1 Investigation of Stress Concentrations 43

4.3 Non-Linear Finite Element Analysis 43

4.3.1 Material Model 44

4.3.2 Elements and Meshing 44

4.3.3 Contact Formulation 46

4.3.4 Solution Controls 46

4.4 Results 47

5 Comparison **49**

5.1 Finite Element Model vs Strain Gauge Data 49

5.2 Analytic Models vs Experimental Data 51

5.2.1 Regression of Experimental Data 52

5.2.2 Fatigue Stress Concentration Factor 54

5.3 Stress-Life Comparison 54

5.4 Study of Reversal Ratio 55

6 Discussion **57**

7 Conclusion **61**

8 Future Work **63**

Bibliography **65**

A Analytic Models **A69**

B Brinell Hardness **A71**

C Standard Deviations of Experimental Data from Schenk 400 kN **A73**

D Four Point Bending Tool **A75**

Introduction 1

In the last centuries, the fatigue life of materials have been heavily investigated by researchers to explain the failure mechanisms of structures. This involves acquiring an understanding of the materials utilized in various structures, whether it is metals such as steel and aluminum or even composite materials such as glass- and carbon-fiber. The work conducted so far has mainly been focusing on the long term endurance of the structures, as a high operational life is desired for structural applications. In 1870, A. Wöhler presented a study in which he investigated the number of cycles to failure with respect to stress, and presented it graphically [13]. These graphs are known as Wöhler diagrams, or S-N curves, which is an abbreviation of Stress(S)-Life(N), and illustrated in figure 1.1.

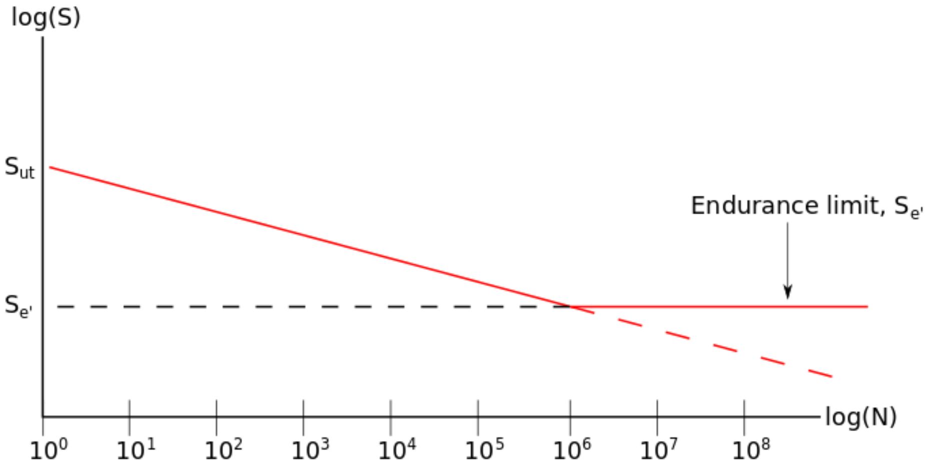

Figure 1.1: Illustration of a S-N curve or Wöhler diagram.

The S-N diagrams are well-established and utilized to evaluate the life-time of structures. In addition, the S-N diagrams are especially utilized for structures and applications designed for long life services. This stress-life approach furthermore led to the development of the strain-life approach. The concept is similar to the stress-life approach, though strains are utilized instead of stresses, and therefore more convenient when applications involve plastic deformation. This have led to numerous low-cycle studies, including the work conducted in this study.

The study presented is a continuation of previous work, conducted by a DMS group at Aalborg University. Consequently, complications arose during the study with respect to the specimen, which is further documented in section 1.1 along with a general presentation of the specimen. The study investigates fatigue behavior of welded specimen, where knowledge of the welding process is necessary. This is presented in section 1.2. As knowledge of the specimen is acquired, analytic models describing an approximated life-time is presented in chapter 2 and later evaluated with experimental work of chapter 3. Along the experimental work, a

Finite Element model is established in chapter 4, which is validated by experimental results obtained through strain gauges. Upon acquiring an accurate model, it is possible to convert displacement-life to strain-life and stress-life curves in chapter 5.

1.1 The Test Specimen

In this section, the two types of test specimen utilized in the project are presented and described in section 1.1.1 and 1.1.2, respectively. The two types of specimen varies in geometry due to necessary post-processing, which is described in section 1.1.2. The manufacturing of the specimen by the previous group are poorly formulated, and, consequently, the manufactured specimen are varying in dimensions, which must be taken into account during evaluation of data. All specimen are manufactured from three plates of S355J2 structural steel, which is an European Standard [31] of non-alloy structural steel. Two of the plates have dimensions 1000x240x10 mm, while the third being 800x240x10 mm. From the two 1000x240x10 mm plates, 36 specimen with a width of 50 mm are manufactured, while 14 specimen are manufactured from the 800x240x10 mm plate. Each plate is milled in the center to create a V-shaped chamfer, as depicted in figure 1.2, as a prerequisite for the welding process.

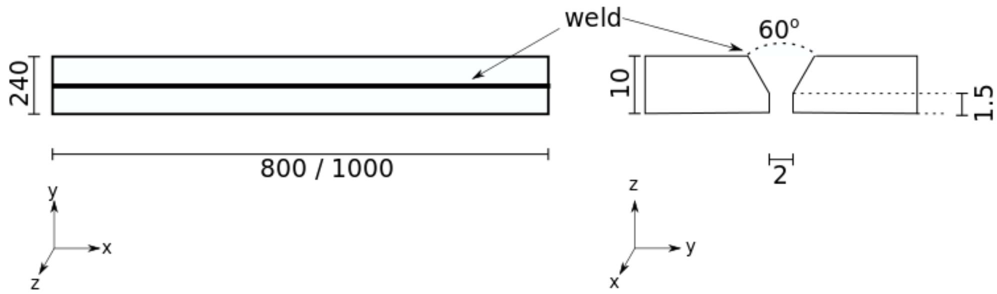

Figure 1.2: Dimensions [mm] of plates and the V-shaped weld chamfer in specimen.

All specimen are welded by MIG/MAG welding, utilizing the 131/135 procedure according to the European Standards [33] and [34]. The MIG/MAG welding process is further described in section 1.2.1. The welding process is conducted by the company *Maskinfabrikken Fuglsangs Eftf. A/S* located in Klarup, Denmark, which is conducted according to the standard [32]. The initial and final part of the weld are removed to ensure a uniform weld throughout the plate. Consequently, a total of 100 mm is removed of each plate. The welded plates are divided into specimen with the dimensions 240x50x10 mm, which each is numerated. The weld is located along the width in the center of the specimen. In addition, each specimen is processed by a surface grinder, resulting in a thickness of 8 mm. By surface grinding the specimen, potential geometrical stress concentrations introduced by the weld toe are removed. This procedure is illustrated in figure 1.3. Initial work by the previous group; [25], concluded the specimen are too stiff even with a reduction in thickness, and consequently roundings are applied each specimen. This procedure is described in section 1.1.1, where type 1 of the specimen is presented. Initially, all specimen should have been type 1, but due to complications, a type 2 is necessary. The type 2 is presented and described in section 1.1.2.

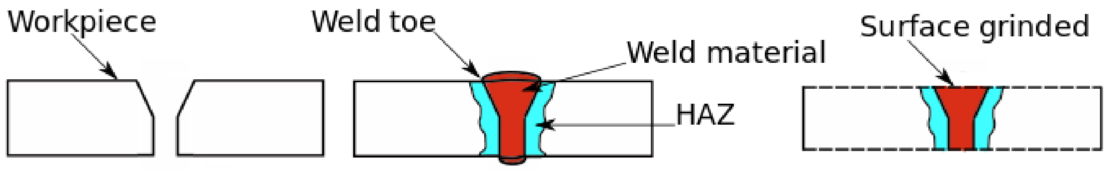

Figure 1.3: Processing of plate. Left: Workpieces with V-shape chamfer before welding. Middle: Workpieces welded together to specimen with Heat Affected Zone illustrated. Right: Welded specimen being surface grinded, reducing thickness.

1.1.1 Test Specimen Type 1

Initially, the test specimen of the project are intended to all be type 1. The type 1 specimen are depicted in figure 1.4. Roundings have been applied to the specimen, which results in a reduction in stiffness, and thereby ensuring failure in the region between the roundings. In addition, fillets of 2 mm are applied to the roundings and edges.

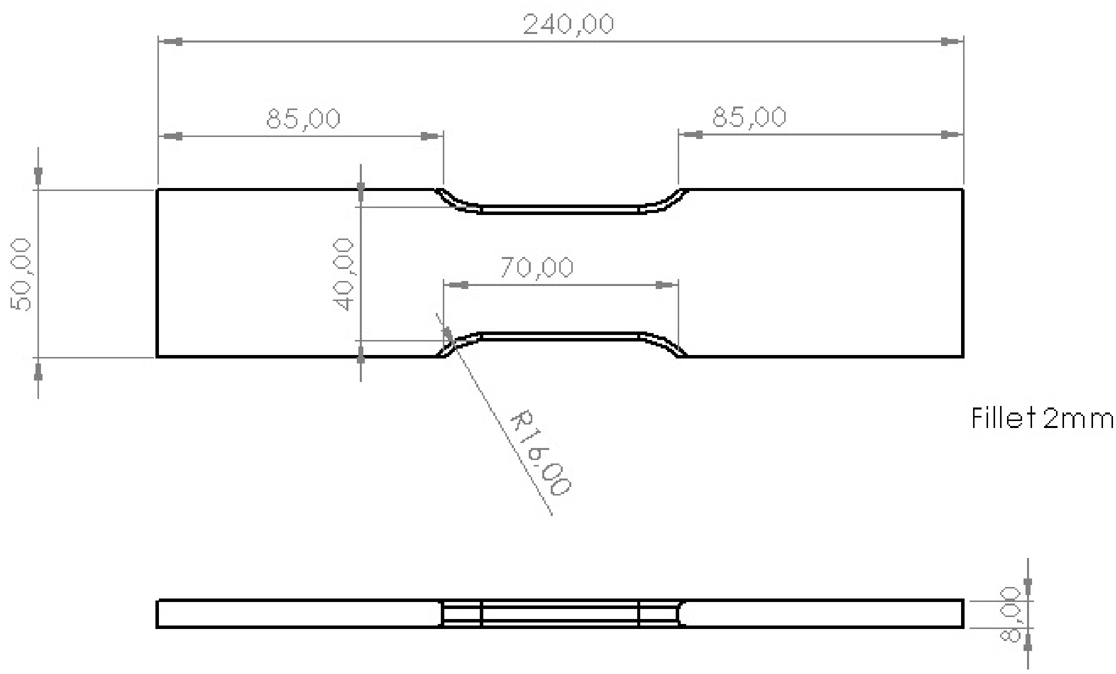

Figure 1.4: Specimen type 1 with dimensions [mm].

As the fillets are applied, the test specimen are ready for testing. However, not all specimen are manufactured by the type 1 dimensions. The type 1 specimen are available from the initial phase of the study, however, a severe number of specimen are incomplete. Due to manufacturing difficulties, the dimensions of these specimen are altered resulting in a new type of specimen; type 2.

1.1.2 Test Specimen Type 2

In this section, the test specimen type 2 is presented. It is discovered after the start of this project, that several test specimen have not been applied fillets in the roundings and edges. Other specimen have not even been applied roundings. For this reason, the workshop at Aalborg University is tasked with processing these specimen into type 1 test specimen.

Consequently, the width of the specimen are altered from the 40 mm depicted in figure 1.4 to 37 mm as depicted in figure 1.5. Additionally, a fillet of 2 mm is applied. As experimental data is acquired, from specimen type 1 and 2, it is important to post-process the data with respect to the dimensions when comparing results. The data is not comparable if this is not accounted for.

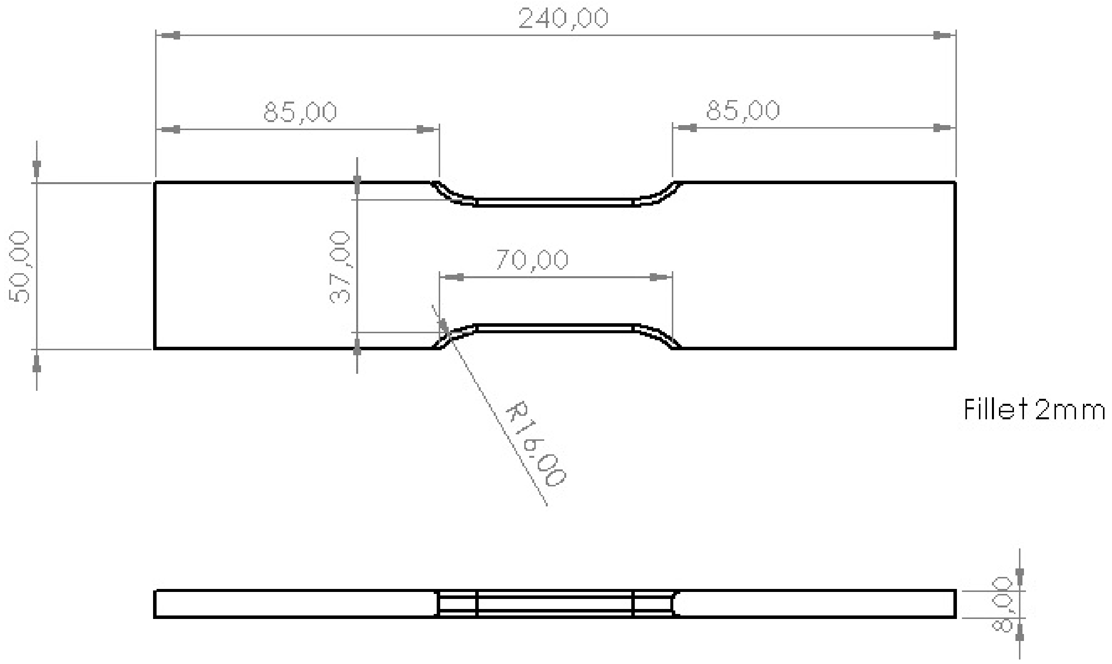

Figure 1.5: Specimen type 2 with dimensions [mm].

1.2 Welding Process

In this section, the welding process utilized for the specimen is presented. In general, a welding can be specified as a joining of two or more workpieces. Often the workpieces are joined together by utilizing a filler material; a material is added during the welding process to enable joining the workpieces. The type of weld utilized for the specimen is a butt-weld, which is a common type of weld in the industry. Butt-welds are often split into two categories; full penetration and partial penetration. These are depicted in figure 1.6. The butt-weld utilized for the specimen is full penetration.

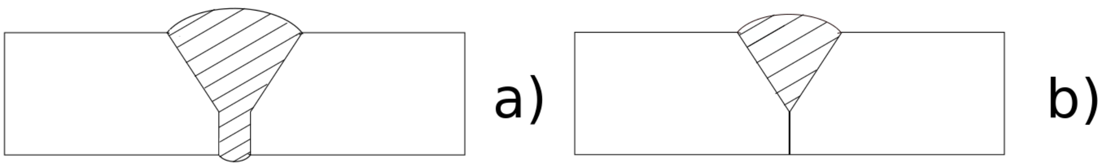

Figure 1.6: Illustration of a) Full penetration butt-weld and b) Partial penetration butt-weld.

The welding type utilized to make the butt-weld of the specimen is a Gas Metal-arc Welding defined as MIG/MAG, which is an abbreviation of *Metal Inert Gas/ Metal Active Gas*. The method is briefly described in section 1.2.1. During the welding process, the surrounding base material is affected by the heat of the process. The region affected by heat of the welding without being a part of the welding itself is defined as the Heat Affected Zone, abbreviated

HAZ. The HAZ is further described in section 1.2.2, as it might provide usable knowledge with respect to experimental resuts. In addition, the welding process introduces residual stresses to the specimen, which is briefly described in section 1.2.3.

1.2.1 MIG/MAG Welding

The MIG/MAG welding is depicted in figure 1.7. This type of welding utilizes a filler material, which is being fed through a nozzle into the weld arc during the welding process as either filler rods or wire [15]. In addition, the MIG/MAG welding utilizes a shielding gas during the welding process. The shielding gas creates a protective area around the welding, which prevents any possible oxidation of the material during the welding process, resulting in a stronger weld.

The solidification of the weld metal affects the microstructure of the weld, often resulting in coarse grains due to slow cooling [15]. Surrounding material, which is located in the HAZ, is affected as well. This is further described in section 1.2.2, though it is clear that the heat and solidification have a significant impact on the microstructure and thereby the mechanical properties of the specimen. The impact can be reduced by e.g. careful selection of filler material and heat treatment, though it is unknown whether such decisions are accounted for during the welding process.

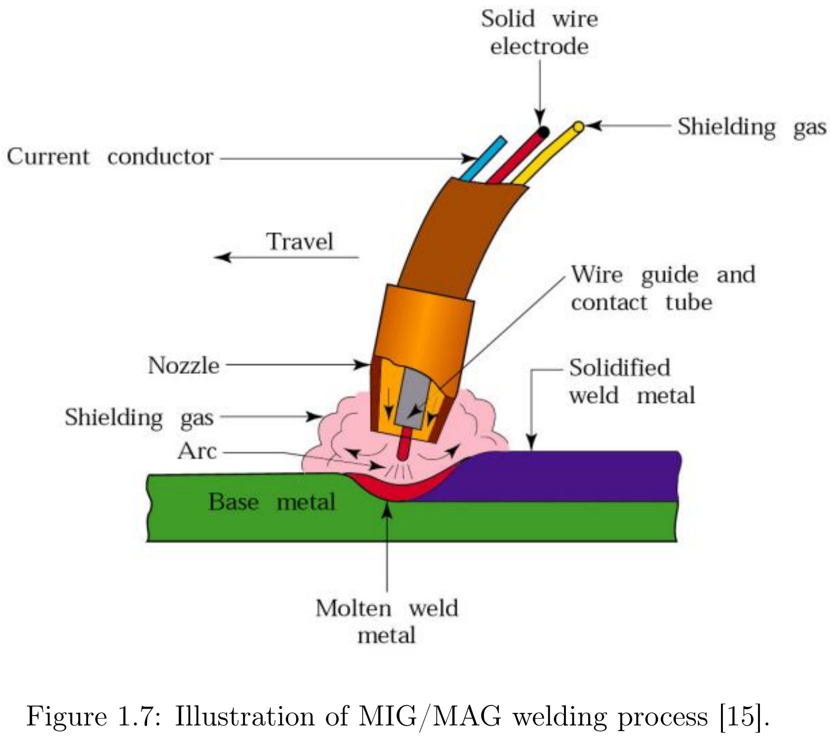

Figure 1.7: Illustration of MIG/MAG welding process [15].

1.2.2 Heat Affected Zone

The arc of the welding torch initiates the chemical reactions of the MIG/MAG welding process. These reactions together with the arc of the welding torch result in heat being generated in the base material, which is concentrated in the weld and surrounding base material. Consequently, the microstructure of the base material, and thereby the material properties, is altered, e.g. hardness and strength [15]. The area affected by this heat is defined as the Heat Affected Zone, or HAZ as previously defined. The material adjacent to the weld is undergoing the greatest microstructural changes due to elevated temperatures, as depicted in figure 1.8. The effect of the temperatures is decreased as distance to the weld is increased. Consequently, the mechanical properties of the HAZ are position dependent. The actual strength and hardness throughout the HAZ is furthermore dependent on the original strength and hardness of the base material.

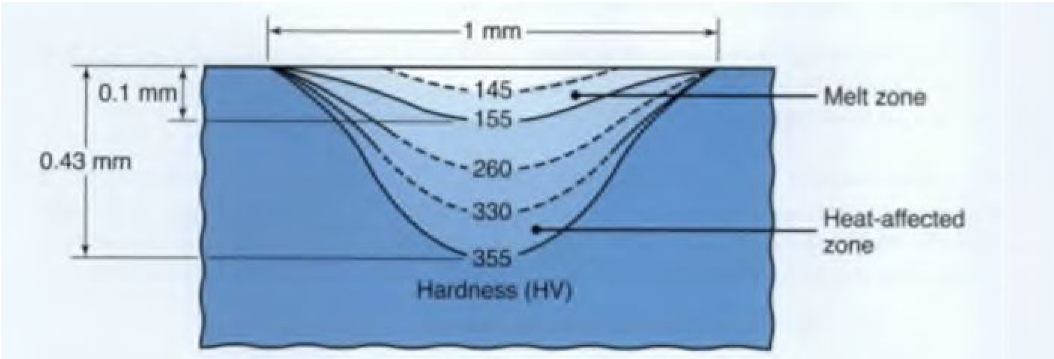

Figure 1.8: Effect of elevated temperatures with respect to hardness [15].

1.2.3 Residual Stresses

Residual stresses can arise from several sources, i.e. mechanical methods or thermal methods. The specimen of this study are hot rolled, and subsequently welded and machined. These manufacturing processes induce residual stresses, though the thermal effects of the welding process is deemed to induce the most significant residual stresses in relation to fatigue life. During the welding process the base material is locally heated and cooled. Residual stresses are introduced to the workpiece as a result of the non uniform thermal expansion, and subsequent contraction of the base material. This induces significant tensile residual stresses in weld and HAZ, which are detrimental to fatigue life.

1.2.4 Highlighting Weld and HAZ

Due to the surface grinding described in section 1.1, the weld and HAZ are not visible. It is desired to highlight the weld and HAZ to investigate their size. In addition, by highlighting the weld and HAZ, it is possible to observe whether the failure occurs in the weld, HAZ or base material. A method to visualize the weld and HAZ is for this reason necessary. After consultation with supervisor and workshop of Aalborg University, it is desired to render the weld visible utilizing ammonium persulfate etch., abbreviated APS, which is an oxidizing agent. By applying the APS, the surface of the specimen is oxidized, which reveals the weld and HAZ. As the results of the APS is not fully satisfying, nitric acid is utilized on the oxidized surface. The result is presented in figure 1.9.

After the application of APS and nitric acid, the weld and HAZ in figure 1.9 is visible. By inspection of the oxidized specimen, formation of grain is detected adjacent to the HAZ, though no microstructural changes should occur in this area. This is investigated further in section 3.7, which extends the work conducted in this section. As applying APS and nitric acid provides satisfying results, it is utilized to evaluate whether the specimen are failing in weld, HAZ or base material.

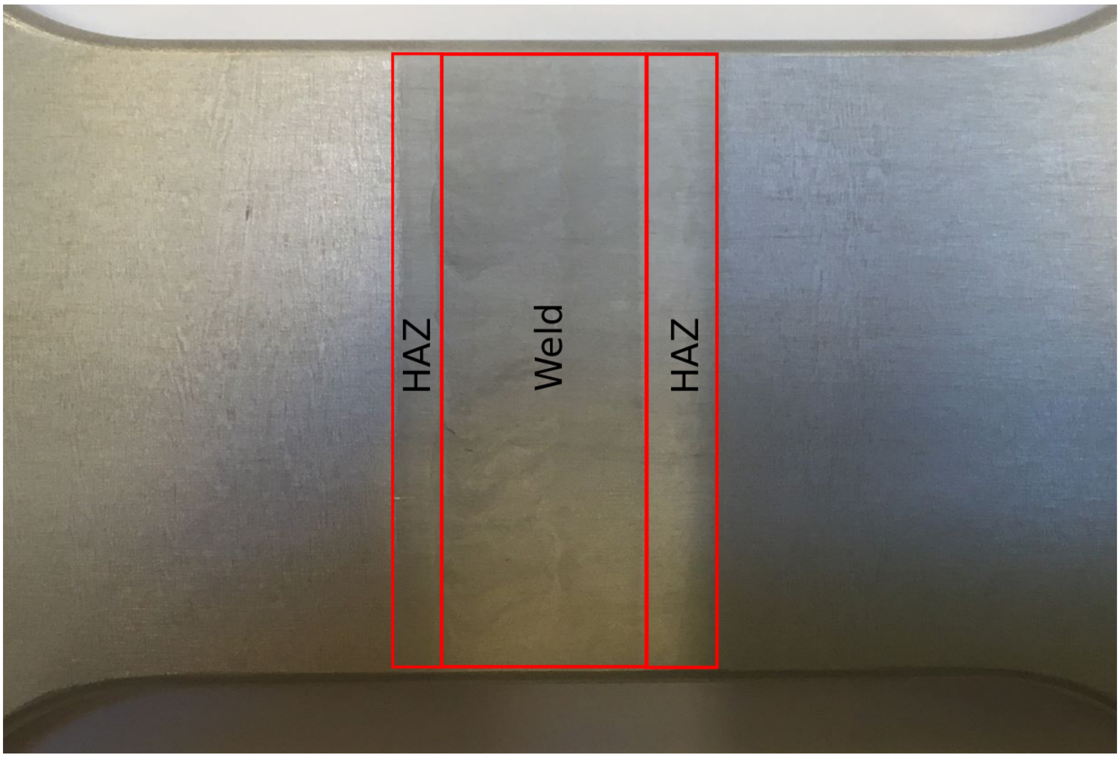

Figure 1.9: Close-up of specimen after application of APS and nitric acid on surface rendering the weld and HAZ visible.

1.3 Material Data

It is desired to determine the material properties of the S355J2 steel, where a tensile test is deemed sufficient to acquire the necessary material data. However, no material of the same batch is available and the monotonic material data can thereby not be determined. Consequently, the monotonic properties obtained in [25] is utilized, as material of same batch is utilized, see table 1.1 and figure 1.10.

Plate	E [GPa]	σ_y [MPa]	σ_{ut} [MPa]
10 mm	198.1	355.9	495.6
15 mm	198.1	401.2	547.2
Weld	198.1	555	615

Table 1.1: Material properties of [25].

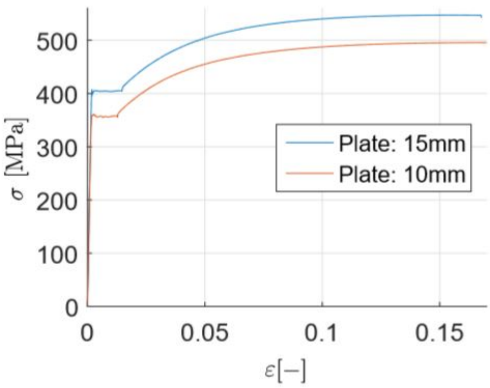

Figure 1.10: Stress-strain curve of [25].

As the thickness of the specimen in this project is < 10 mm, the material properties of a 10 mm plate in table 1.1 is utilized. The material data is utilized for the analytic approaches in section 2.3 and for the Finite Element model in chapter 4.

Analytic Models 2

In this chapter, the analytic fatigue models utilized in this study are presented. The fatigue approaches for the two regions, high-cycle and low-cycle fatigue region, abbreviated HCF and LCF, vary. The fatigue models established for the LCF region are primarily based on the strain-life approach, while the HCF region models are on the stress-life approach. The HCF region is elastic dominated, i.e. deals with small cyclic loads, while the LCF region is plastic dominated, i.e. deals with large plastic deformations.

This chapter is split into three sections. Section 2.1 presents and describes the models utilized in this study, which are based on [12]. Section 2.2 presents analytic models based on scientific papers, which utilizes monotonic material properties to predict fatigue life. In addition, section 2.3 presents analytically determined curves based on the models of section 2.2. The three sections are listed in an itemize below to provide an overview of the chapter. It should be noted the models of [12] and majority of the articles are not dealing with welded specimen, as the LCF behavior of welded structures are limited compared to non-welded structures. Consequently, the models are expected to deviate from experimental data acquired in chapter 3.

- Applied Fatigue Models - section 2.1
- Models by Scientific Papers - section 2.2
- Analytic Determination of Fatigue Properties and Strain-Life - section 2.3

2.1 Applied Fatigue Models

In this section, the fatigue models utilized are presented. Each of the models is assigned a section in which the model is briefly described. This includes the equation, the components of the equation and, if possible, graphical representation of the model.

2.1.1 The Ramberg-Osgood Relationship

The Ramberg-Osgood relationship is an expression, which describes the true stress-true strain relationship of a specimen subjected to a monotonic load. The model itself is not utilized in this study, however, it provides an understanding for the presented analytic models by scientific papers in section 2.2. The expression of Ramberg-Osgood describes the true strain based on elastic and plastic strain, see equation 2.1. The elastic strain is expressed by Hooke's Law as presented in equation 2.2, while the plastic strain is expressed by a power law presented in equation 2.3.

$$\varepsilon = \varepsilon_e + \varepsilon_p = \frac{\sigma}{E} + \left(\frac{\sigma}{K}\right)^{\frac{1}{n}} \tag{2.1}$$

$$\varepsilon_e = \frac{\sigma}{E} \tag{2.2}$$

$$\sigma = K(\varepsilon_p)^n \tag{2.3}$$

ε	=	True strain	K	=	Strength coefficient
σ	=	True stress	n	=	Strain hardening exponent
ε_e	=	Elastic strain $= \sigma E^{-1}$	E	=	Young's modulus
ε_p	=	Plastic strain $= (\sigma K^{-1})^{-n}$			

Do note that the expression in equation 2.1 is for monotonic tests only. As the tests conducted in this project are cyclic, it is desired to present an expression for cyclic loading. Equation 2.1 is for this reason rewritten to equation 2.4, in which the parameters are modified to a cyclic load scenario.

$$\varepsilon_a = \frac{\sigma_a}{E} + \left(\frac{\sigma_a}{K'}\right)^{\frac{1}{n'}} \tag{2.4}$$

K'	=	Cyclic strength coefficient	σ_a	=	Stress amplitude
n'	=	Cyclic strain hardening exponent	ε_a	=	Strain amplitude

2.1.2 The Basquin-Manson-Coffin Model

The Basquin-Manson-Coffin model consists of two models; The Basquin model, which describes the elastic strain amplitude of a specimen subjected to cyclic loading and the Manson-Coffin model, which describes the plastic strain amplitude of a specimen subjected to cyclic loading. By combining these two models, the Basquin-Manson-Coffin model is acquired, which describes the total strain amplitude. The model is abbreviated BMC and presented in equation 2.5. Note, this model is valid for fully reversed cyclic loading, in which $R = -1$ and consequently no mean stresses are present.

For convenience, the Basquin model is underlined in red and Manson-Coffin model in blue in equation 2.5. In addition, the elastic, plastic and total strain amplitudes are illustrated in figure 2.1 to provide an understanding of how the elastic and plastic strain amplitudes affect the total strain amplitude. The intersection where elastic and plastic strain amplitude curves crosses in figure 2.1, illustrated by a dashed line, is defined as the transition fatigue life $2N_t$. At the transition fatigue life, the elastic and plastic strain amplitudes are of equal magnitude and the point indicates the change in dominance with respect to elastic and plastic strain. As depicted in figure 2.1, the total strain amplitude is dominated by the plastic strain amplitude until the transition fatigue life is reached. After this point, the total strain amplitude is dominated by the elastic strain amplitude. As the transition fatigue life describes the change in dominance of elastic and plastic strain amplitude, it can be utilized to estimate the LCF and HCF region. The definition of the LCF region differs in literature, as some defines it from

1 to 10^3 cycles, while some defines it up to 10^4 cycles. Therefore, the transition fatigue life can be utilized to estimate the LCF region.

$$\frac{\Delta\varepsilon}{2} = \frac{\Delta\varepsilon_e}{2} + \frac{\Delta\varepsilon_p}{2} = \underline{\sigma_f^{'} E^{-1}(2N_f)^b} + \underline{\varepsilon_f^{'}(2N_f)^c} = \varepsilon_a \tag{2.5}$$

ε_a	=	Total strain amplitude	$\sigma_f^{'}$	=	Fatigue strength coefficient
$\frac{\Delta\varepsilon_e}{2}$	=	Elastic strain amplitude	$\frac{\Delta\varepsilon_p}{2}$	=	Plastic strain amplitude
$\varepsilon_f^{'}$	=	Fatigue ductility coefficient	b	=	Fatigue strength exponent
E	=	Young's modulus	c	=	Fatigue ductility exponent
$2N_f$	=	Number of reversals to failure			

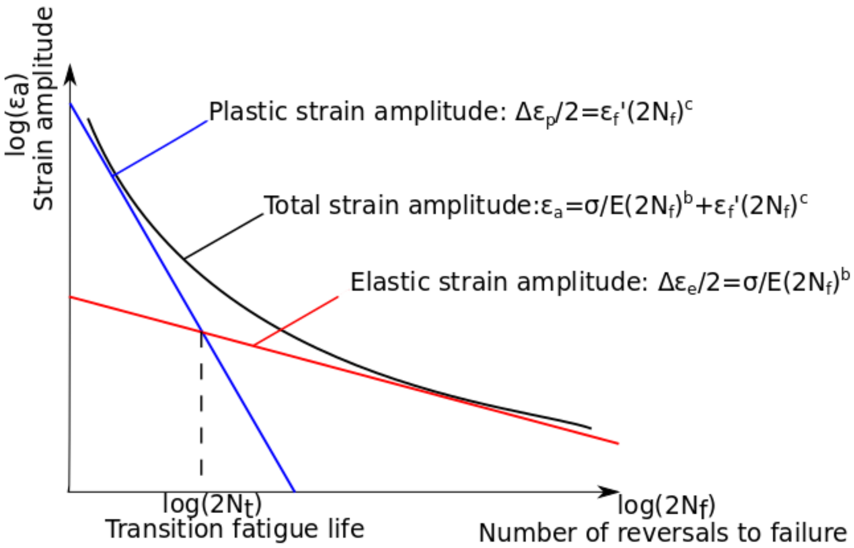

Figure 2.1: Illustration of the strain amplitude as function of number of reversals to failure.

2.1.3 The Smith-Watson-Topper Model

The Smith-Watson-Topper model, abbreviated SWT, is a fatigue model, which accounts for any R-ratio. Consequently, the effect of mean stresses are accounted for. The SWT model, presented in equation 2.6, can be derived of the BMC model in equation 2.5.

$$\sigma_{max}\varepsilon_a E = (\sigma'_f)^2(2N_f)^{2b} + \sigma'_f\varepsilon'_f E(2N_f)^{b+c} \tag{2.6}$$

σ_{max}	$=\sigma_a + \sigma_m$	Maximum tensile stress
σ_m		Mean stress

The SWT expression is obtained by multiplying σ_{max} and E to the BMC expression. Assuming the material behaves ideally and satisfy compatibility conditions, σ_{max} can be expressed as in equation 2.7. The compatibility conditions are $n' = b/c$ and $K' = \sigma'_f/(\varepsilon'_f)^{n'}$ [14] and $R = -1$.

$$\sigma_{max} = \sigma_a = \sigma'_f(2N_f)^b \tag{2.7}$$

$$\begin{aligned}\sigma_{max}\varepsilon_a E \; &= (\sigma'_f E^{-1}(2N_f)^b + \varepsilon'_f(2N_f)^c)(\sigma_{max}E) \\ &= (\sigma'_f E^{-1}(2N_f)^b + \varepsilon'_f(2N_f)^c)(\sigma'_f(2N_f)^b E) \\ &= (\sigma'_f)^2(2N_f)^{2b} + \varepsilon'_f\sigma'_f E(2N_f)^{b+c}\end{aligned} \tag{2.8}$$

The SWT model states, that $\sigma_{max}\varepsilon_a$ is constant for a given life N. Considering a scenario of $R = -1$, then $\sigma_{max} = \sigma_a$ and $\sigma_{max}\varepsilon_a = \sigma_a\varepsilon_a$, as no mean stress is present. However, if $R \neq -1$ a mean stress is present, which alters σ_{max} and ε_a. If the mean stress results in an increase of σ_{max}, then ε_a decreases to uphold a constant value. However, if the mean stress reduces σ_{max}, then ε_a increases. Consequently, it is clear that the mean stress influences the fatigue life of a specimen. However, the magnitude of this influence, whether it is negligible or has to be accounted for, is investigated in section 5.4. This investigation is initiated to acquire an understanding of the importance of the R-ratio. Note, if $R = -1$, no mean stress is present and SWT simplifies to BMC.

2.1.4 Notch Effect

Roundings are applied the specimen, where geometric stress concentrations are introduced as a consequence of this. The roundings are defined with a radius of 16 mm, which should ensure the effect of the concentration factor is limited. However, it is desired to investigate this further, as a significant number of specimen in chapter 3 are failing in or in the vicinity of the roundings. As the specimen are subjected to cyclic loading, the fatigue stress concentration factor K_f is defined based on the geometric stress concentration factor K_t. K_t is determined according to illustration in figure 2.2 and D/d ratio in [13], presented in equation 2.9. The geometric parameters r, d and D are presented in table 2.1 along with corresponding b and A values. Note, the load scenario depicted in figure 2.2 is not exact, however, it is deemed sufficient for an approximation of the geometric stress concentrations.

$$K_t \approx A\left(\frac{r}{d}\right)^b \tag{2.9}$$

	r	D	d	D/d	b	A	K_t
Type 1	16	50	40	1.2	-0.25084	1.0351	$1.3026 \approx 1.3$
Type 2	16	50	37	≈ 1.2	-0.25084	1.0351	$1.2773 \approx 1.3$

Table 2.1: Values to determine K_t for type 1 and type 2.

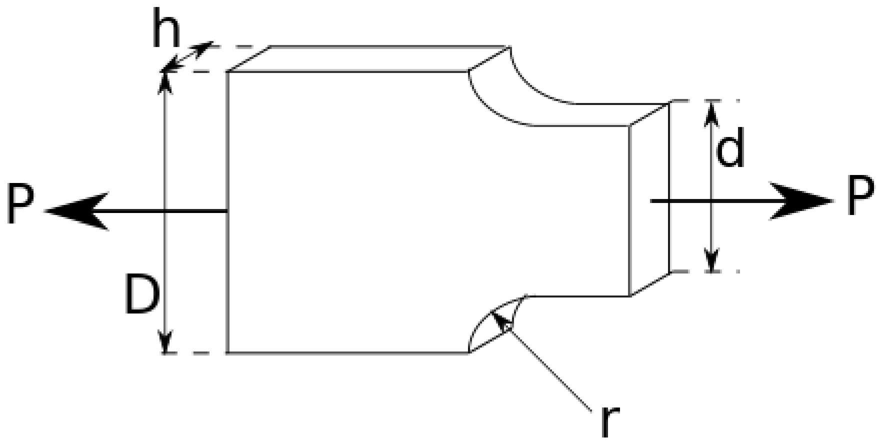

Figure 2.2: Illustration of geometric parameters to determine K_t.

K_t is utilized to determine K_f according to equation 2.10 [12].

$$\begin{aligned} K_f &= 1 + \frac{K_t - 1}{1 + a/r} && \approx 1.3 \\ a &= 0.0254 \left(\frac{2070}{S_{ut}}\right)^{1.8} && = 0.3329 \end{aligned} \tag{2.10}$$

The true strain- and stress state at the roundings is a factor of 1.3 higher than nominal strain and stress, which could account for the failure regions identified in section 3.6. The effect of K_f is considered in chapter 5.

2.2 Models by Scientific Paper

In addition to the analytic models of [12], several scientific papers have been investigated to acquire knowledge of fatigue of welded specimen. The research led to several interesting articles, though most are not for welded specimen. It is, however, of interest to evaluate these models in relation to fatigue results obtained in this study.

2.2.1 LCF Study of S355

The article [6] investigates the LCF behavior of S355 and S690 structural steel, where the results for the S355 steel is of interest. The average material properties of the S355 steel is; E of 210.5 GPa, σ_y of 419 MPa and σ_{ut} of 732 MPa. The material properties differ significantly from the provided material data of section 1.3, however, it is of interest to compare the model of [6] to the experimental data of this study. The fatigue data of [6], which is utilized to establish an analytic curve, is presented in table 2.2 as FP, where it is compared to fatigue properties of alternative models.

2.2.2 LCF Study of Welded T-Joint

In [1], the LCF behavior of welded steel T-joints is investigated. The article provides two types of information utilized in this study; firstly, information to provide analytic curves based on the strain-life approach and secondly, a stress-life approach is presented.

Approximations of Fatigue Properties Based on Monotonic Material Properties

The approximations introduced in [1] are presented in equation 2.11. Note, all expressions are based on monotonic material properties; the ultimate tensile strength S_{ut} and yield stress σ_y. As fatigue tests are time consuming, it is beneficial to determine fatigue properties and thereby fatigue life of a specimen by monotonic properties. For this reason, it is desired to investigate how well these approximations describes the specimen of this study. The usage of the approximations are presented in section 2.3.

$$
\begin{aligned}
n' &= \frac{b}{c} & \varepsilon_f' &= \left(\frac{\sigma_f'}{K'}\right)^{\frac{1}{n'}} \\
K' &= \sigma_y'(0.002)^{-n'} & \sigma_f' &= 0.95 S_{ut} + 370\text{MPa} \\
\sigma_y' &= 0.608 S_{ut} & b &= -0.1667 \log\left(2.1 + \frac{917}{S_{ut}}\right) \\
c &= [-0.7 : -0,5]
\end{aligned}
\tag{2.11}
$$

Stress-Life Approach

In addition to the analytic approximations of the fatigue properties, [1] provides a stress-life approach for welded steel T-joints. The article proposes that the LCF behavior, of welded steel specimen, can be described by a line between two points at N = 1 cycle and N = 3000 cycles. The equations utilized to describe the two points are presented in equation 2.12.

$$
\begin{aligned}
\Delta\sigma(N=1) &= 2S_{ut} \\
\Delta\sigma(N=3000) &= 2\frac{3}{4}S_{ut}
\end{aligned}
\tag{2.12}
$$

The data of the study conducted by [1] are within ±2x standard deviations from the line interpolated by the two points. A knee drop is observed pertaining to the data beyond N = 3000 cycles. An exact formulation for the linear expression beyond N = 3000 cycles is unknown, though this is deemed possible to approximate through experimental data. Note, the T-joints of [1] are not load carrying as the butt-joints of this study, hence the expressions of equation 2.12 might not be valid.

2.2.3 Hardness Models

Two approaches by [2] and [3] entitled approach 1 and 2, respectively, are presented in this section. Both approaches utilizes the Brinell hardness and monotonic material properties to estimate the fatigue properties. Several scientific papers have investigated the approximation of fatigue properties by hardness besides the two approaches presented. In [7] it is concluded that a change in hardness due to cyclic loading is negligible and the determination of ultimate tensile strength and fatigue properties by Brinell hardness are in agreement with experimental data. In addition, [8] concludes a good linear relationship exists between the fatigue strength and ultimate tensile strength, or hardness. As the hardness is acquired by nondestructive tests, it is a beneficial way of determining the fatigue life as experimental time and cost is reduced.

In general, both [2] and [3] provide an approach to determine the unknown fatigue properties of the BMC model by utilizing the Brinell hardness and Young's modulus, which is documented in the two subsequent sections. The Brinell hardness is acquired in section 3.8.

Approach 1

In the work of [2], simple approximations are utilized in order to predict fatigue properties and life. The model utilizes a simple approximation of the fracture strength σ_f, which can be approximated by the Brinell hardness, see equation 2.13 [12]. The ultimate tensile strength S_{ut} is approximated by the Brinell hardness number by a linear relationship.

$$\sigma_f = S_{ut} + 345MPa = 3.45HB + 345MPa \tag{2.13}$$

$$\begin{aligned} HB &= \text{Brinell hardness number} \\ \sigma_f &= \text{Fracture strength} \\ S_{ut} &= \text{Ultimate tensile strength} = 3.45 \cdot HB \end{aligned}$$

The fracture strength σ_f of the material can be utilized to determine the fatigue strength exponent b, based on the expression in equation 2.14 [13].

$$b = \frac{1}{log(N_1) - log(N_2)} log\left(\frac{S_{N_1}}{S_{N_2}}\right) \tag{2.14}$$

$$\begin{aligned} N_1 \quad \text{and} \quad N_2 &= \text{Number of cycles} \\ S_{N_1} \quad \text{and} \quad S_{N_2} &= \text{Fatigue strength at } N_1 \text{ and } N_2\text{, respectively} \end{aligned}$$

Assuming that N_1 is at $N = 1$ cycles and that N_2 at $N = 10^6$ cycles, the corresponding strength values are $S_{N_1} = \sigma_f$ and $S_{N_2} = S_e^{'} = \frac{1}{2}S_{ut}$, where $S_e^{'}$ is the endurance-limit of the material. Inserting these values into equation 2.14, the definition of equation 2.15 is acquired.

$$b = -\frac{1}{6} log\left(\frac{2\sigma_f}{S_{ut}}\right) \approx -\frac{1}{6} log\left(\frac{2\sigma_f^{'}}{S_{ut}}\right) \tag{2.15}$$

Do note that the fracture strength σ_f in equation 2.15 is replaced by the fatigue strength coefficient $\sigma_f^{'}$, as it is assumed by [2] that these values are approximately equal; $\sigma_f^{'} \approx \sigma_f$. The article furthermore presents an expression for the transition fatigue life $2N_t$ based on a different study, where a correlation between Brinell hardness and transition fatigue life is expressed in equation 2.16. Note, this is merely an approximation.

$$ln(2N_t) = 13.6 - 0.0185HB \tag{2.16}$$

Based on the transition fatigue life $2N_t$, the elastic strain amplitude $\frac{\Delta\varepsilon_e}{2}$ can be determined if a monotonic tensile test is conducted to acquire the Young's modulus E of the material. As the elastic strain amplitude is determined, the plastic strain amplitude $\frac{\Delta\varepsilon_p}{2}$ is obtained, as the plastic and elastic strain amplitude are equal at the transition fatigue life. This is utilized to approximate the fatigue ductility coefficient $\varepsilon_f^{'}$ in equation 2.17.

$$\frac{\Delta\varepsilon_p}{2} = \frac{\Delta\varepsilon_e}{2} \rightarrow \varepsilon_f^{'}(2N_t)^c = \frac{\sigma_f^{'}}{E}(2N_t)^b \rightarrow \varepsilon_f^{'} = \frac{\sigma_f^{'}}{E}\frac{(2N_t)^b}{(2N_t)^c} \tag{2.17}$$

As the fatigue ductility coefficient $\varepsilon_f^{'}$ is determined, the elastic and plastic strain amplitudes are obtained and an analytic approximation of the total strain amplitude is acquired.

Approach 2

The second approach by [3], in which experimental tests have been conducted to modify existing simple estimation of fatigue properties based on monotonic properties. The approximations have been adjusted by utilizing a least square fit method between the analytic approximations and the experimental data for multiple steels, thereby modifying the existing analytic approximations. The work of [3] results in a simplified BMC model, in which the only unknown properties are the Brinell hardness and Young's modulus. The approximations and approach of how to obtain the simplified model is described in this section. Recall from approach 1 by [2] that the fatigue strength coefficient $\sigma_f^{'}$ is determined by the Brinell hardness. This second approach determines $\sigma_f^{'}$ by a different expression utilizing the Brinell hardness, see equation 2.18.

$$\sigma_f^{'} = 4.25HB + 225MPa \tag{2.18}$$

Furthermore, [3] utilizes a relationship between the transition fatigue life $2N_t$ and the Brinell hardness number shown by Landgraf. The relationship is presented in equation 2.19. The relationship utilized in [3] is, however, defined as in equation 2.20, which is based on a least square fit with a coefficient of determination $R^2 = 0.89$. The expression in equation 2.20 is utilized, as it is deemed in close agreement with the expression in equation 2.19, while it is based on the experimental data acquired in [3].

$$log(2N_t) = 6.126 - 0.0083HB \tag{2.19}$$

$$log(2N_t) = 5.755 - 0.0071HB \tag{2.20}$$

Through experimental testing, the fatigue strength exponent b and fatigue ductility exponent c are determined. b is determined to be -0.09, which is an average of the obtained values and similar to the Method of Universal Slopes. The average for c is -0.6, however, a value of -0.56 as in the Method of Universal Slopes is utilized instead. As these values are fixed, it is possible to determine the fatigue ductility coefficient $\varepsilon_f^{'}$ by utilizing the transition fatigue life $2N_t$, see equation 2.21. The expression acquired for the fatigue ductility coefficient is furthermore simplified by [3] with a second-order polynomial, which coincides well with the actual expression in the range of 150<HB<700. Consequently, this simpler expression is utilized, see equation 2.21.

$$\varepsilon_f^{'} = \frac{\sigma_f^{'}(2N_t)^b}{E(2N_t)^c} \approx \frac{0.32(HB)^2 - 487(HB) + 191000}{E} \tag{2.21}$$

If the modified approximations for $\sigma_f^{'}$, $\varepsilon_f^{'}$, b and c are inserted into the BMC model, a simplified model based on the Brinell hardness number HB and Young's modulus E is obtained, see equation 2.22.

$$\frac{\Delta\varepsilon}{2} = \frac{4.25(HB) + 225}{E}(2N_f)^{-0.09} + \frac{0.32(HB)^2 - 487HB + 191000}{E}(2N_f)^{-0.56} \tag{2.22}$$

2.3 Analytic Determination of Fatigue Properties and Strain-Life

In section 2.2, five different analytic approaches are presented. The approaches are subsequently referred to as; section 2.2.2 as SN1 and SN2, where SN1 is the strain-life approach and SN2 is the stress-life approach. Approach 1 and 2 of section 2.2.3 as BH1 and BH2, respectively, and section 2.2.1 as FP. By comparing the acquired experimental data of chapter 3 and analytic approaches, it is possible to evaluate whether the analytic models are applicable to this type of welded specimen and load scenario. The approximated fatigue properties of each approach are presented in table 2.2 and are based on monotonic material data in section 1.3. All estimations are based on a Young's modulus E of 198.1 GPa, an ultimate tensile strength σ_{ut} of 495.6 MPa and a Brinell hardness HB of 178.

Comparing the four approaches in table 2.2, it is clear that they do not agree on the transition fatigue life, and consequently a determination of where the transition from plastic to elastic dominance occur is difficult. Each approach is graphical represented in appendix A with elastic, plastic and total strain. The $\varepsilon - N$ of the four approaches are presented in figure 2.3.

	SN1	BH1	BH2	FP
$\sigma_f^{'}$	840.82 MPa	959.1 MPa	981.5 MPa	952.2 MPa
b	-0.099	-0.099	-0.09	-0.089
c	-0.6	-0.6	-0.56	-0.664
$\sigma_y^{'}$	301.32 MPa	NaN	NaN	NaN
$n^{'}$	0.1657	NaN	NaN	0.0757
$K^{'}$	843.986 MPa	NaN	NaN	595.85 MPa
$\varepsilon_f^{'}$	0.9776	0.85555	0.57775	0.7371
N_t	$2.6{\cdot}10^4$	$1.49{\cdot}10^4$	$1.25{\cdot}10^4$	$3.5{\cdot}10^3$
ε_a	$0.0045(2N_f)^{-0.099}$ $+0.9776(2N_f)^{-0.6}$	$0.0045(2N_f)^{-0.099}$ $+0.85555(2N_f)^{-0.6}$	$0.00495(2N_f)^{-0.09}$ $+0.57775(2N_f)^{-0.56}$	$0.0045(2N_f)^{-0.089}$ $+0.7371(2N_f)^{-0.644}$

Table 2.2: Tabular comparison of fatigue properties of the four analytic approaches SN1, BH1, BH2 and FP.

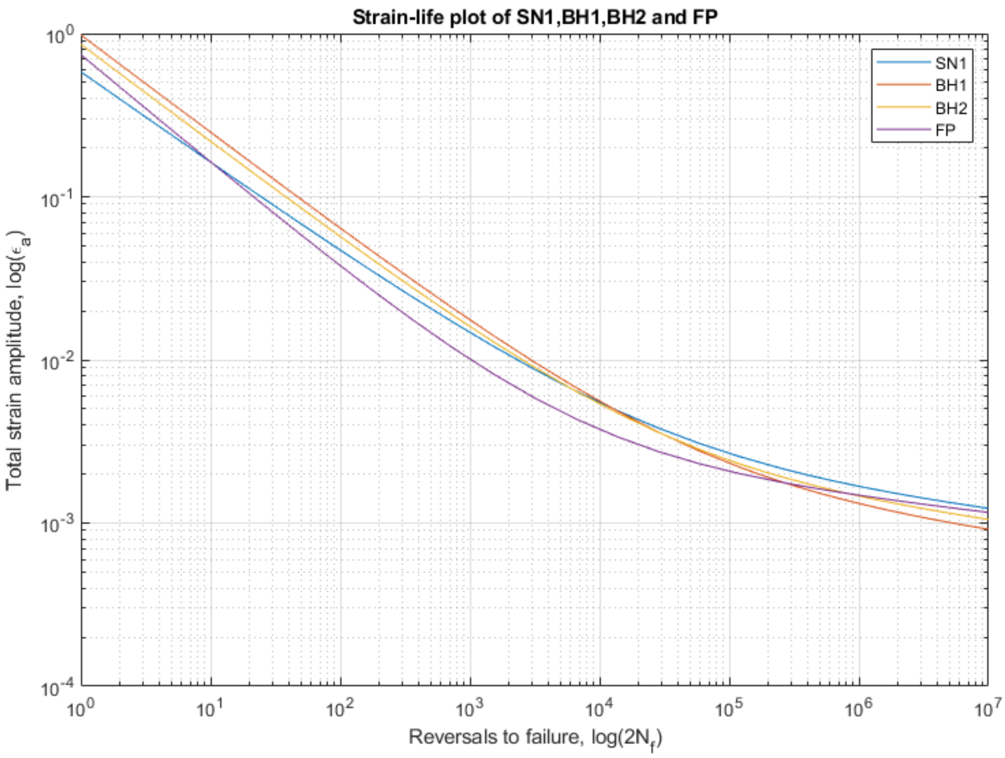

Figure 2.3: Graphical representation of approach SN1, BH1, BH2 and FP.

Experiments 3

In this chapter, the experimental work conducted is presented. This involves documentation of 32 fatigue tests on the butt-welded steel specimen presented in chapter 1, for which strain gauges data, mean values and standard deviations are documented. In addition, hardness tests are conducted, as the models in section 2.2.3 depends on obtained values of hardness. In addition, it is necessary to present the load scenario, see section 3.1. No material properties are investigated in this chapter, as previous documented in section 1.3. The subsequent sections in this chapter are listed in the itemize below.

- Load Scenario - section 3.1
- Schenk 400 kN - section 3.2
- Strain Gauge Experiments - section 3.3
- Experimental Results -section 3.4
- Video Documentation - section 3.5
- Failure Regions - section 3.6
- Brinell Hardness Test - section 3.7
- Microstructure Study - section 3.8

3.1 Load Scenario

To investigate the fatigue properties of the butt-welded steel specimen, a four point bending test is utilized. It is furthermore desired to utilize a fully reversed load, i.e. a stress ratio R of -1, as this define the ratio between minimum and maximum stress. The four point bending test is conducted by utilizing the machine; Schenk 400 kN by Instron. The machine, and the settings utilized, are described in section 3.2, as initially a description of the load scenario is desired. An illustration of the four point bending testing method is depicted in figure 3.1.

Figure 3.1: Illustration of four point bending testing method.

The test involves the specimen being fixed in position by eight rollers, four above and four beneath the specimen. The two center pairs are fixed in position, while the two outer pairs are able to displace vertically. It is assumed no out-of-plane displacement occurs during testing. The addition of rollers enable mobilization of the specimen during testing; effectively ensuring a state of bending in the specimen.

However, position of the contact area between specimen and roller become dependent on the desired displacement of the outer rollers. To furthermore acquire knowledge of the load scenario, a free body diagram, abbreviated FBD, is derived based on a single load, illustrated in figure 3.2.

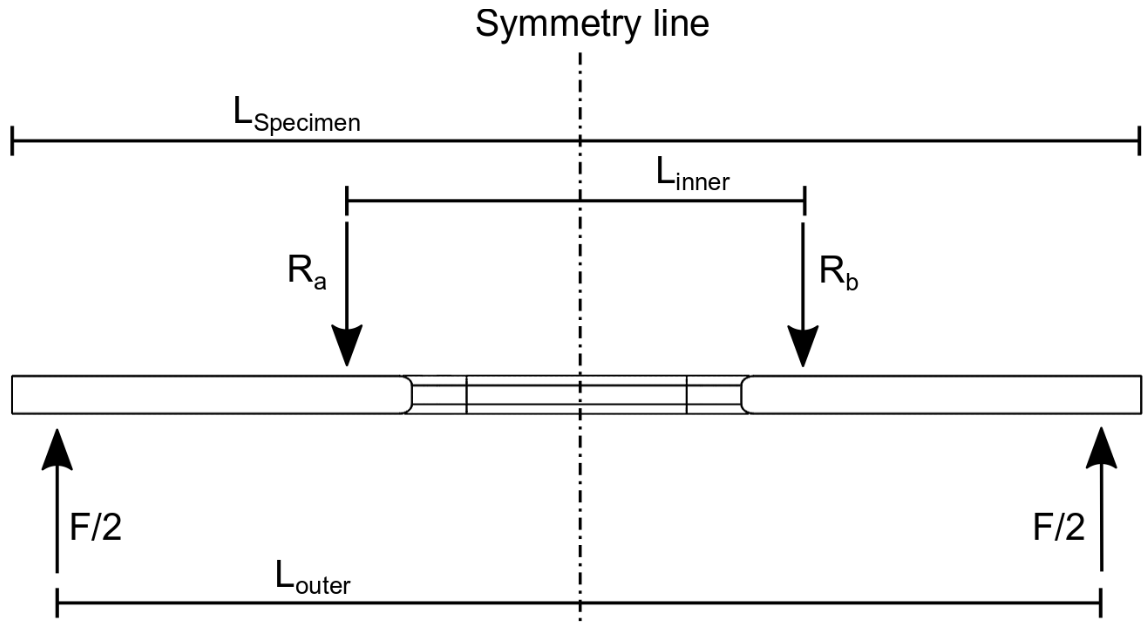

Figure 3.2: FBD of the load scenario. R_a and R_b are equal and corresponds to the applied force F.

Based on the FBD, half-symmetry is applicable, which is advantageous in the Finite Element analysis in chapter 4, as symmetry reduces the computational time. As an understanding of the load scenario is acquired, the equipment utilized to subject the specimen to a state of bending is presented and described in the subsequent section 3.2. The specimen are expected to fail between the two center roller pairs, where a state of bending occur. This is due to the geometrical alterations in the specimen, which induces a reduction of the cross-sectional area.

3.2 Schenk 400 kN

The Schenk 400 kN, presented in figure 3.3, is a servo-hydraulic testing machine available at Aalborg University, capable of both static- and fatigue testing. As the name suggest, it is capable of applying a maximum load of 400 kN. The machine consists of a lower part, where the main actuator of the system is located. In addition, the system consists of a top beam, where the load cell is located. The vertical position of the top beam depends on the two cylinders of the system, which together with the main actuator is controlled by a hydraulic pump.

The PID-controller of the system is utilized to control the main actuator, to subject the specimen to an user-defined load or displacement. The main actuator causes a vertical displacement, which is converted to bending of the specimen by utilizing the four point bending tool presented in figure 3.4. The tool consists of two main parts; an upper and lower part. Both parts aid in fixing the specimen in place by utilizing four pairs of rollers as depicted in figure 3.1. In addition, an end fixture is applied to ensure the specimen is kept in place.

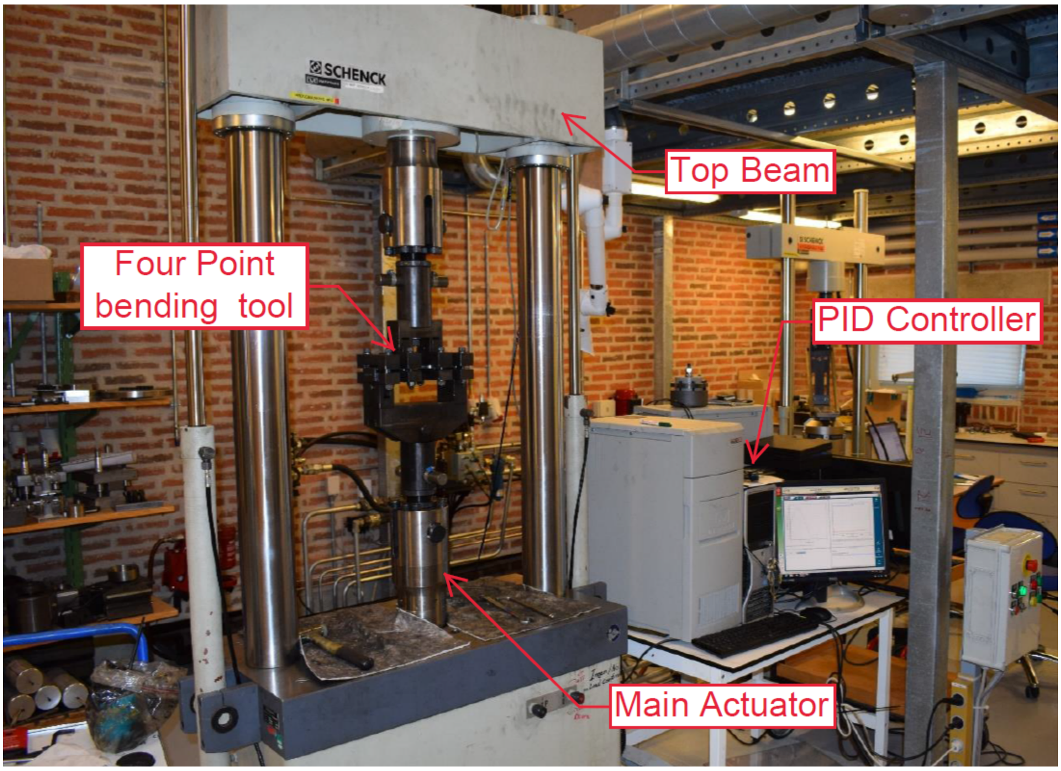

Figure 3.3: Instron Schenk 400 kN with PID controller and bending tool mounted.

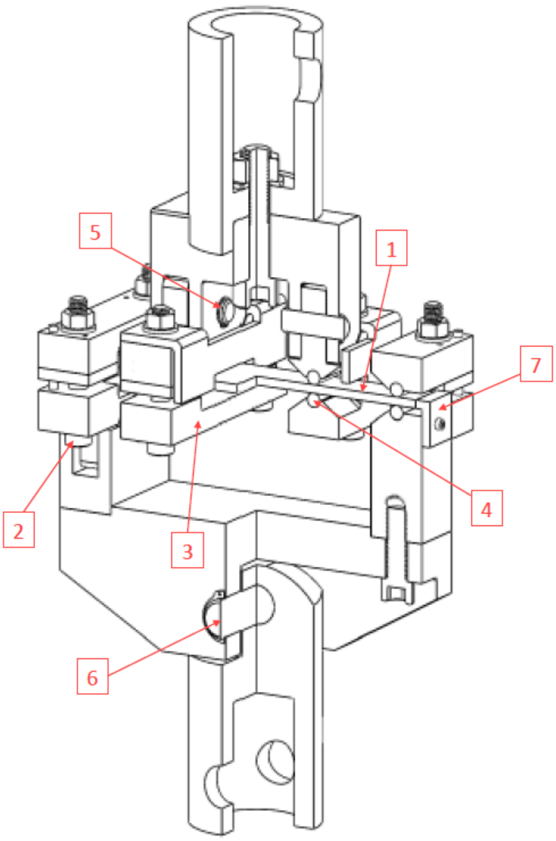

1. Specimen
2. Bolts
3. Clamps
4. Rollers
5. Rotational joint for clamps
6. Rotational joint for tool
7. End fixture

Figure 3.4: Illustration of the four point bending tool, modified [5].

To ensure the rollers enable the specimen to displace, each roller is applied lubricant, grease. Another important aspect in regard to the rollers is the contact between rollers and specimen, as it depends on the clamping of the specimen. If the bolts are tightened extensively, they clamp and limit the movement of the specimen, even with the addition of lubricant. In [5], it is observed that extensive tightening of the bolts could result in a decrease of the applied moment to the specimen. However, if the bolts are loose, the specimen and rollers might experience slippage in the contact region, which induces erroneous test results. Consequently, the process of fastening the bolts are performed with care.

In figure 3.4, the four point bending tool with a specimen attached is displayed. The tool has two rotational joints, marked as nr. 5 and 6 in figure 3.4, which ensures a uniform load across the specimen. The rotational joints are essential in order to ensure a pure state of bending, however, it is evaluated to induce slippage in the system. The slip is identified by a clicking sound when utilizing the tool, which induces a potential error. The slippage is evaluated as wear of the tool. A detailed description of the four point bending tool is presented in appendix D. During testing the utilized software acquires and presents data, which entails a displacement-time curve, a force-time curve and cycles. In addition, the software provides additional data as the tests are concluded. This involves:

- Total time [s]
- Cycle elapsed time [s]
- Total cycles
- Elapsed cycles
- Total cycle count
- Position [mm]
- Applied load [kN]

In the following sections, the data sampling of the software, choice of control and an uncertainty assessment are presented.

3.2.1 Data Sampling

The data acquired during testing is limited to a fixed amount and consequently a satisfying sample frequency is required. The sample frequency should be determined based on the expected life time of the specimen, and frequency of the applied load. When conducting cyclic life time testing, and the generated data is of a significant quantity, it is necessary to pause the tests once or several times to acquire the desired data as the data acquisition of the software is limited. As the data is collected, the test can be resumed and new data is acquired.

3.2.2 Choice of Control

The machine has two types of control; displacement control and load control. Initially, it is desired to utilize load control to ensure a constant force amplitude. However, due to malfunctions, load control can not be utilized, as the machine produces an alarming noise. Consequently, displacement control is utilized. In addition, small errors are detected during initial testing. The applied load at maximum and minimum displacement are not of equal magnitude, resulting in the load not being fully reversed. This is evaluated to be due to slippage between the tool and specimen, and errors in the load cell transducer. Consequently, a brief study of the measured force and displacement is conducted in section 5.4.

3.2.3 Uncertainty Assessment

When performing experimental work, uncertainties are present and must be accounted for. The raw data acquired by the software consists of maximum and minimum values of both force and displacement, which each are assigned an array. Data is recorded to enable determination of empirical mean value $\vec{x}$ of both force and displacement. The empirical mean value further enable determination of the empirical standard deviation $s(x)$. These are determined in accordance with [17]. The formulation of the empirical mean value is presented in equation 3.1 and the empirical standard deviation in equation 3.2.

$$\vec{x} = \frac{\sum x_i}{n} \tag{3.1}$$

$$s(x) = \sqrt{\frac{\sum (x_i - \vec{x})^2}{n-1}} \tag{3.2}$$

$\vec{x}$	Empirical mean value	n	Number of measured data points
$s(x)$	Empirical standard deviation	x	Measured data

3.3 Strain Gauge Experiments

In this section, the data acquisition during fatigue testing utilizing strain gauges is documented. The data acquired is utilized to validate the FE-model presented in chapter 4. In total, seven specimen are tested with strain gauge attached; specimen 3, 11*, 21, 32, 36*, 42 and 47. However, due to several errors regarding attachment and data acquisition, only four of the strain gauge provided usable data. This is further documented in section 3.4.2. The placement of strain gauges is desired a sufficient distance away from weld and roundings as depicted in figure 3.5. All strain gauges utilized in this study are rosette gauges. The rosette gauges consists of three gauges in a 0°, 45° and 90° configuration, as presented in figure 3.6. The rosette gauges are attached so 0° and 90° correspond to the x- and y-axis, respectively, depicted in figure 3.7.

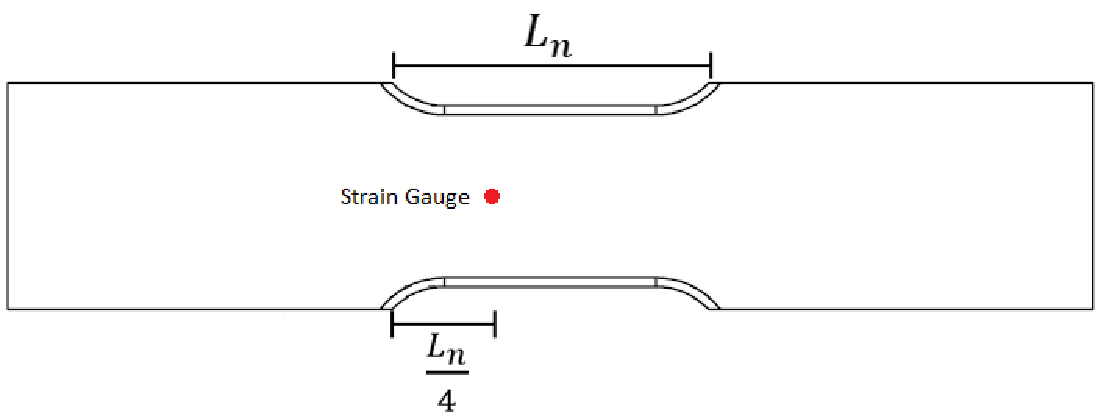

Figure 3.5: Illustration of strain gauge placement, where L_n is the length between the roundings.

To ensure a satisfactory adhesion between rosette gauge and specimen, the strain gauge attachment guide at Aalborg University is utilized, which is presented step-wise below.

1. Removal of oil, grease and other impurities by utilizing acetone
2. Mark strain gauge placement
3. Scrub with M-line Rosin Solvent
4. Wipe dry from center to edge with cotton fabric
5. Repeat 3 and 4 until cotton fabric is unblemished
6. Prepare clean area on gauge box Clean tweezers with M-line Rosin Solvent
7. Position gauge and soldering terminals on box and pick up gauge with tape
8. Position gauge and soldering terminals on specimen
9. Peel back tape (Shallow angle)
10. Apply catalyst and wait 30 seconds
11. Apply and spread adhesive by applying thumb pressure (1 minute)
12. Wait 2 minutes then peel away tape (roll back over itself)

Once the rosette gauge and the soldering terminals have been attached to the specimen as depicted in figure 3.6, the rosette gauge is soldered to the terminals to establish a stable connection to the data acquisition system, abbreviated DAQ. The DAQ utilized in this study is the Spider8-30/SR30 strain gauge amplifier, abreviated Spider-8. The rosette gauge is connected in a Wheatstone quarter bridge configuration, which results in one measurement of each of the three gauges. The Wheatstone bridge is presented in section 3.3.1.

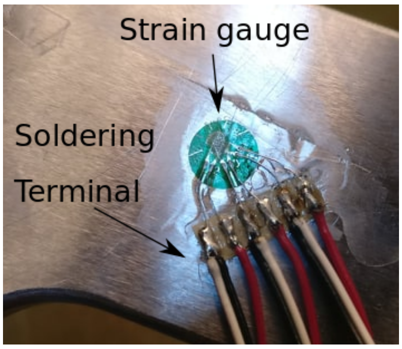

Figure 3.6: Rosette gauge attached to specimen with soldering terminals and wires.

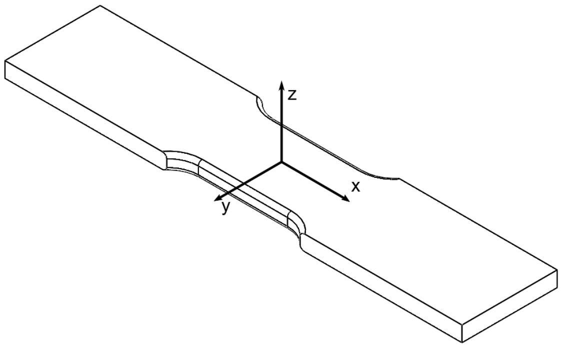

Figure 3.7: Illustration of specimen with the defined coordinate axis.

3.3.1 Data Processing

The Spider-8 is measuring the change in resistance occurring when the strain gauge is exposed to deformation. The change in resistance is converted to change in voltage utilizing the Wheatstone Bridge equation. The linearized Wheatstone Bridge formulation in equation 3.3 is utilized, where a linear relation between resistance and voltage is assumed.

$$\frac{V_0}{V} = \frac{1}{4}\left(\frac{\Delta R_1}{R_1} - \frac{\Delta R_2}{R_2} + \frac{\Delta R_3}{R_3} - \frac{\Delta R_4}{R_4}\right) = \frac{1}{4}\frac{\Delta R_{SG}}{R_{SG}} \tag{3.3}$$

The strain gauges are wired in a quarter bridge configuration, ensuring no change in resistance occur in three of the four resistors; i.e. $\Delta R_2 = \Delta R_3 = \Delta R_4 = 0$. Consequently, the change in voltage is only dependent on a single resister; R_1, which is redefined as R_{SG}. To balance the Wheatstone Bridge, the resistance of the three aforementioned resistors are set equal to the resistance of the strain gauge. The change in voltage is converted to strain by utilizing the gauge factor, k, provided by the strain gauge manufacturer as 2.14 [23]. The correlation between strain and change in resistance is presented in equation 3.4, and inserted into equation 3.3, yielding equation 3.5.

$$k\epsilon = \frac{\Delta R_{SG}}{R_{SG}} \tag{3.4}$$

$$\frac{V_0}{V} = \frac{k}{4}\varepsilon \tag{3.5}$$

The Spider-8 gathers data of all three gauges in the rosette gauge, which is separated into arrays of maximum and minimum values of each cycle. The data acquired is measured in $\frac{mV}{V}$, which is converted to $\frac{\mu m}{m}$ by applying a factor of 10^{-3}. In order to obtain the strain components, ε_{xx}, ε_{xy} and ε_{yy}, the rosette gauge equation presented in equation 3.6 is utilized.

$$\varepsilon(\theta) = \varepsilon_{xx}cos^2(\theta) + \varepsilon_{yy}sin^2(\theta) + 2\varepsilon_{xy}sin(\theta)cos(\theta) \tag{3.6}$$

Recall, the gauges 0° and 90° are aligned according to the x- and y-axis depicted in figure 3.7, respectively. However, due to alignment difficulties of the rosette gauges, the orientation of the gauges are prone to deviate. Consequently, principal strains and angles are determined utilizing Mohr's Circle [16], as the principal directions are defined along the x- and y-axis. The principal strains are utilized to validate the FE-model in section 5.1, while the principal angle is utilized to account for possible misalignment, providing more accurate strain components. This enables the determination of equivalent strain according to [26], which is utilized in the desired strain-life curves presented in section 5.2.

3.3.2 Errors During Testing

In the fatigue tests conducted with rosette gauges attached, several errors are encountered. The connection of the 0° gauge is terminated during testing with large displacements, which is evaluated to be due to failure of adhesion. Furthermore, the encountered strains could exceed the measuring range of the Spider-8, which is approximately $\pm 25.000\mu$ strain according to [17]. In addition to failure of adhesion, the soldering is prone to failure during large displacement. Consequently, only partial data is acquired during these tests. The loss of connection or exceeding the measuring range of the Spider-8 results in a spike in the acquired data.

3.3.3 Uncertainty Assessment

An uncertainty assessment of the data is presented in this section. The Law of Accumulation presented in equation 3.7 [17] is utilized to evaluate the uncertainty.

$$s(R) = \sqrt{\left(\frac{\partial R}{\partial x}s(x)\right)^2 + \left(\frac{\partial R}{\partial y}s(y)\right)^2 + \left(\frac{\partial R}{\partial z}s(z)\right)^2 + ... + \left(\frac{\partial R}{\partial n}s(n)\right)^2} \tag{3.7}$$

R	Function for calculated values
$x, y, z, .., n$	Statistical variables in R

Utilizing the formulation in equation 3.7, the uncertainty of R is determined. Mean values have been utilized for the statistical variables in the derivatives, e.g. $\frac{\partial R}{\partial x}$, to determine the standard deviation of the data. Recall from section 3.3.1, the gauge factor k is 2.14 with a tolerance of ± 1%. The relative uncertainty of the gauge factor is determined as $\frac{1}{2}$ of the tolerance, i.e. $\frac{s(k)}{k} \approx 0.5$ %. If the measured strain is in the range of ± 5000 $\mu strain$, the uncertainty of ≈ 0.025 % induced by the linearized Wheatstone Bridge formulation and ≈ 0.05 % of the Spider-8 can be neglected. As several measurements exceed the strain range, these uncertainties, of ≈ 0.056 % [17], are accounted for in equation 3.8.

$$\frac{s(\varepsilon)}{\varepsilon} = \sqrt{(-1 \cdot 0.5\%)^2 + (+1 \cdot 0.056\%)^2} = 0.5031\% \tag{3.8}$$

The determined uncertainty of equation 3.8 is utilized for all strain calculations presented in section 3.4.

3.4 Experimental Results

In this section, the experimental results acquired by the Schenk 400 kN and strain gauges are presented. All results are based on empirical mean values according to equation 3.1 and presented in tables throughout this section.

3.4.1 Schenk 400 kN Results

Results acquired by the Schenk 400 kN are presented in table 3.1, and in appendix C. All specimen numbers with * symbolizes specimen type 1 presented in section 1.1.1. The specimen numbers without * are specimen type 2 presented in section 1.1.2. The specimen number -1 originally lacked a number due to manufacturing error, consequently being assigned -1. In addition, specimen -1 has a flaw in the fillet, visible in figure 3.8. This manufacturing error reoccurs in specimen 12*, 22, 32* and 43.

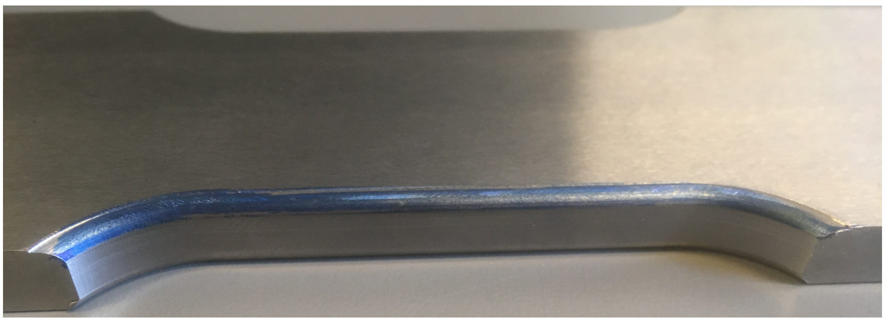

Figure 3.8: Image of error in fillet occurring in specimen -1, 12*, 22, 32* and 43.

Specimen 12* and 28* are utilized to calibrate the PID controller, and consequently subjected to loading before fatigue testing. The loading is deemed to influence the results, which is to be considered if deviations are observed. The calibration are conducted on specimen type 1, as the two specimen types have approximately equal stiffness and deemed to not influence the results. The fatigue test and calibration of specimen 12* is conducted utilizing load control during the initial phase of the study. The errors of load control, however, became evident during testing of specimen 5*. The fatigue test of specimen 12* is deemed satisfying, though the results of specimen 5* are unreliable. This is detectable in table 3.1 in which specimen 5* has a shorter lifetime than specimen 6*, even though specimen 6* is subjected to a larger displacement. Consequently, displacement control is utilized. In addition, specimen 1* has been removed and re-inserted in the machine multiple times due to a high cyclic life. In table 3.1; N is cycles to failure, d is displacement, R is ratio and F is force. a and m refers to amplitude and mean, respectively.

SP Numb	**N [Cycle]**	$\mathbf{d_a}$ **[mm]**	$\mathbf{R_d}$ **[-]**	$\mathbf{F_a}$ **[kN]**	$\mathbf{R_F}$ **[-]**	$\mathbf{F_m}$ **[kN]**
1*	460018	1.48 ± 0.03	-1.00 ± 0.03	3.64 ± 0.30	-1.01 ± 0.17	0.01 ± 0.30
48	97787	1.97 ± 0.04	-1.00 ± 0.04	4.18 ± 0.11	-1.09 ± 0.06	-0.18 ± 0.11
18	25410	2.42 ± 0.02	-1.00 ± 0.015	4.74 ± 0.29	-0.89 ± 0.11	0.26 ± 0.29
46*	21000	2.52 ± 0.02	-1.00 ± 0.01	5.19 ± 0.45	-1.08 ± 0.19	-0.19 ± 0.45
3	17103	2.77 ± 0.04	-1.00 ± 0.03	5.06 ± 0.27	-1.15 ± 0.13	-0.32 ± 0.27
26	12746	2.85 ± 0.13	-1.00 ± 0.09	5.43 ± 0.70	-0.81 ± 0.22	0.51 ± 0.70
42	12085	2.99 ± 0.03	-0.98 ± 0.02	5.20 ± 0.35	-0.89 ± 0.12	0.30 ± 0.35
9*	8847	3.03 ± 0.03	-1.00 ± 0.02	5.91 ± 0.40	-1.01 ± 0.14	-0.04 ± 0.40
2	7744	3.27 ± 0.04	-1.00 ± 0.02	5.58 ± 0.30	-0.89 ± 0.10	0.33 ± 0.30
36*	7744	3.28 ± 0.04	-1.00 ± 0.02	6.06 ± 0.50	-0.95 ± 0.16	0.12 ± 0.50
16	5566	3.52 ± 0.01	-1.00 ± 0.01	5.40 ± 0.34	-1.12 ± 0.14	-0.27 ± 0.34
22	3384	4.04 ± 0.002	$-1.000.002$	5.73 ± 0.34	-0.93 ± 0.13	-0.13 ± 0.34
35	2732	4.52 ± 0.05	-1.00 ± 0.02	6.11 ± 0.32	-1.04 ± 0.11	-0.10 ± 0.32
-1	1741	5.05 ± 0.08	-1.00 ± 0.03	6.16 ± 0.46	-1.12 ± 0.16	-0.19 ± 0.46
14*	1732	5.05 ± 0.08	-1.00 ± 0.03	6.16 ± 0.46	-1.12 ± 0.16	-0.19 ± 0.46
15	1256	5.51 ± 0.002	-1.00 ± 0.0006	6.24 ± 1.05	-1.13 ± 0.35	-0.18 ± 1.05
12*	685	5.96 ± 0.28	-0.76 ± 0.08	7.79 ± 0.25	-0.89 ± 0.06	0.44 ± 0.25
4*	848	6.06 ± 0.06	-1.00 ± 0.02	7.92 ± 0.58	-1.04 ± 0.15	-0.17 ± 0.58
40	846	6.56 ± 0.08	-1.00 ± 0.02	6.95 ± 0.40	-1.04 ± 0.12	-0.13 ± 0.40
11	585	7.06 ± 0.17	-1.00 ± 0.05	7.89 ± 0.55	-1.05 ± 0.15	-0.19 ± 0.55
28*	755	7.07 ± 0.08	-1.00 ± 0.02	8.05 ± 0.54	-0.99 ± 0.13	0.02 ± 0.54
32*	773	7.07 ± 0.0004	-1.00 ± 0.0001	7.73 ± 0.43	-1.03 ± 0.11	-0.12 ± 0.43
41	550	7.29 ± 0.52	-0.98 ± 0.14	7.57 ± 1.24	-0.88 ± 0.30	0.36 ± 1.24
25	486	8.06 ± 0.18	-1.00 ± 0.05	7.58 ± 0.48	-1.05 ± 0.13	-0.17 ± 0.48
5*	118	8.24 ± 0.68	-1.14 ± 0.18	8.57 ± 0.23	-0.97 ± 0.05	0.16 ± 0.23
50	411	8.98 ± 0.23	-1.00 ± 0.05	7.99 ± 0.50	-1.05 ± 0.13	-0.20 ± 0.50
47	270	10.05 ± 0.34	-1.00 ± 0.07	9.53 ± 0.75	-1.06 ± 0.17	-0.29 ± 0.75
45	218	11.03 ± 0.55	-0.99 ± 0.10	8.75 ± 0.77	-0.92 ± 0.17	0.31 ± 0.77
6*	120	12.12 ± 0.001	-1.00 ± 0.0002	12.25 ± 0.76	-0.80 ± 0.10	1.35 ± 0.76
43	110	13.04 ± 0.62	-0.99 ± 0.10	9.09 ± 0.82	-1.06 ± 0.19	-0.33 ± 0.82
21	178	14.11 ± 0.0003	-1.00 ± 0.00004	9.02 ± 0.80	-0.99 ± 0.18	0.03 ± 0.80
24	129	15.06 ± 0.66	-0.99 ± 0.09	10.08 ± 0.66	-1.07 ± 0.14	-0.36 ± 0.66

Table 3.1: Results acquired by Schenk 400 kN; * refers to specimen type 1.

3.4.2 Strain Gauge Results

Results acquired by strain gauges are presented in tables, entitled with specimen number and displacement amplitude throughout this section. E.g. the results of specimen 3 at a displacement amplitude of 2.77 mm is presented in table 3.2. The entries of the tables are presented below. 1st and 2nd Reversal in the tables refers to the first and second reversal of a cycle.

- Strain gauge data; ε_{0°, ε_{45° and ε_{90°
- Rosette equation data; ε_{xx}, ε_{xy} and ε_{yy}
- Principal strain; ε_1 and ε_2
- Principal angles; θ_1 and θ_2
- Equivalent strain; ε_{equiv}

Specimen 3 at 2.77mm			
Title	**Amplitude**	**Mean**	**Ratio[-]**
$\varepsilon_1[10^{-6}]$	2916.66 ± 10.37	-18.41 ± 10.37	-1.01 ± 0.007
$\varepsilon_2[10^{-6}]$	-786.71 ± 2.81	-58.17 ± 2.81	-
ε_{equiv} $[10^{-6}]$	2177.08 ± 6.43	27.27 ± 4.29	-
-	**1st Reversal**	**2nd Reversal**	**-**
$\varepsilon(0^\circ)$ $[10^{-6}]$	2893.92 ± 14.56	-2934.88 ± 14.77	-
$\varepsilon(90^\circ)$ $[10^{-6}]$	-840.54 ± 4.23	728.37 ± 3.66	-
$\varepsilon(45^\circ)$ $[10^{-6}]$	899.52 ± 4.53	-1129.16 ± 5.68	-
ε_{xx} $[10^{-6}]$	2893.92 ± 14.56	-2934.88 ± 14.77	-
ε_{yy} $[10^{-6}]$	-840.54 ± 4.23	728.37 ± 3.66	-
ε_{xy} $[10^{-6}]$	-127.17 ± 8.83	-25.90 ± 9.49	-
$\theta_1[rad]$	-0.01700 ± 0.00465	0.00354 ± 0.00518	-
$\theta_1[deg]$	-0.97 ± 0.27	0.20 ± 0.30	-
$\theta_2[rad]$	1.55380 ± 0.00465	1.57433 ± 0.005180	-
$\theta_2[deg]$	89.03 ± 0.27	90.20 ± 0.30	-

Table 3.2: Strain gauge results of specimen 3 at 2.77 mm displacement amplitude.

Specimen 42 at 5 mm	
	1st Reversal
$\varepsilon(0^\circ)$ $[10^{-6}]$	6278.45 ± 31.59
$\varepsilon(90^\circ)$ $[10^{-6}]$	-3138.99 ± 15.79
$\varepsilon(45^\circ)$ $[10^{-6}]$	2211.33 ± 11.13
ε_{xx} $[10^{-6}]$	6278.45 ± 31.59
ε_{xy} $[10^{-6}]$	641.60 ± 20.87
ε_{yy} $[10^{-6}]$	-3138.99 ± 15.79
$\varepsilon_1[10^{-6}]$	6321.96 ± 31.57
$\varepsilon_2[10^{-6}]$	-3182.50 ± 15.97
$\theta_1[rad]$	0.03386 ± 0.00415
$\theta_1[deg]$	$1.94^\circ \pm 0.24^\circ$
$\theta_2[rad]$	1.60465 ± 0.004153
$\theta_2[deg]$	$91.93^\circ \pm 0.24^\circ$
ε_{equiv} $[10^{-6}]$	5520.65 ± 20.79

Table 3.3: Strain gauge results of specimen 42 at 5 mm displacement amplitude.

Specimen 42 at 4.5 mm	
	1st Reversal
$\varepsilon(0^\circ)$ $[10^{-6}]$	4905.34 ± 24.68
$\varepsilon(90^\circ)$ $[10^{-6}]$	-2609.50 ± 13.13
$\varepsilon(45^\circ)$ $[10^{-6}]$	1712.42 ± 8.62
ε_{xx} $[10^{-6}]$	4905.34 ± 24.68
ε_{xy} $[10^{-6}]$	564.50 ± 16.42
ε_{yy} $[10^{-6}]$	-2609.51 ± 13.13
$\varepsilon_1[10^{-6}]$	4947.51 ± 24.44
$\varepsilon_2[10^{-6}]$	-2651.67 ± 13.28
$\theta_1[rad]$	0.03728 ± 0.00404
$\theta_1[deg]$	$2.14^\circ \pm 0.23^\circ$
$\theta_2[rad]$	1.60808 ± 0.00404
$\theta_2[deg]$	$92.14^\circ \pm 0.23^\circ$
ε_{equiv} $[10^{-6}]$	4409.57 ± 16.43

Table 3.4: Strain gauge results of specimen 42 at 4.5 mm displacement amplitude.

In tables 3.3 to 3.5, the strain gauge results of specimen 42 are presented. Initially, a displacement amplitude of 5 mm is desired. However, data spiking is observed in the second reversal of each cycle and test is terminated after 10 cycles. Consequently, the displacement amplitude is lowered to a value of 4.5 mm. However, spiking reoccurs and the displacement amplitude is lowered to 3 mm, where no spiking occurs. Consequently, only the 3 mm displacement amplitude acquired data of both cycles, while tests with 5 and 4.5 mm displacement amplitude lacked data of the second reversal. When evaluating the data of specimen 42 in table 3.4 and 3.5, effect of pre-displacement must be considered. In addition, the strain gauge is balanced before each test is initiated, inducing further errors as whether the specimen is at rest is unknown.

Specimen 42 at 3mm			
Title	**Amplitude**	**Mean**	**Ratio [-]**
$\varepsilon_1[10^{-6}]$	2999.67 ± 10.60	15.49 ± 10.60	-0.99 ± 0.007
$\varepsilon_2[10^{-6}]$	-969.27 ± 3.51	-7.15 ± 3.51	-
$\varepsilon_{equiv}\ [10^{-6}]$	2324.55 ± 6.65	13.18 ± 6.61	-
-	**1st Reversal**	**2nd Reversal**	**-**
$\varepsilon(0°)\ [10^{-6}]$	2995.91 ± 15.07	-2964.43 ± 14.91	-
$\varepsilon(90°)\ [10^{-6}]$	-957.17 ± 4.82	942.37 ± 4.74	-
$\varepsilon(45°)\ [10^{-6}]$	1295.96 ± 6.52	-1289.49 ± 6.49	-
$\varepsilon_{xx}\ [10^{-6}]$	2995.91 ± 15.07	-2964.43 ± 14.91	-
$\varepsilon_{yy}\ [10^{-6}]$	-957.17 ± 4.82	942.37 ± 4.74	-
$\varepsilon_{xy}\ [10^{-6}]$	276.59 ± 10.25	-278.46 ± 10.16	-
$\theta_1[rad]$	0.03476 ± 0.00484	0.0354 ± 0.00484	-
$\theta_1[deg]$	1.99 ± 0.28	2.03 ± 0.28	-
$\theta_2[rad]$	1.60556 ± 0.00484	1.60620 ± 0.00484	-
$\theta_2[deg]$	91.99 ± 0.28	92.03 ± 0.28	-

Table 3.5: Strain gauge results of specimen 42 at 3 mm displacement amplitude.

Specimen 36* at 3.25mm			
Title	**Amplitude**	**Mean**	**Ratio**
$\varepsilon_1[10^{-6}]$	3980.03 ± 14.15	-92.05 ± 14.16	-1.05 ± 0.007
$\varepsilon_2[10^{-6}]$	-1042.08 ± 3.72	-9.26 ± 3.72	-
$\varepsilon_{equiv}\ [10^{-6}]$	2954.13 ± 8.77	51.62 ± 8.77	-
-	**1st Reversal**	**2nd Reversal**	**-**
$\varepsilon(0°)\ [10^{-6}]$	3887.75 ± 19.56	-4068.37 ± 20.47	-
$\varepsilon(90°)\ [10^{-6}]$	-1051.12 ± 5.29	1029.12 ± 5.18	-
$\varepsilon(45°)\ [10^{-6}]$	1385.22 ± 6.97	-1657.07 ± 8.34	-
$\varepsilon_{xx}\ [10^{-6}]$	3887.75 ± 19.56	-4068.37 ± 20.47	-
$\varepsilon_{yy}\ [10^{-6}]$	-1051.12 ± 5.29	1029.12 ± 5.18	-
$\varepsilon_{xy}\ [10^{-6}]$	-33.10 ± 12.30	-137.44 ± 13.45	-
$\theta_1[rad]$	-0.00335 ± 0.00498	0.01347 ± 0.00522	-
$\theta_1[deg]$	-0.19 ± 0.29	0.77 ± 0.30	-
$\theta_2[rad]$	1.56745 ± 0.00498	1.58426 ± 0.00522	-
$\theta_2[deg]$	89.81 ± 0.29	90.77 ± 0.30	-

Table 3.6: Strain gauge results of Specimen 36* at 3.25 mm displacement amplitude.

The results presented in table 3.6 are the only full data set for specimen type 1. Data for specimen 32* is limited due to a faulty gauge, consequently no measurements of $\varepsilon(0°)$ are available rendering the data unusable. Whether the faulty gauge is a result of poor attachment, manufacturing or shipping is unknown. The remaining specimen tested with strain gauges; 11*, 21 and 47 resulted in erroneous data acquisition as a results of the aforementioned errors in section 3.3.2.

3.5 Video Documentation of Experiments

Initially, it is desired to document the fatigue tests by video, to evaluate the crack growth during cyclic loading, with the desire of implementing Paris' Equation. To capture video of the fatigue, a capture device is utilized and positioned next to the Schenk 400 kN, capturing images as displayed in figure 3.9. During testing the crack of some specimen initiated on the upper surface of the specimen. To document this, a further capture device; a GoPro, is set up. However, aligning the GoPro to the surface is not possible, and consequently the captured images of crack growth are skewed. In addition, the crack size must be converted from pixel to mm. The misalignment of GoPro and conversion induce errors to the evaluation of the crack growth. Furthermore, during the fatigue testing kinking of the cracks are observed, indicating mixed mode behaviour, consequently rendering Paris' Equation invalid.

Figure 3.9: Image of a loaded specimen with visible crack propagation.

3.6 Failure Regions

The failure regions and fracture surfaces are investigated to evaluate possible causes of failure, based on observations. Three recurring failure regions are identified and depicted in figure 3.10 along with weld and HAZ. The failure regions are illustrated by three colored lines; red, green and dark blue. The weld and HAZ are depicted by utilizing the method described in section 1.2.4.

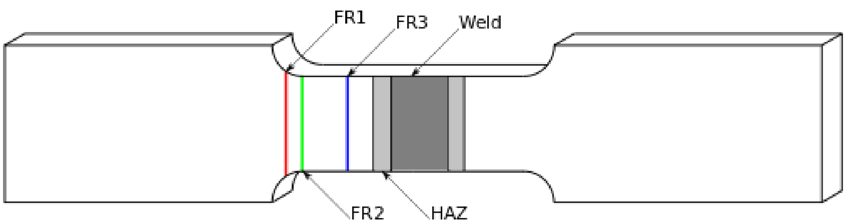

Figure 3.10: Illustration of specimen with weld, HAZ and failure regions depicted.

The red failure line, defined as Failure Region 1; FR1, occurs in the rounding in which the cracks typically form at the edges of the notch and grows towards the center. The green failure lines, FR2, occur approximately at the transition of the rounding, for which the crack growth occurs at the edges and the middle. As both red and green failure regions are in the vicinity of a notch, geometrical stress concentrations are deemed present, which could result in these failure locations. This is further evaluated in chapter 6. In addition, the dark blue failure lines, FR3, occur between the rounding and HAZ, which is evaluated to be due to fatigue and possibly the microstructure at this region. Figure 3.11 illustrates a failure at FR3, where the microstructure of the oxidized surface is visible.

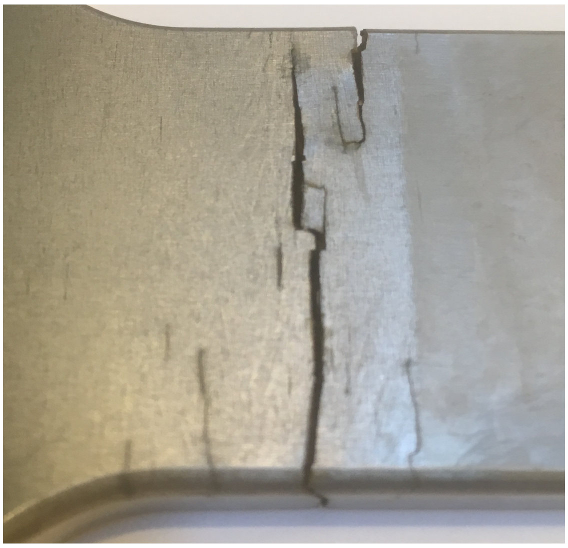

Figure 3.11: Close-up at FR3 of failed specimen with oxidized surface to render weld and HAZ visible.

Figure 3.12: Upper surface = FS3, Middle surface = FS2, Bottom Surface = FS1.

In addition to the observed failure regions, the fracture surfaces are investigated to evaluate whether microstructural changes have occurred due to the welding process. Three fracture surfaces are observed as presented in figure 3.12 and defined as; FS1, FS2 and FS3. The failure regions and fracture surfaces of each specimen are presented in table 3.7. The observed fracture surfaces do not exhibit the identifying marks of a typical fatigue failure surface, where distinct crack nucleation sites, beach marks and a final fracture region is observed [12].

In the bottom of table 3.7, a total count of each failure region is presented. In total, 32 specimen are utilized for fatigue testing, whereas 9 have failed at FR1 $\approx$ 28%, 9 at FR2 $\approx$ 28% and 14 at FR3 $\approx$ 44%. Consequently, geometrical stress concentrations could possibly account for more than 50 % of the failures.

This is undesired, as fatigue life could be influenced by crack initiation based on geometrical stress concentrations. As the specimen have not been manufactured by this project group, this is unavoidable and, consequently, it is important to distinguish the data acquired at the three failure regions, as this could explain possible deviations in data. This is accounted for in chapter 5.

Specimen Number	FR1	FR2	FR3	FS1	FS2	FS3
1*	X			X		
48			X		X	
18	X				X	
46*		X			X	
3			X			X
26		X		-	-	-
42			X			X
9*	X				X	
2	X			-	-	-
36*	X			X		
16			X			
22		X		X		
35		X		X		
-1			X			X
14*		X			X	
15		X			X	
12*			X			X
4*			X			X
40		X		X		
11*			X			X
28*			X	X		
32*	X				X	
41	X				X	
25		X			X	
5*		X			X	
50			X			X
47			X			X
45			X			X
6*			X			X
43			X			X
21	X				X	
24	X				X	
Total	9	9	14	6	12	11

Table 3.7: Overview of the different types of fracture encountered in the experiments. Specimen 2 and 26 are not evaluated with respect to fracture surface, as these specimen are kept together. Specimen are sorted according to displacement.

3.7 Microstructure Study

A brief microstructure study, initiated by results acquired in section 3.6 and figure 3.11, is conducted to investigate whether thermal effects of the welding process possibly affected the microstructure of the base material. The equipment utilized and preparation of the specimen are presented in section 3.7.1 followed by the results presented in section 3.7.2.

3.7.1 Equipment and Preparation of Specimen

The method of section 1.2.4 is deemed insufficient for microscopy, consequently resulting in a new method. The specimen is divided into three smaller parts by utilizing the cut-off machine Discotom 6 at Aalborg University in figure 3.14. The positioning of the cuts are illustrated in figure 3.13. The center part, containing the weld, is investigated, as failures occurs within this region. The surface of the part is wet sanded as presented in figure 3.15 and subsequently polished. As initial images captured through the microscope are unsatisfying, electropolishing is utilized. Pitting occur due to electropolishing, however, the images captured are satisfying and presented in section 3.7.2. All images are captured by an AxioCam at Aalborg University.

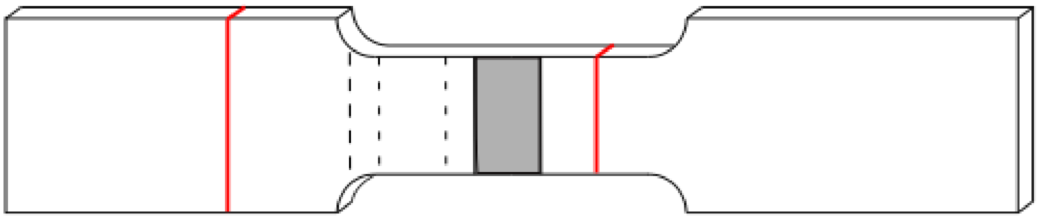

Figure 3.13: Cut-off lines in red and failure regions marked by dashed lines.

Figure 3.14: Discotom 6 by Struers.

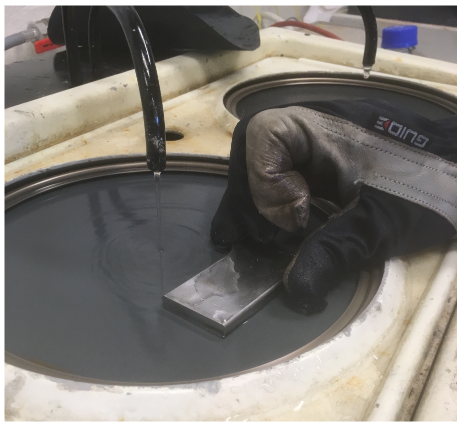

Figure 3.15: Wet sanding of test piece.

3.7.2 Microstructure of Specimen

During inspection of microstructure a possible cause of failure for FR3 is observed. Initially, the grain-like pattern in figure 3.11 is deemed as part of the HAZ. However, the HAZ is limited to the dark area next to the weld. Inspecting this region closer, it is evaluated that the pattern is due to pearlite, see figure 3.16. The α-ferrite, cementite Fe_3C and pearlite are depicted in figure 3.17; ferrite in black, cementite in blue, pearlite band in red and the presence of a microcrack in green. Note, the pearlite is laying in a band along the width of the specimen in the observed failure region. Consequently, the material is more brittle in this region, which could result in failure at this region. Small bands of pearlite and cementite are observed throughout the specimen, however, not of a similar magnitude. Consequently, the idea of microstructural changes due to weld in the notched region is rejected, as the temperature is below any phase transformation temperature.

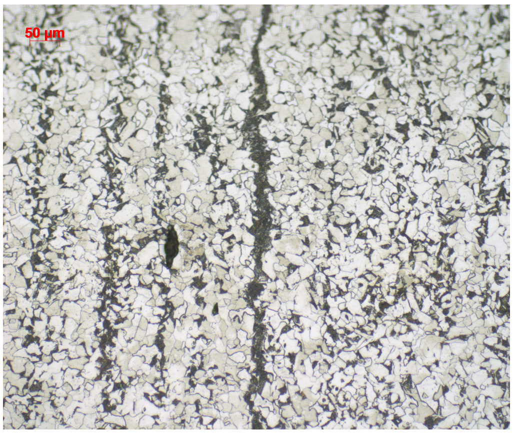

Figure 3.16: Microstructure of specimen at failure region adjacent to HAZ.

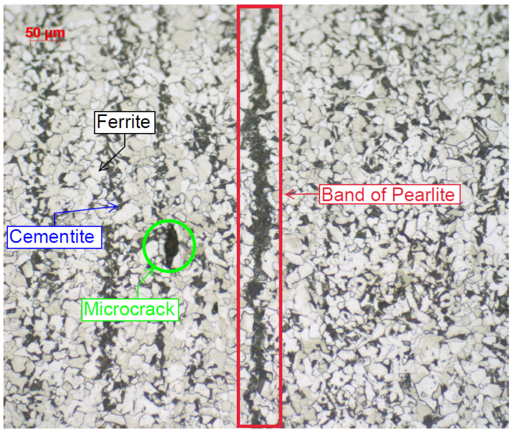

Figure 3.17: Identified microconstituents.

According to [9], the occurrence of pearlite bands indicates that in the initial solidification process, when steel is cooled from molten state, where ferrite is formed, inclusions of manganese sulphides; MnS, and other elements, are formed throughout the material. These phases induce some degree of anisotropy within the material, as they pertain high concentrations of MnS. The subsequent deformations occurring during hot rolling draw out the phases, and consequently align phases of MnS along the rolling direction, as the pearlite bands observed in figure 3.17. The direction of MnS bands is responsible for the toughness being dependent on orientation, hence cross rolling of the material can mitigate the orientation dependency of MnS.

3.8 Brinell Hardness

In section 2.2.3, expressions to determine properties such as the ultimate tensile strength S_{ut} and fatigue ductility coefficient $\varepsilon_f^{'}$ is presented as functions of the Brinell hardness. In general, hardness is a measure of how resistant of wear a material is. The linear relationship between hardness and ultimate tensile strength for steels is expressed in equation 3.9 [13].

$$S_{ut} = 3.45BH \pm 0.2BH \tag{3.9}$$

The standard methods of defining hardness are Brinell, Vicker and Rockwell, where it is desired to focus on the Brinell hardness in this study. However, a Brinell hardness test machine is not available and a Rockwell hardness testing machine is utilized instead to determine the hardness. The hardness tests of this study are conducted with Rockwell B and Rockwell C, which is converted to Brinell hardness.

The Rockwell B, abbreviated HRB, utilizes a 1.6 mm diameter steel ball, which is pressed down on the surface of the test specimen. The Rockwell C, abbreviated HRC, utilizes a cone rather than a steel ball. The load of the indenter corresponds to 100 kg for HRB and 150 kg for HRC. The hardness is determined based on the depth of the indentation t. The Rockwell hardness is determined as presented in equation 3.10 and 3.11, respectively [15]. In addition, the two types of Rockwell hardness testing are illustrated in figure 3.18.

$$\mathrm{HRB} = 130 - 500t \tag{3.10}$$
$$\mathrm{HRC} = 100 - 500t \tag{3.11}$$

HRB	=	Rockwell Hardness B	P	=	Load
HRC	=	Rockwell Hardness C	t	=	Indentation

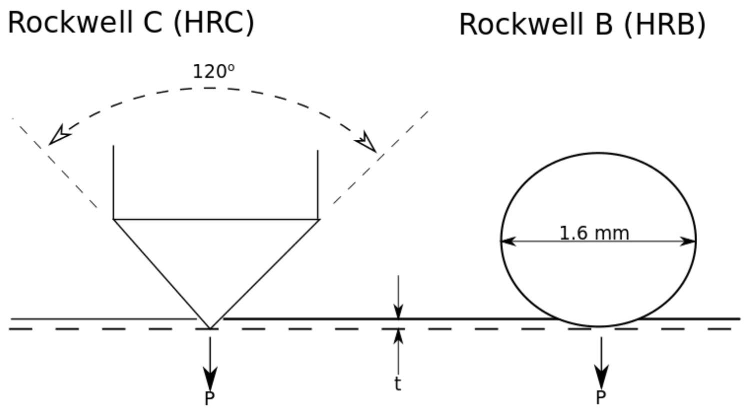

Figure 3.18: Illustration of Rockwell C and Rockwell B testing methods. Load of Rockwell C (HRC) is 150 kg, while Rockwell B (HRB) is 100kg.

3.8.1 Experimental Testing

To acquire the HRB and HRC values of the test specimen, a Wilson Rockwell testing machine is utilized. Upon selection of a Rockwell test type, the display indicates which indenter, minor and major load to utilize. The specimen is placed on the platform and height is adjusting until the minor load display is set. As the test is conducted, the machine calculates the hardness based on the indentation. Three specimen surfaces are utilized to determine the hardness, defined as 14S1 (HRC testing), 14S2_1 (HRB testing) and 14S2 (HRC testing). The acquired hardness values are presented in table 3.8.

	14S1 (26 points)	14S2_1 (20 points)	14S2 (15 points)
Average	4.55 HRC	4.49 HRC	88.64 HRB
Brinell Hardness	≈ 167 HB	≈ 167 HB	≈ 178 HB

Table 3.8: Tabular of hardness.

Numerous tests are conducted on each surface to provide a mean value of the hardness. Not all points are utilized due to large deviations, e.g. 14S1. The hardness is afterwards converted to Brinell hardness by utilizing conversion table and charts presented in [13] and [15], respectively. Note, the conversion is rough and troublesome, consequently resulting in approximated hardness values. The data is available in appendix B.

Finite Element Model 4

In this chapter, the Finite Element Model, abbreviated FE-model, is presented, which is in parts based on: [19], [10] and [24]. The intention of establishing a FE-model is to yield an approximation of the stresses and strains encountered in the specimen during loading, enabling conversion of acquired displacement amplitude-life data to stress- and strain-life data. The model consists of a structural analysis simulating the experiments from chapter 3. Utilizing the constitutive relations pertaining to the material; S355J2, the stresses are determined. Upon obtaining strains and stresses for both types of specimen, a validation of the FE-model is presented in section 5.1.

The FE-model is established on the monotonic responses of the experiments, i.e. one reversal of a cycle, as no fatigue behaviour is modeled. In order to accurately simulate in a FE-context, a static structural non-linear analysis is performed; as non-linearties are present in the model. A non-linear approach is utilized when stresses, i.e. loading, are expected to exceed the linear elastic region of the material, which is refereed to as material non-linearity. This is one of the three main sources of non-linearities, which furthermore includes geometric non-linearities, if the model pertain large displacements or rigid body rotations, and contact non-linearity, where bodies are in contact. Consequently, all three main sources of non-linearities are present in the model.

Throughout the project, Abaqus, Ansys Workbench and SolidWorks have been addressed. Ultimately, Abaqus is utilized for the FE-analysis. Before the actual FE-analysis is documented, the reader is acquainted with the theoretical aspects and notations utilized throughout FE-analysis. The subsequent sections in this chapter are listed in the itemize below.

- Finite Element Theory - section 4.1.
- Initial Finite Element Analysis - section 4.2
- Non-linear Finite Element Analysis - section 4.3
- Results - section 4.4

4.1 Finite Element Theory

Finite element is a method of computing engineering analysis, which utilizes a numerical approach in order to solve the governing equations applicable to real world problems. The governing differential equations are divided into solvable approximated expressions, capable of being handled by the numerical solvers. Therefore in structural analysis the FE-method is an immense powerful tool, where systems with very high degrees of freedom are solvable. The FE-analysis yield an approximation of the actual system investigated through interpolation.

4.1.1 Non-Linearities

A FE-model of the experiment is desired, and in order to model a four point bending utilized for LCF, which is plastically dominated, several non-linearties are required implemented in the model to acquire the appropriate results. The properties of a linear system, presented in the itemize below, is utilized to describe how a non-linear system differs from a linear system.

- The principle of superposition is valid
- Linearized constitutive equations
- Linearized geometric equations
- Internal forces equal external forces

The principle of superposition is invalid in a non-linear system, i.e. a non-linear problem can not be divided into sub-problems, which are solved individually and summarized to yield the full solution. The expressions of the geometric- and constitutive equations in a linear system are displayed in equations 4.1 and 4.2, respectively. These expressions are, in collaboration with the assumption of force equivalency, utilized to describe the internal and external forces, which is displayed in equation 4.3.

$$\{\epsilon\} = [B]\{d\} \tag{4.1}$$
$$\{\sigma\} = [E]\{\epsilon\} \tag{4.2}$$
$$\{R^{int}\} = \{R^{ext}\} \qquad \longrightarrow \qquad [K]\{d\} = \{R^{ext}\} \tag{4.3}$$

$\{\varepsilon\}$	=	Strain vector	$[E]$	=	Young's modulus
$[B]$	=	Strain-displacement matrix	$\{R^{int}\}$	=	Internal forces
$\{d\}$	=	Displacement vector	$\{R^{ext}\}$	=	External forces
$\{\sigma\}$	=	Stress vector	$[K]$	=	Stiffness matrix

In a non-linear systems the stiffness becomes dependent on the displacements, rendering the linearized expressions invalid. Consequently, a non-linear formulation is sought, as displayed in equation 4.4.

$$[K(x)]\{x\} \quad = \quad \{F\} \tag{4.4}$$

Where $\{x\}$ is displacement and $\{F\}$ is load. In a non-linear approach the input and output can not be expected to exhibit a linear relationship, i.e. doubling the applied load is not expected to yield a doubling of displacement. Hence a non-linear analysis requires an iterative solution as the relation between load and displacement is unknown.

4.1.2 Structural Non-Linearities

The non-linearities considered in this project are the structural non-linearities. The three main sources of non-linearities in a structural analysis are:

- Geometric non-linearities
- Material non-linearities
- Contact non-linearities

Each structural non-linearity pertain to the FE-model established in this project. In addition, plasticity is pertained to the model.

Geometric Non-Linearities

A geometrical non-linear problem has two main attributes of non-linearities; a non-linear strain definition and equilibrium equations are formulated on the deformed configuration. Such non-linearities occur when deformations, or rotations, are large. The non-linear strain definition, i.e. the Green-Lagrange strain definition ε_G displayed in equation 4.5, is a higher order strain definition utilized when large displacements are present. The Cauchy formulation of strain, i.e. engineering strain ε_E, where displacements are related to the undeformed configuration, are inadequate in defining problems containing large displacements. Consequently, the Green-Lagrange formulation is utilized by Abaqus.

$$\varepsilon_G = \frac{L^2 - L_0^2}{2L_0^2} = \varepsilon_E + \frac{1}{2}\varepsilon_E^2 \tag{4.5}$$

The aforementioned non-linearities are taken into account when defining the slope of a force-displacement response; the tangent stiffness K_T. The tangent stiffness is explicitly written in equation 4.6.

$$[K_T] = [K_0] + [K_L(d)] + [K_\sigma] \tag{4.6}$$

Where $[K_0]$ is the linear stiffness matrix, which is updated in relation to the deformed configuration by $[K_L(d)]$, and K_σ takes into account the stress stiffening effect.

Material Non-Linearities

A material model is an implementation of a constitutive equation into a FE-analysis, and if the applied load is sufficient to exceed the elastic limit of the defined material, the non-linear plastic region is reached. Plasticity is a non-linear phenomena and in order to account for plasticity an appropriate material model is required. Metals, which exhibit ductile behaviour, are well suited to an elastic-plastic material model, i.e. S355J2. In an elastic-plastic material model, both a linear elastic region and an non-linear plastic region are modeled, as illustrated in figure 4.1. Figure 4.1 depicts a ductile material response with elastic strain region ε_{el} and plastic strain region ε_{pl}. Energy is dissipated due to plastic deformations, however upon unloading the elastic strain is re-gained as elastic energy.

Contact Non-Linearities

A problem formulation with contact is highly non-linear as typically the contact region changes, i.e. stiffness of the system changes depending on boundary. When defining contact pairs in Abaqus, each surface is assigned as either a master or slave surface, where the stiffer surface is assigned as master surface. Abaqus defines both tangential and normal behaviour as illustrated in figure 4.2.

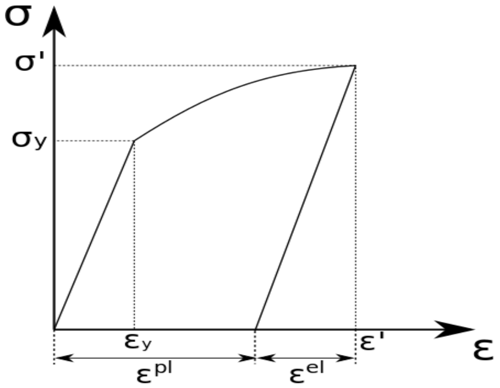

Figure 4.1: Illustration of an elastic-plastic material response.

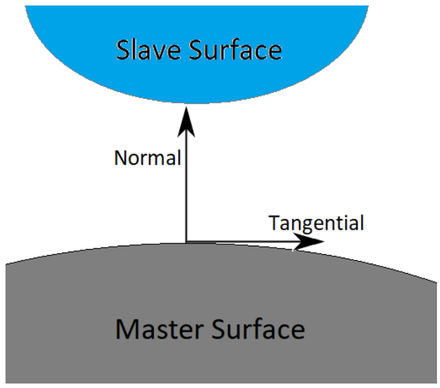

Figure 4.2: Illustration of interface between two surfaces.

In contact problems two physical phenomena should be fulfilled: conservation of momentum and compatibility between colliding surfaces, i.e. no penetration. However, often these requirements are only approximately fulfilled [19]. Two methods of contact are often formulated in FE-software;

- The penalty method
  - Implements an artificial stiffness in the contact interface, where the magnitude of the interface stiffness is significantly higher that structural stiffness. The method fulfills conservation of momentum, however, a small penetration is always present.
- The Lagrange multiplier
  - Adds an additional variable to the system, which exactly fulfills compatibility, as the added variable describes the kinematic behaviour, i.e. the contact force. However, conservation of momentum is not necessarily fulfilled.

The implementation of contact in Abaqus is documented in section 4.3.3.

4.1.3 Newton-Raphson Solution Method

As previously documented the stiffness, and perhaps additionally the force, in a non-linear analysis is dependent on displacement, as displayed in equation 4.4. The solution requires an iterative process, as a direct solver apporach is insufficient. Several non-linear solution methods exist, where the Newton-Raphson procedure is chosen and documented in this section. Newton-Raphson is the most widely utilized iterative scheme in commercial FE-software. Unless specifically altered by the user, the standard solution method in Abaqus is the Newton-Raphson, or a variation of it.

The Newton-Raphson scheme utilizes the inherent forces of a non-linear system to determine displacements from applied loads. The applied load is divided into a predetermined set of load steps, f_n, of which the displacement increment, δd, is determined by evaluating the force imbalance in the system, i.e. the residual in equation 4.7. A single load step is illustrated in figure 4.3.

$$r(d, f) = p(d) - f = 0 \tag{4.7}$$

Where r is the force residual, $p(d)$ is the internal forces which is dependent on displacement d, f is the external forces. Initially, the actual load displacement curve, in figure 4.3, is unknown and ultimately the solver yield a set amount of equilibrium points throughout the curve in figure 4.3. At every load step n the displacement increment is determined through an iterative process, and assessed in accordance with the residual force imbalance. To evaluate the displacement increment, the tangent stiffness in equation 4.6 is utilized in combination with the incremental equilibrium equation displayed in equation 4.8.

$$K_T(d_i^n)\delta d_i^n \quad = \quad -r_i^n \tag{4.8}$$

This enables the current displacement step, d_i^n, to be updated by the incremental displacement step, δd_i^n, yielding the future step as presented in equation 4.9.

$$d_{i+1}^n \quad = \quad d_i^n + \delta d_i^n \tag{4.9}$$

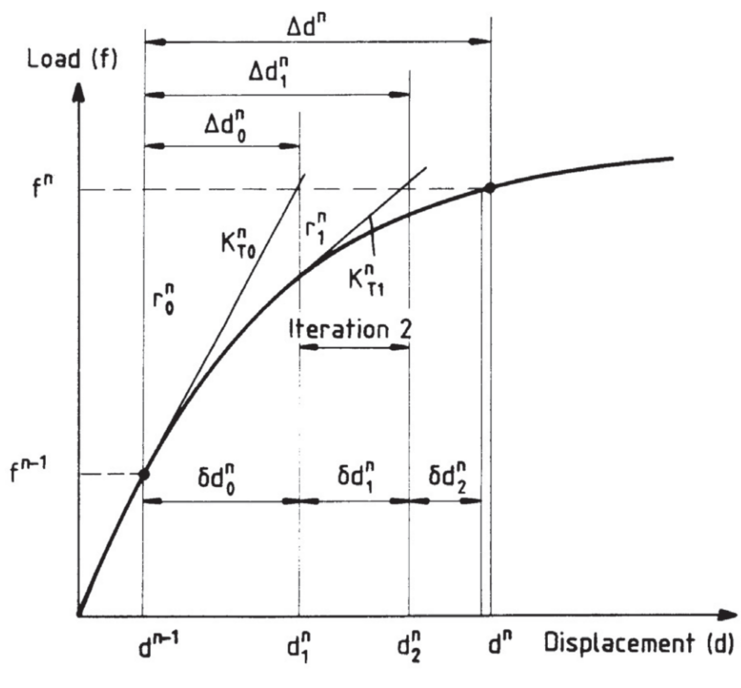

Figure 4.3: Illustration of the Newton-Raphson procedure [19].

4.2 Initial Finite Element Analysis

A simplified FE-analysis is conducted, where geometric non-linearties are excluded and a linear material model is utilized. The simplified analysis serves as a reference point to the non-linear model, providing understanding of the non-linear effects and to evaluate results and furthermore to investigate geometric stress concentrations introduced by the roundings. The model utilizes identical modelling parameters; elastic material properties, geometry, half-symmetry and boundary conditions. The modeled specimen is depicted in figure 4.4 and the rollers of the system are modeled as in figure 4.5. Partitions, the black lines, are implemented to place boundary conditions and simplify meshing. Do note, the linear static analysis pertain the contact between roller and specimen.

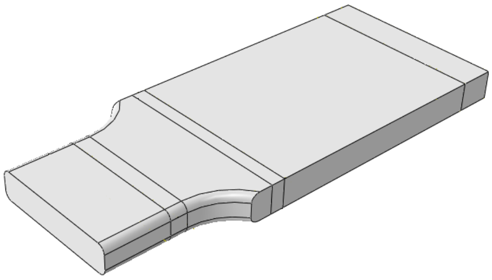

Figure 4.4: The specimen modeled in Abaqus.

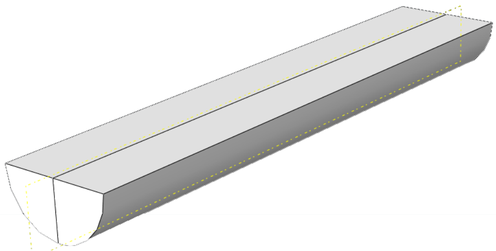

Figure 4.5: The rollers modeled in Abaqus.

The half-symmetry FE-model with applied boundary conditions is illustrated in figure 4.6. The model consists of the specimen and two rollers, where contact is applied between each roller and specimen. The regions, where boundary conditions are applied, are numerated and described in the itemize below.

1. Symmetry boundary condition, symmetry surface constrained in x-axis.
2. Fixed boundary condition of stationary roller, surface fixed in all directions and rotations.
3. Transverse boundary condition at node, model fixed in y-axis.
4. Fixed boundary condition on displaced roller, surface fixed in x- and y-axis.
5. Reference point constrained to surface of displaced roller, displacement applied in negative direction of z-axis.

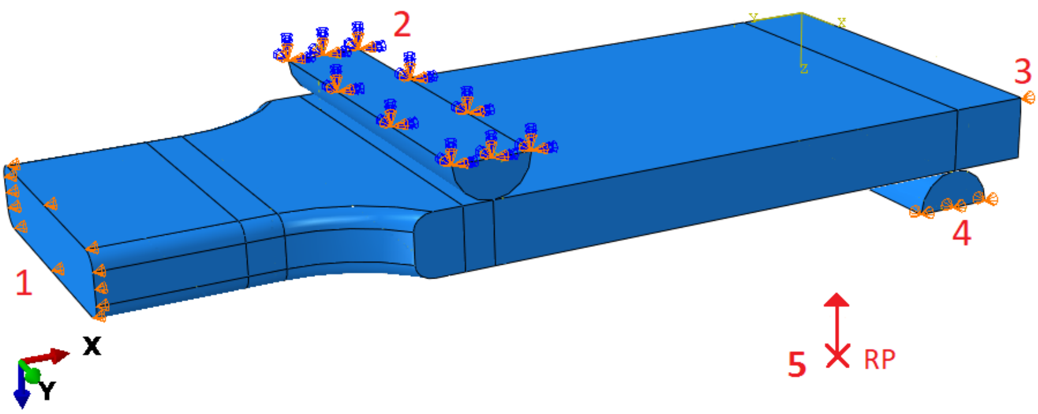

Figure 4.6: The FE-model illustrated with numerated boundary conditions.

To uphold the symmetry conditions, the surface at 1 in figure 4.6 is constrained in the x-axis, which ensures symmetry is applied correctly. To represent the experimental setup, the specimen is fixed in the y-axis at point 3, a node, consequently resulting in no transverse displacement of the specimen is allowed. Point 3 is selected a sufficient distance from the region of interest to ensure the constraint is not interfering with the data acquired at this region. In addition, the surface at 2 is fixed, while the surface at 4 is constrained in the x- and y-axis, consequently allowing displacement in z-axis. The desired displacement is applied in collaboration with the reference point 5 constrained with the roller, which is implemented to simplify the output controls of the analysis, i.e. utilizing a single point to sum up the reaction forces. Displacement control is applied, through a user defined amplitude, which is loaded and unloaded stepwise.

4.2.1 Investigation of Stress Concentrations

The presence of geometric stress concentrations are investigated and presented with Von Mises stress plots in figure 4.7 and 4.8. In the figures, the geometric stress concentrations are visible in red and are in accordance with the fracture regions encountered in section 3.6.

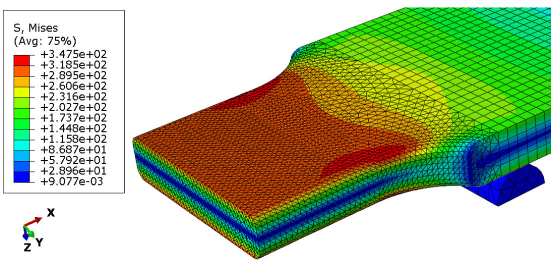

Figure 4.7: FE-analysis illustrating geometric stress concentration.

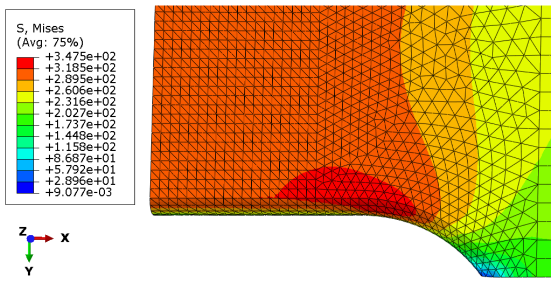

Figure 4.8: Close-up of region with geometric stress concentration.

4.3 Non-Linear Finite Element Analysis

In low-cycle fatigue applications, the applied loads are of a significant magnitude to induce plastic deformation for which a non-linear analysis is necessary. The load utilized is defined through displacement control, which aid the non-linear solver to converge. In the subsequent sections, the analysis settings utilized are presented. The settings are displayed in the itemize below in the order of which the model is established.

- Geometric Modeling - Section 4.2
- Boundary Conditions - Section 4.2
- Material Model - Section 4.3.1
- Mesh and Elements - Section 4.3.2
- Assembling Model
- Contact Formulation - Section 4.3.3
- Step and Analysis Settings - Section 4.3.4
- Output of results - Section 4.4

4.3.1 Material Model

The material model is based on input from a tensile test of the material; S355J2, where isotropic hardening is assumed. Material of same batch is not available and data of [25] is utilized, as documented in section 1.3. The data, however, induces problems with respect to stress-strain beyond the yield point. The problem is solved by utilizing the material calibration tool in Abaqus to create a full material response rather than separately defining an elastic and plastic region.

The material model utilized in modeling the specimen is defined as an elastic-plastic within Abaqus. The elastic-plastic material model in Abaqus is based on the von Mises stress criterion. The material model utilized for the rollers are modeled as an isotropic linear elastic material with a significant magnitude of stiffness, in relation to the stiffness of the specimen.

4.3.2 Elements and Meshing

In this section, the choice of elements and mesh is presented. These choices affects the computational time, which is an imporant aspect when performing a FE-analysis. The element formulation utilized in the FE-model is solid elements, where two different element formulations of the solids elements are considered; hexahedral and tetrahedral elements. Quadratic formulations of both elements are illustrated in figures 4.9 and 4.10, respectively.

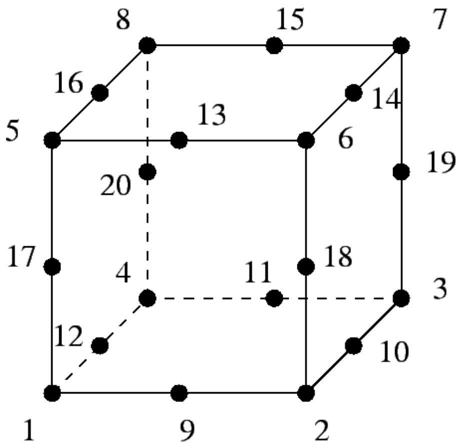

Figure 4.9: Quadratic 20-node hexahedral element; C3D20 in Abaqus [27].

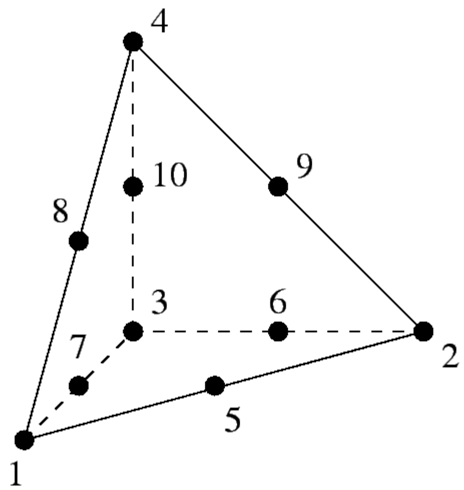

Figure 4.10: Quadratic 10-node tetrahedral element; C3D10 in Abaqus [28].

In order for the meshing tool in Abaqus to mesh the full geometry, tetrahedral elements are required to revolve around the circular shape of the fillet. According to [29], the linear formulation of the tetrahedral element is not recommended, as it yields unacceptable approximations in bending dominated problems. However, the quadratic formulation, which is a 10-node element, is well suited for bending problems. Additionally, the quadratic hexahedral, a 20-node element, is well suited, though computational heavy. The linear hexahedral, an 8-node element, is suited as well, though in bending shear locking can induce complications. Tetrahedral elements increase the amount of elements in the model relative to hexahedral elements. For this reason, hexahedral elements are desired to reduce computational time. However, in combination with the tetrahedral elements, utilized for the fillet, incompatibility at the interface of the two meshed regions is introduced. Consequently, tie constraints are applied between the meshed regions.

Based on obtained results, and computational time, the quadratic hexahedral element with reduced integration is utilized; C3D20R. Additionally quadratic tetrahedral element is utilized; C3D10.

Element Size

In order to approximate the model to some degree of accuracy without computational time prohibiting the flow of the analysis, an appropriate element size is required. The Abaqus academic teaching license available at AAU offers a maximum of 250000 nodes, which sets a natural restriction on the element size of the model, however, the computational time when reaching the limiting number of nodes is extensive. Therefore a mesh convergence study is performed to determine the required element size to acquire acceptable results. A local mesh sizing is utilized in the region of interest; the mesh region pertaining tetrahedral elements in figure 4.13. Throughout the mesh convergence study the hexahedral mesh region is applied a constant element size of of 2 mm. The element size of the tetrahedral elements are the only altered variable, and values of maximum principal stress and strain are obtained; in the region of strain the gauge placement. The study is conducted utilizing a displacement of 2.77 mm. The results are depicted in figures 4.11 and 4.12, plotting maximum principal stress and strain, respectively. Table 4.1 display the further obtained values.

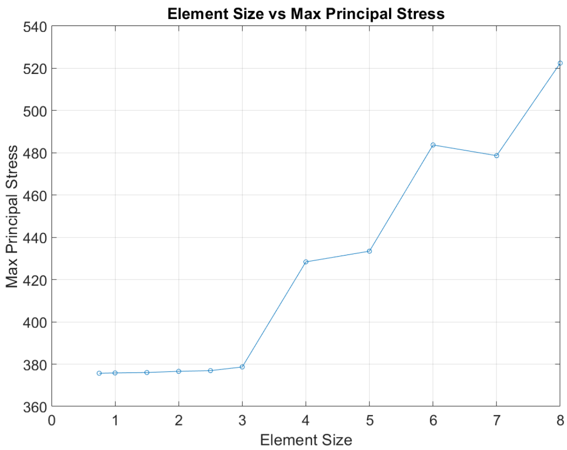

Figure 4.11: Maximum principal stress plotted against element size for 2.77 mm displacement.

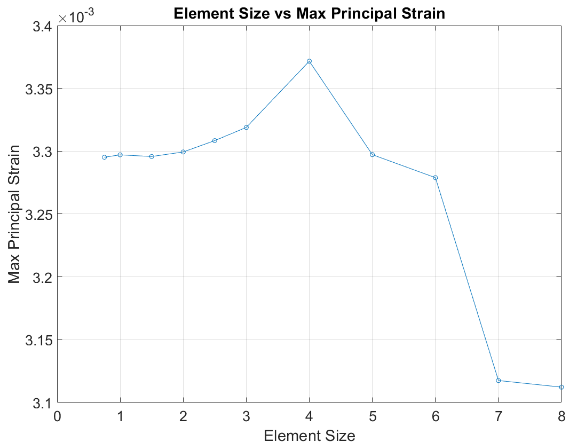

Figure 4.12: Maximum principal strain plotted against element size, for 2.77mm displacement

Based on obtained values an element size of 2 mm is utilized, as values of stress and strain are within acceptable margins, and the computational time is manageable. The FE-model is depicted in figure 4.13. The accuracy of the FE-model in relation to obtained strain gauge results are evaluated in section 5.1.

Element Size [mm]	Max. Principal Stress [MPa]	Max. Principal Strain [10^{-6}]	Number of Elements [-]
0.75	375.714	3295.21	147553
1	375.843	3297.08	102204
1.5	376.048	3295.78	30180
2	376.608	3299.37	16937
2.5	376.943	3308.43	12163
3	378.672	3318.91	9842
4	428.4	3371.63	7921
5	433.455	3297.24	7077
6	483.725	3278.93	6437
7	478.658	3117.48	6067
8	522.454	3112.22	5565

Table 4.1: Obtained values of the mesh convergence study for 2.77 mm displacement.

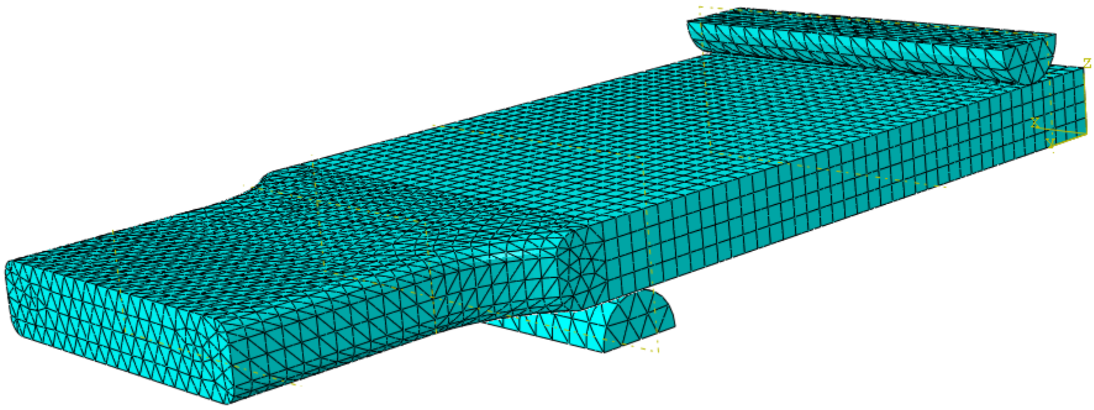

Figure 4.13: Meshed FE-model utilizing an element size of 2 mm.

4.3.3 Contact Formulation

In Abaqus, the surface to surface contact formulation is utilized in modeling contact between the specimen and two rollers. The rollers, which consist of the stiffer material, are set as the master surface, consequently the specimen is set as slave surface. The tangential behaviour is set to frictionless, as the computational time increase if friction is considered. The model is investigated with a frictional coefficient of lubricated steel, which induced a negligible difference in the desired outputs. Consequently a frictionless tangential behaviour is deemed an adequate approximation. The normal behaviour is defined as hard contact utilizing the augmented Lagrange formulation, which utilizes the penalty method and the Lagrange multiplier method, which are presented in section 4.1.2.

4.3.4 Solution Controls

This section discusses the solver settings applied for the analysis, utilizing the step approach pertaining to Abaqus. The maximum number of increments is set to the default value of 100, where the initial increment size is altered from a default value of 1 to 0.25. This results in the load being divided into a maximum of 100 load steps, while the maximum load in the initial increment is limited to a quarter of the actual load applied. The utilized solver applies the initial increment and the required iterations of the Newton-Raphson approach are conducted. If the solver does not converge to a solution, utilizing the initial load step, it divides the initial incremental size by a factor of two, i.e. a new size of 0.125. This process continues until the minimum allowable increment size is reached or converges.

4.4 Results

With the presented settings, Abaqus converges to a solution and the desired output controls of the model are listed in the itemize below.

- Von Mises stress
- Principal strain components
- Reaction force of the displaced roller

All output controls are defined across all nodes in the model. In order to obtain results in the region where strain gauges are attached, a path is defined, displayed in figure 4.14. The path intersects with the strain gauge position on the specimen, i.e. 17.5 mm from the symmetry boundary face.

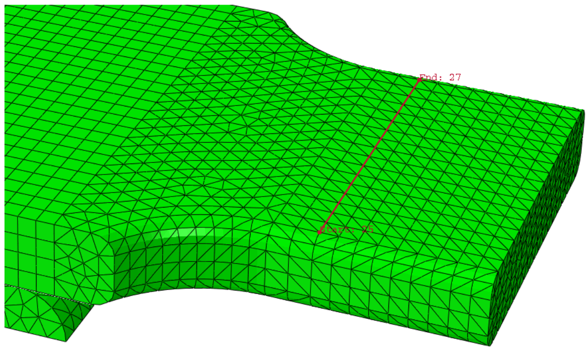

Figure 4.14: Path where output controls are defined across.

All outputs are defined from the applied inputs, i.e. the displacement ranging 1-16 mm. All outputs, with the exception of reaction force, are obtained in the middle of the defined path. The output of reaction force is determined from the displaced roller utilizing the reference point, visible in figure 4.6 as point 5. To illustrate the deformed configuration of the specimen, a displacement of 4 mm is applied and the Von Mises stress plot is displayed in figure 4.15.

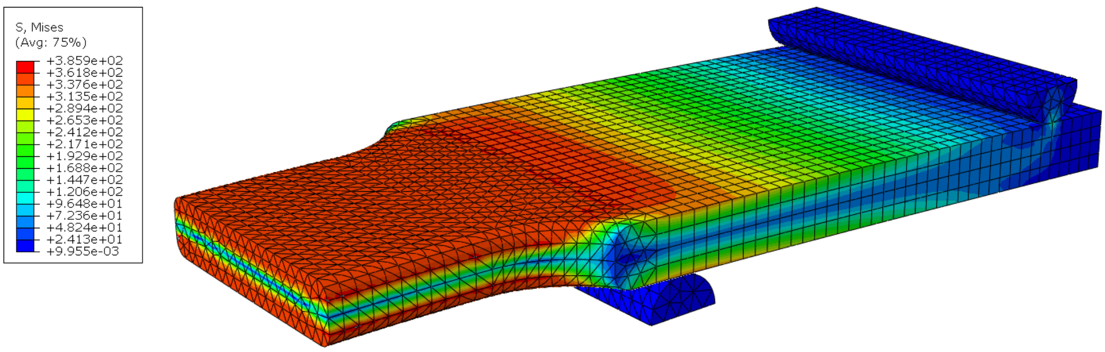

Figure 4.15: The FE-model plotted with Von Mises stress for 4 mm displacement.

The results obtained in Abaqus of both types of specimen are presented in tables 4.2 and 4.3, respectively.

Displacement [mm]	Max. Principal Strain [10^{-6}]	Min. Principal Strain [10^{-6}]	Von Mises Stress [MPa]	Reaction Force [N]
1	1002	-305	197.77	-1293
2	1893	-604	356.56	-2579
3	3509	-1568	358.79	-3204
4	5186	-2612	361.23	-3405
5	6867	-3667	363.70	-3543
6	8615	-4782	366.34	-3658
7	10365	-5907	369.19	-3700
8	12096	-7019	372.57	-3733
9	13810	-8132	375.94	-3759
10	15503	-9228	379.50	-3786
12	18899	-11392	391.64	-3843
14	21136	-13417	405.31	-3891
16	25213	-15364	415.67	-3991

Table 4.2: FE-outputs of specimen type 1.

Displacement [mm]	Max. Principal Strain [10^{-6}]	Min. Principal Strain [10^{-6}]	Von Mises Stress [MPa]	Reaction Force [N]
1	1036	-314	204.53	-1233
2	2129	-738	357.40	-2440
3	3698	-1682	358.79	-2989
4	5432	-2761	362.36	-3157
5	7233	-3900	364.22	-3287
6	9083	-5082	367.24	-3366
7	10941	-6280	370.25	-3420
8	12779	-7478	373.50	-3449
9	14593	-8662	378.28	-3494
10	16390	-9822	382.94	-3515
12	19999	-12128	398.26	-3572
14	23444	-14321	409.81	-3619
16	26781	-16427	418.39	-3715

Table 4.3: FE-outputs of specimen type 2.

Comparison 5

In section 5.1, a comparison of the FE-model of chapter 4 and the strain gauge results in section 3.4.2 are presented. To ensure the established FE-model is validated, results must coincide with the acquired strain gauge results. As the FE-model is validated, it is utilized to convert the displacement amplitude-life data, acquired from Schenk 400 kN in section 3.4.1, to strain-life data, which is compared to the analytic curves of section 2.3 in section 5.2. Recall from chapter 2, no analytic model for butt-welded specimen is presented, and the models are expected to differ from experimental data, though it is desired to investigate to what extend, and whether the difference is negligible. In addition, stress-life data is established to evaluate whether the method of [1] is compatible for butt-welded specimen in section 5.3. In addition, a study investigating the effect of varying R ratio is presented in section 5.4, as some deviations have occurred during testing. The four sections of this chapter, and the microstructure study of section 3.7, are utilized as a foundation for the discussion and conclusion, presented in chapter 6 and 7, respectively.

5.1 Finite Element Model vs Strain Gauge Data

Validation of the model is a necessity to ensure accurate results are provided. The model is validated by principal strains, determined by the strain gauge data in section 3.4.2, as these provide reliable comparison as misalignment of strain gauges are negligible. The major strain; principal strain 1 along the x-axis, and the minor strain; principal strain 2 along the y-axis, of the FE-model, and corresponding strain gauge data at coinciding displacement amplitudes are utilized for comparison. A major and minor strain plot is utilized to validate the FE-model, presented in figure 5.1, containing data of FE-model and strain gauges. Upon evaluating the data it is important to distinguish specimen type 1 and 2 due to their difference in geometry.

Initially, it is desired to provide strain gauge results, containing a larger displacement span, however, due to the complications and errors mentioned in section 3.3.2, the strain gauge data is limited. The strain gauge results differ from the FE-data, though within an acceptable margin. The strain gauge data for 3 and 4.5 mm, which is for specimen 42, deviates beyond this margin and are evaluated to do so due to the specimen being subjected to displacements before these readings. Consequently, the FE-model is not compatible with these data points. The FE-model is accepted, it is utilized in section 5.2 and 5.3 to convert displacement amplitude-life data to strain- and stress-life data, respectively.

In addition, the force output of Schenk 400 kN and reaction forces of FE-model is compared. It is evident that noticeable deviations are present, see figure 5.2.

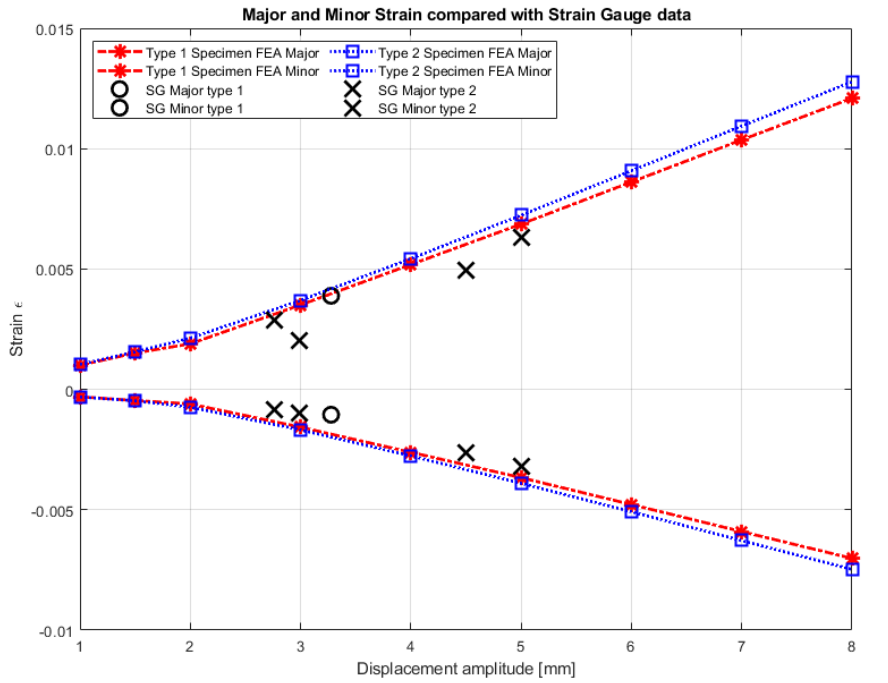

Figure 5.1: Displacement amplitude-strain of 1st reversal, containing major and minor strains of both FE-model and strain gauge data.

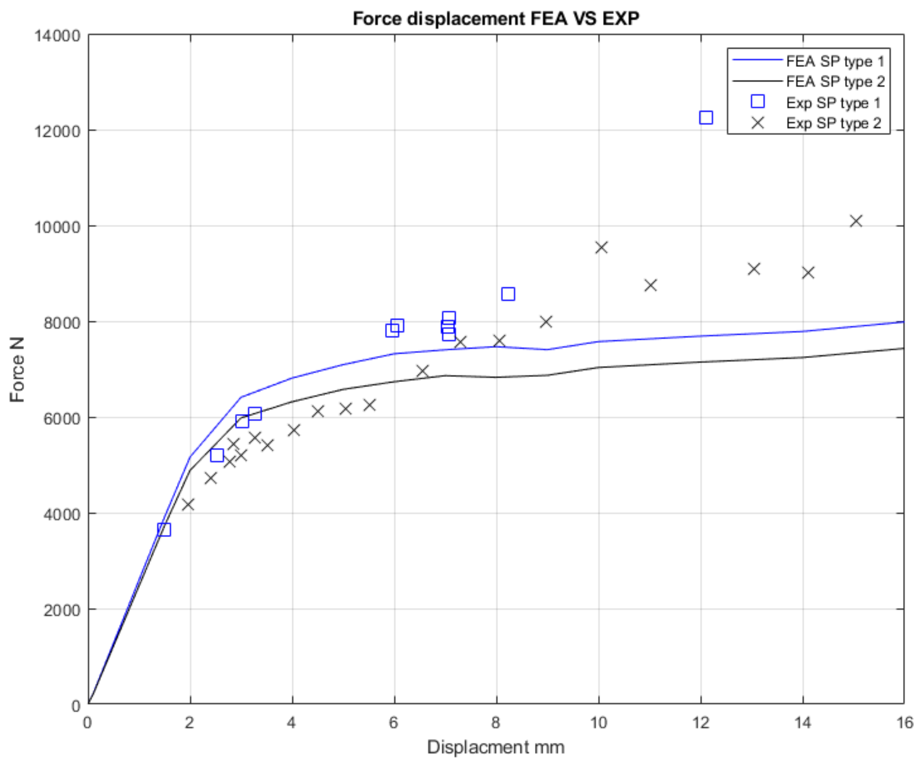

Figure 5.2: Comparison of force-displacement output between FE-model and experimental data.

The force-displacement output especially deviates at larger force magnitudes, which is deemed to be due to a poorly defined material model in the FE-software, or erroneous force control. The considerable deviations in force readings led to an investigation of the load transducer, by evaluating applied weight and corresponding force measurements. However, no errors in force readings are observed. In addition, the position control of the hydraulic cylinder is investigated and no errors are observed. These investigations resulted in an assumption of wrongful configuration of the PID controller, which could account for deviations in force and possibly the noise encountered during force control.

5.2 Analytic Models vs Experimental Data

In this section, the four analytic approaches in section 2.1 are compared to experimental data, which is converted through the FE-model enabling a strain-life comparison. In order to convert the data, the results of the FE-model are interpolated linearly using the displacement amplitude with respect to stress and strain, respectively. To determine the equivalent strain, the results of the FE-model presented in section 4.4 are utilized according to [26]. The three approaches BH1, BH2 and FP are not based on welded specimen. The remaining analytic model of section 2.2.2, SN1, is based on simple monotonic approximations. Consequently, none of the four analytic models are expected to coincide with obtained experimental data. However, if a relation exist, it would be advantageous to investigate, as three of the four analytic models are based on monotonic and hardness material properties. The process of obtaining properties such as ultimate tensile strength σ_{ut}, Young's Modulus E and Brinell hardness BH, are significantly less time consuming than obtaining fatigue properties. Since the presence of a weld is detrimental to fatigue life, the analytic models, based on non-welded specimen, are expected to overestimate the butt-welded fatigue data.

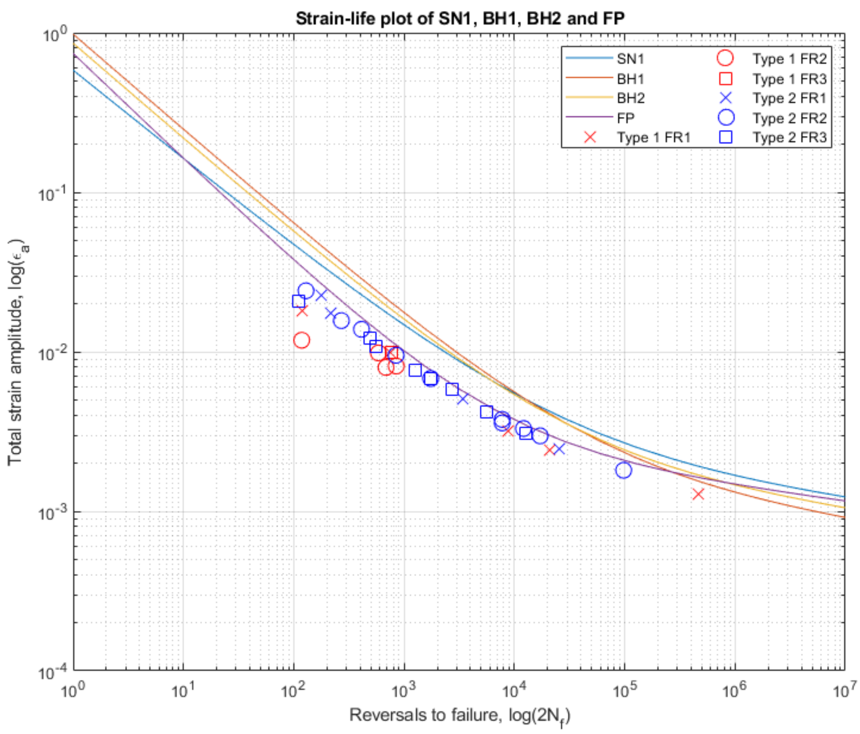

Figure 5.3: Strain-life graph of analytic curves and converted experimental data.

The four analytic curves, and the experimental data converted by the FE-model, are presented in figure 5.3. Data based on type 1 and 2 specimens are presented, with red and blue makers, respectively. In addition, the different failure regions are investigated in section 3.6. Consequently, the specimen data in figure 5.3 is further divided into failure regions; FR1, FR2 and FR3 marked with X, □ and O, respectively.

It is evident from figure 5.3, the analytic curves overestimates the fatigue life as expected. However, a correlation in the behavior of the experimental data and the analytic curves are obvious; if the curves are shifted, they fit the experimental data quite well. The best fitting analytic model is where fatigue material properties are determined from non-welded specimen; article [6]. None of the analytic models are modeled for butt-welded structures, consequently it is quite surprising that the experimental data observed is in close proximity to the analytic models. However, an overestimation of fatigue life time across all models are still observed, which correlates well with the test specimen being welded, and further pertain geometric stress concentrations and pearlite bands.

5.2.1 Regression of Experimental Data

In addition to comparing the experimental data points to the analytic methods, a regression of the data is conducted with respect to the BMC and SWT models. The regression yield an estimation of the fatigue variables pertaining to the two models. The strain data of both models are split into elastic and plastic strain, subsequently a power law fit; ax^b is performed on both. Through the power law fit, expressions for elastic and plastic strain for the BMC model is acquired; equation 5.1. Note, the coefficient of determination R^2 is provided for both power law fits. The results are utilized to evaluate the fatigue variables of the BMC and SWT approach; listed in table 5.1. Specimen 5* and 12* are subjected to load control, and are, consequently, excluded in the regression as these limit the accuracy.

Regression for the BMC model excludes the possibility of incorporating a varying reversal ratio, and consequently the experiments with a displacement ratio between $-0.9 \geq R \geq -1.1$ are not utilized in the fit.

$$\begin{aligned} \varepsilon_e &= \sigma'_f E^{-1}(2N)^b \quad \rightarrow \quad 0.0021(2N)^{-0.0284} \quad R^2 = 0.7526 \\ \varepsilon_p &= \varepsilon'_f (2N)^c \quad \rightarrow \quad 0.5053(2N)^{-0.5695} \quad R^2 = 0.9918 \end{aligned} \tag{5.1}$$

The SWT approach is incorporating the reversal ratio R through the variable σ_{max}, and in order to enable regression, the force ratio is utilized to determine the mean stresses σ_m. This further enables the regression to be performed on elastic and plastic parts of the SWT expression, displayed in equation 5.2. Through regression, the variables a and b of the power law are utilized to determine fatigue parameters; listed in table 5.1.

$$\begin{aligned} \sigma_{max} E \varepsilon_e &= (\sigma'_f)^2 (2N)^{2b} \quad \rightarrow \quad (1.9291 \cdot 10^5)(2N)^{(-0.0561)} \quad R^2 = 0.8072 \\ \sigma_{max} E \varepsilon_p &= \sigma'_f \varepsilon'_f E (2N)^{c+b} \quad \rightarrow \quad (3.3448 \cdot 10^7)(2N)^{(-0.5492)} \quad R^2 = 0.9487 \end{aligned} \tag{5.2}$$

The regression fit for the BMC approach and SWT approach are displayed in figures 5.4 and 5.5, respectively. The two models yield a reasonable fit to the experimental data, however, deviations for both approaches are observed in a life of $2N_f = 10^2$ to 10^3, which coincides with the largest observed scatter in experimental data. Evaluating the coefficient of determination R^2, low-cycle plastic region has the best fit.

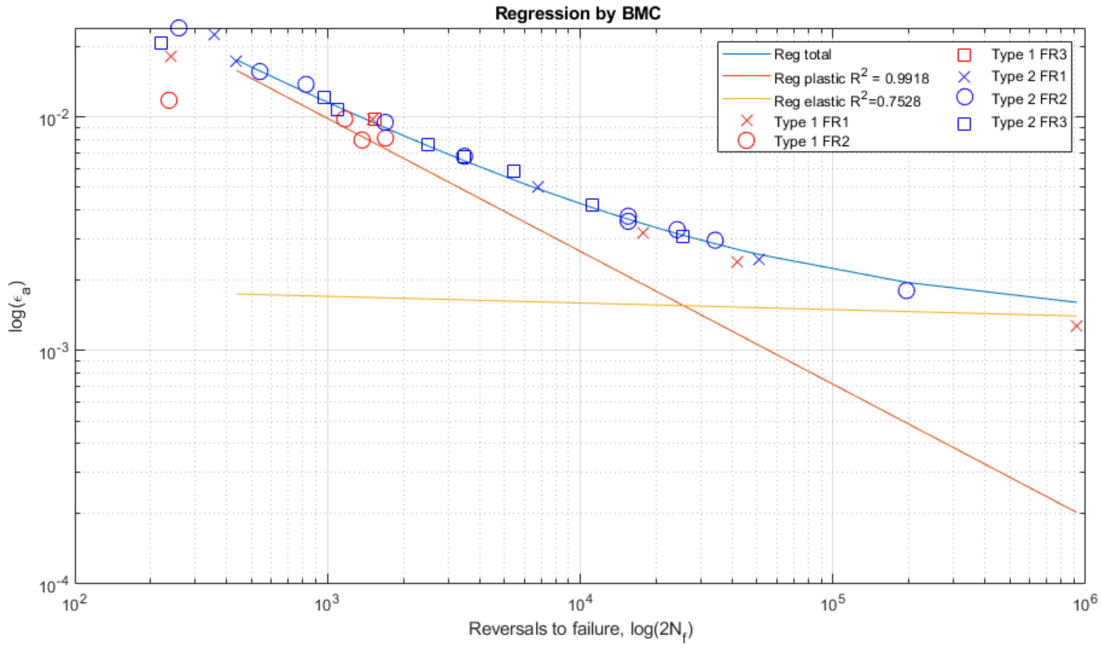

Figure 5.4: Data points and BMC curves by regression of data.

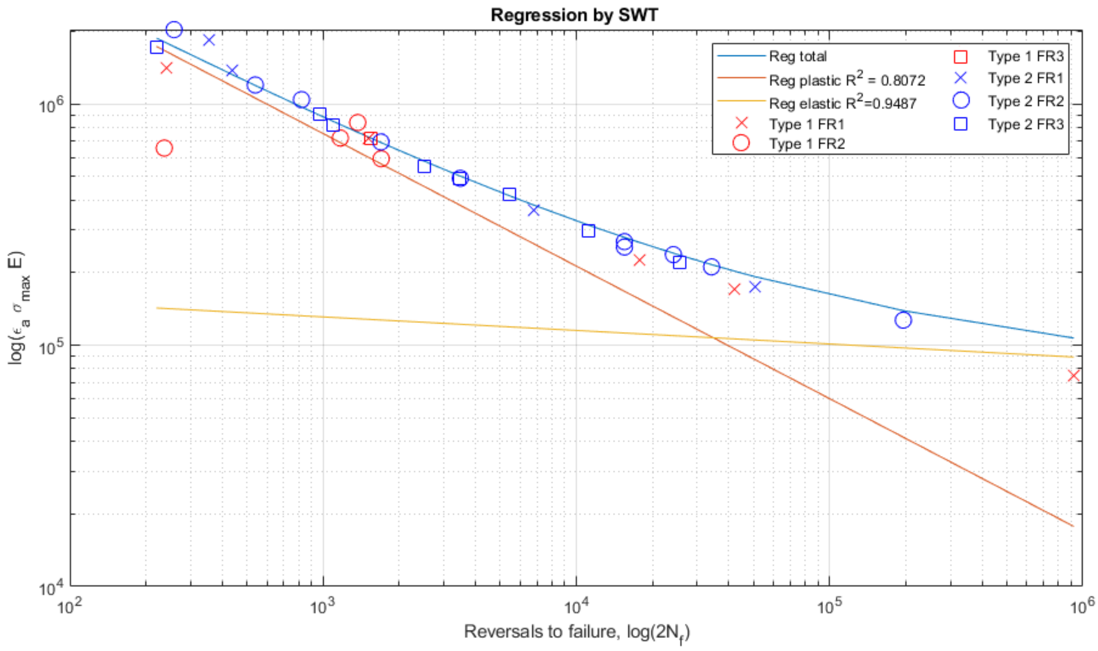

Figure 5.5: Data points and SWT curves by regression of data.

The obtained fatigue values determined by regression, displayed in table 2.2, are compared to values determined in section 2.3 and displayed in table 5.2 for convenience.

Regression		
	BCM	SWT
σ'_f	411.7	439.2
ε'_f	0.5053	0.3844
b	-0.0284	-0.0280
c	-0.5695	-0.5212

Table 5.1: Fatigue variables of the BCM and SWT approach, obtained through regression.

Analytical approaches				
	SN1	BH1	BH2	FP
σ'_f	840.82	959.1	981.5	952.2
ε'_f	0.9776	0.85555	0.57775	0.7371
b	-0.099	-0.099	-0.09	-0.089
c	-0.6	-0.6	-0.56	-0.664

Table 5.2: Tabular comparison of fatigue properties of the four analytic approaches SN1, BH1, BH2 and FP.

Major differences are present for all fatigue properties with the exception of the fatigue ductility exponent c. The value of the fatigue strength exponent b deviates by a factor of approximately 3.5 from the analytic determined values, which could be due to the data. Few data points are within the elastic region, which affects the determination of b during regression. In addition, the fatigue strength coefficient σ'_f is affected by the lack of data within the elastic region as well. The obtained fatigue ductility coefficient ε'_f, deviates substantially, and the obtained value of 0.5053 indicates a brittle material behaviour [14]. This is deemed likely to be a consequence of the geometric stress concentrations and pearlite bands.

5.2.2 Fatigue Stress Concentration Factor

In addition to the curves based on regression, a fatigue stress concentration factor K_f is analyzed. In section 2.1.4, K_f is determined to 1.3, while the FE-model estimates a factor of 1.2. The K_f based on the FE-model is most likely lower due to the fillets of 2 mm, which the analytic approach excludes. Evaluating the data with respect to the determined K_f, the data approaches the analytic curve FP. This could be an indication of why the specimen fail in, or in the vicinity of, the roundings, as the strain and stress is concentrated in this region even though a large radius is utilized. In general, if the strain state increases for a given life N, it approaches the analytic curves, though a $K_f > 1.3$ is deemed unlikely due to the established radius.

5.3 Stress-Life Comparison

In addition to the developed strain-life data presented in section 5.2, it is desired to convert the acquired experimental data to stress-life data, through the FE-model. The result is presented in figure 5.6, where the converted data is presented along the S-N approach, SN2, proposed by [1] in section 2.2.2. The converted data is, as for the strain-life data, divided according to specimen type and failure region.

Upon comparing the data to the S-N approach by [1], most data points for approximately $2N < 10^3$ follows a slope similar to SN2. However, a change in slope occurs hereafter. The data follows this slope until $2N \approx 10^5$, at which a drop similar to the SN2 approach after $2N = 3 \cdot 10^3$. The difference in stress range values could be a consequence of a poor material model, in which the provided stress at a certain life is incorrect.

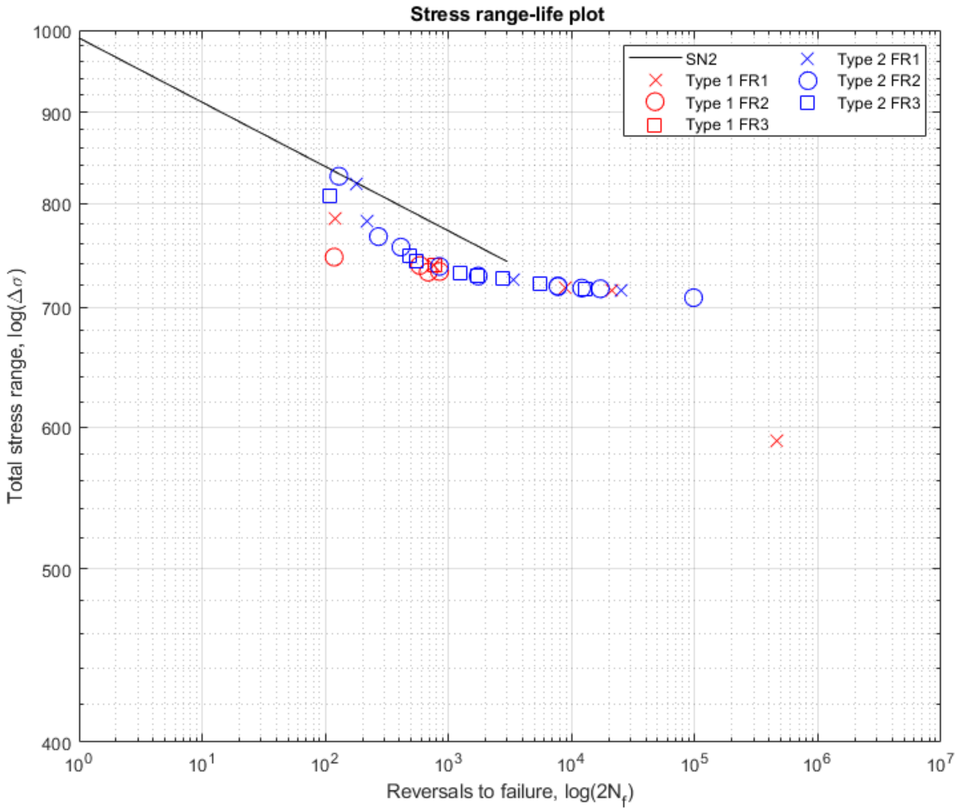

Figure 5.6: S-N curve of data and analytic approach by [1].

5.4 Study of Reversal Ratio

A brief study investigating the effect of a varying R ratio is conducted. In table 3.1, the force ratio $R_F \neq -1$, and deviates with up to ± 0.20. Consequently, it is desired to acquire an understanding of the effect of $R \neq -1$ and how it could influence the acquired experimental data. Initially, load control is desired, however, as explained in section 3.2.2, during the experiments a disconcerting noise ensued from the Schenk 400 kN when utilizing load control. In addition, a peculiar displacement amplitude is observed. Consequently, only two experiments are conducted with load control; specimen 5* and 12*. The remaining experiments are conducted with displacement control and utilizing the observed displacement amplitudes d_a, presented in table 3.1, and the displacement ratio R_d is essentially -1.

As a consequence of $R_F \neq -1$, $F_{max} \neq -F_{min}$, which is evident in figure 5.7, R of force, displacement and strain gauge data is presented. Observing R_d, the majority of specimen pertain an ideal ratio of ≈ -1. Two significant spikes occur, which is for specimen 5* and 12*; the two specimen utilized for load control. If observing R_F, the scatter is noticeable, which illustrates the difference in the obtained force experimental values, which initially is evaluated to be caused by slippage in tool and machinery. Especially the rotational joints, and possible loose bolts, are deemed to affect the ratio, causing a difference between displacement and force ratio. Consequently, the ratio of strain gauges are investigated, which indicates that the conducted tests are not fully reversed.

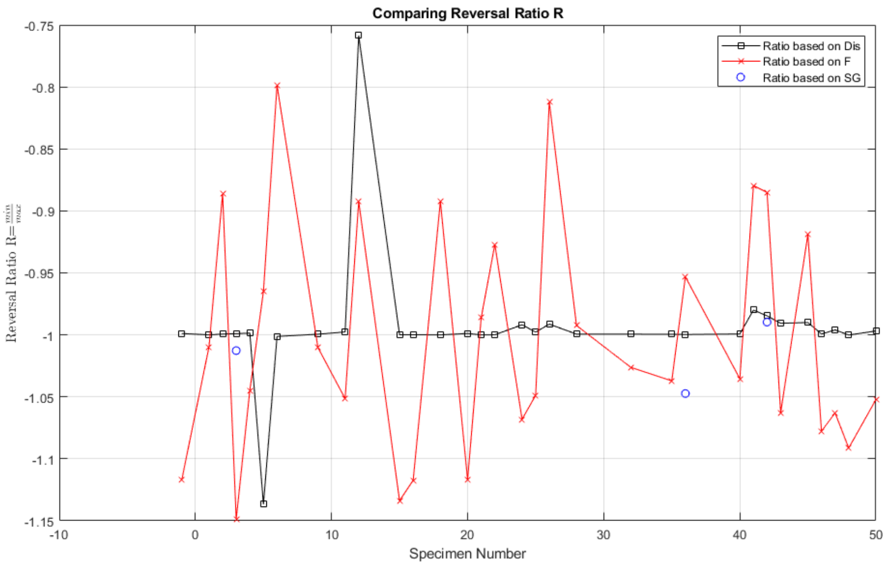

Figure 5.7: Reversal ratios from experiments based on force, strain gauge and displacement.

If $R \neq -1$, mean stresses are present during testing. Consequently, it is desired to investigate the effect of mean stress on the fatigue life by utilizing the SWT model of section 2.1.3. To evaluate the effect, results of the FE-analysis is utilized along with experimental data to obtain stress and strain. To utilize SWT, mean stresses are determined from mean displacements, which are based on R_F and corresponding displacement amplitude. Based on this scheme, mean stresses are determined based on various R-values; -0.5, -0.8, -1, -1.2 and -1.5. The resulting SWT approach for varying R-ratios is depicted in figure 5.8. The effect of mean stress is noticeable, however, when evaluating the presented curves in the LCF region, the mean stress has little effects compared to the HCF region. Considering the maximum variation observed in the experiments is a R_F of ± 0.2, the effects of mean stress has little influence on fatigue life of this project in relation to other factors.

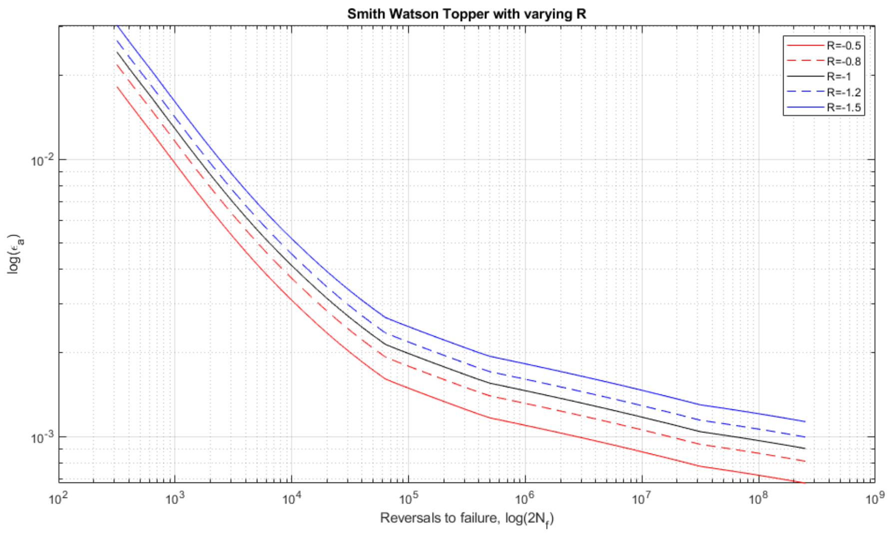

Figure 5.8: The SWT approach with varying R-ratio.

Discussion 6

Initially, it is desired to determine the material properties of the utilized material; S355J2 . However, no batch of material is available and consequently it is necessary to utilize material properties determined by [25]. This is an undesired situation, as whether the determination of material properties is correct, or some undocumented errors occurred which are not accounted for. It is always preferable to conduct these test to ensure desired data is acquired. This could be an explanation of the erroneous implementation of material data in FE-software, even though this ultimately is overcome. In addition, whether the observed pearlite bands are present in the tested material is unknown. Consequently an investigation of anisotropy is of interest.

In addition, it could be beneficial for the study to perform a second study in which a new specimen are manufactured. As a result of ill-defined geometries of specimen type 1 in section 1.1.1, the dimensions of the specimen differ. Consequently, each specimen is subjected to a slightly different load. In addition, as documented in section 3.6, a significant number of specimen are failing at the region of the roundings, FR1 and FR2. This deemed to be due to geometric stress concentrations, which are highly undesired as specimen are not failing in weld, HAZ or base material due to cyclic loading, but are failing due to the geometric stress concentrations. Consequently, this renders the data acquired undesired. If a second study is conducted, it would, in addition to material, be beneficial to define a new geometry to decrease geometric stress concentrations and to ensure identical dimensions for across all specimen.

In section 3.6, a third failure region FR3 is defined, which is not affected by geometric stress concentrations, but rather the microstructure of the base material, S355J2. The microstructure at FR3 contains multiple pearlite bands across the width of the specimen, which results in a brittle region, where failure is more prone to occur. The fracture surfaces; FS1, FS2 and FS3 further document the observed microstructure discoveries. FS3 occur at FR3, where what is interpreted as a brittle fracture has occurred. FR1 and FR2 experiences predominantly FS1 and FS2, which could correspond to a lesser amount of pearlite, possibly none, at these regions. This could possibly account for the specimen failures, however, due to the presence of pearlite and possible geometric stress concentrations, the data acquired might be undesired, as it does not provide an accurate depiction of the fatigue life of a butt-welded S355J2 specimen. If a second study is conducted, with a new material, the data of this study could be compared to investigate the effects of possible geometric stress concentrations and pearlite bands.

The FE-model of the study is based on a single reversal load scenario; a static structural analysis. The FE-model is validated in section 5.1, as the principal strain acquired by the FE-model coincides with the principal strain determined based on the utilized rosette gauges. The principal strain accounts for possible misalignment, though a possible misplacement of the gauge can not be accounted for. The FE-model measures the strain at a specific node, or element, defined by user, while the mounting of rosette gauge at similar location on specimen can be troublesome for several reasons. Small misplacements could occur due to physical measurements utilizing a caliper, while the exact location of the gauges in the rosette gauge will not coincide with the probed element in FE-model due to the physical size of the gauges.

Initially, data of the Schenk 400 kN, e.g. force, is deemed misleading and erroneous as it does not coincide with the reaction forces of the FE-model. The malfunctioning load control option indicates this and could perhaps be an explanation for some of the data in section 3.4.1, where specimen 21 and 24 at displacement amplitude of 14 and 15 mm pertain a greater lifetime than specimen 6* at displacement amplitude 12 mm. This is especially noticeable, as 21 and 24 are of specimen type 2. However, this could be an indication of errors in the FE-model as well, as the utilized material model by [25] could be erroneous. This led to a brief testing of Schenk 400 kN, at which static known loads are applied and the force should correspond, as described in section 5.1. Furthermore, besides comparing force of Schenk 400 kN and reaction force of the FE-model, the force ratio R_F is investigated, where $R_F \neq$ -1. If R_F is not -1, it can influence the utilized models, not to mention the established FE-model. However, as displacement control is utilized, the displacement ratio R_d is utilized. The displacements, however, coincide almost perfectly, consequently resulting in $R_d \approx -1$. The strain ratio R_ε determined by strain gauges is deviating by ± 0.05, which is deemed sufficient. However, as none of the ratio R are exactly -1, mean stresses are present. Consequently, the effect of mean stress at different R-values are investigated in section 5.4 by the SWT model. In the study, the effect of R and mean stress is clear, though negligible with respect to the determined R-values of this study.

In section 5.2, the comparison of the established analytic strain-life curves and acquired experimental data is presented. The models do not correspond to the data, however, this is expected as none of the established curves are based on welded specimen. In addition, two of the models are based on hardness measurements, which is a conversion of HRC and HRB to HB. In general, the conversion of hardness introduces errors, while accuracy of the measurement equipment is questionable. The measurements acquired differ significantly at certain points, and the determined hardness should consequently be utilized with caution. Consequently, the hardness utilized for BH1 and BH2 could be misleading, providing curves which overestimates the fatigue life. The SN1 curve, which is based on simple approximations for fatigue properties based on monotonic properties, behaves similarly to the curves of BH1 and BH2. Most interestingly, the curve FP actually coincides quite well with respect to the acquired data, which initially is not expected. This could be due to the aforementioned failure regions; FR1, FR2 and FR3, which all are located in the base material. The model could coincide well due to the specimen failing in base material, and not in the HAZ nor the weld, thereby yielding acceptable results. FP does predict a higher strain-life curve than the experimental data, which is similar for the other analytic curves, which could be due to the pearlite band or geometric stress concentrations. If the fatigue stress concentration factor K_f of 1.3 is applied, the FP curve fits almost perfectly with the experimental data, even with different material properties. The FE-model provides a K_f of 1.2. Consequently, the results will not fit perfect, though this is to be expected. In addition, it should be noted that some sort of safety factor would be implemented if an analytic model is to be utilized to determine the fatigue life.

In addition to the analytic strain-life curves, the experimental data is converted through the FE-model to stress-life, in section 5.3, to investigate whether the proposed model of [1] is applicable. The model coincides well with the acquired data, however, the knee drop observed in [1] occurs at a lower life cycle than for the specimen of this study. This might be a consequence of the failure regions, as the base material rather than the HAZ or weld is failing. If a fatigue stress concentration factor K_f of 1.2 is applied, the data fits the line of [1] better, though the slope of the data is still not satisfying. Some revisions are probably necessary if to describe the S-N curve of the material by this model.

Conclusion 7

As mentioned previously, the main objective of this study is to investigate LCF behavior of full penetration butt-welded steel specimen, and investigate different analytic models ability to predict fatigue life in the LCF region. This succeeded to some degree, however, several errors detrimental to the obtained fatigue results are present and therefore the main objective is not fulfilled.

Firstly, material for tensile testing have not been available, resulting in relying on work conducted by [25]. The material properties are deemed inaccurate based on the force-displacement study, though deviations in obtained forces could also be a result of slippage, due to wear in the tool. Consequently, new tensile tests are desired to ensure material properties are determined appropriately. In addition, repair of the four point bending tool is desired.

A new batch of material is desired, as the presence of the pearlite bands are observed. The presence of pearlite introduces a brittle region in the material, and is deemed to significantly interfere with acquired experimental results. If cross rolling could be implemented, this could mitigate the anisotropic effects of pearlite bands. However, a new material batch is desired in order to limit the presence of pearlite bands.

A newly defined geometry is necessary, as the geometric stress concentrations, introduced by roundings, are interfering with the acquired results. In addition, geometry of the specimen differs due to ill-defined geometry during manufacturing, thereby affecting the data.

It is concluded that a second study, with altered specimen dimensions and material batch, must be initiated, as failures of the specimen are not due to pure cyclic loading, but rather cyclic loading in collaboration with geometric stress concentrations and flaws in microstructure.

Experimental results utilizing strain gauge are obtained, where utilization of principal strains is deemed necessary to account for misalignment, though the determined angular misalignment is negligible. The obtained results approximately coincides with the established FE-model, and deviations are deemed due to ill-defined geometry and strain gauge user error.

In addition to errors introduced by misalignment and placement of rosette gauges, the Schenk 400 kN introduces errors due to slippage. Based on R_d and R_ε, the tests are deemed fully reversed, though according to the force ratio R_F, the tests are not fully reversed, as F_{min} and F_{max} differ. Consequently the effects of mean stresses are addressed through the SWT approach. However, the study determined that the deviations in R have minor effects in the LCF region.

The analytic models and curves presented in this study are evaluated with respect to the experimental data. In general, the models overestimates the fatigue life of the specimen in this study, as expected from the addition of a butt-weld. However, specimen fatigue failure is not observed at the welded region, but rather in regions with stress concentrations and pearlite bands. Consequently, the models are expected to overestimate the experimental data.

The strain-life approach, FP [6], has the best fit out of all models investigated, despite the approach being for a non-welded S355 specimen, which has different material properties, and consequently different fatigue properties. The difference in fatigue properties, in relation to the regression study, suggests the experimental data being more conservative than FP. As the fatigue ductility and fatigue strength coefficients are significantly reduced in relation to article [6]. Furthermore the presence of geometric stress concentrations and pearlite bands, should indicate even more conservative experimental fatigue results, in relation to FP. Though FP only slightly overestimate the obtained experimental results.

The strain-lifes approaches based on hardness measurements, BH1 and BH2, overestimates the fatigue life severely. This is deemed a consequence of inaccurate hardness measurements and a brittle behavior of the steel due to pearlite bands and geometric stress concentrations, resulting in a conservative fatigue life. Due to the presence of the pearlite bands, the hardness approach is deemed impractical for the utilized material.

Out of all analytic approaches, only the approach by [1] is for welded specimen, and in [1] is able to yield accurate predictions of fatigue life for a different type of weld; a T-joint with an existing weld toe. The strain-life approach, SN1, deviates, as BH1 and BH2, which also are based on approximations of monotonic material properties. The S-N approach, SN2, of [1] overestimates fatigue life in the LCF region, and experimental results of this study are conservative due to geometric stress concentrations and pearlite bands. Consequently, the S-N approach is deemed able to predict the S-N behavior of the specimen in the LCF region, though new tests are necessary to confirm it. For the new tests, new specimen with mitigation of stress concentrations and removal of pearlite bands is implemented. Furthermore if any analytic model is utilized for determining fatigue life in real life structures, certain safety factors must be applied to ensure the desired fatigue life, which even further yield fatigue predictions closer to the S-N approach of [1].

8 Future Work

In this chapter, subjects for possible future work and research is presented. Optimal experimental results are not acquired in this study, which is evident when evaluating the fracture surfaces and failure regions of the specimen. The specimen are concluded to fail due to stress concentrations and pearlite bands, resulting in wrongful LCF data. Consequently, a new geometry of specimen and material batch is necessary to investigate the LCF behavior of butt-welded steel specimen. Furthermore, the geometry of all specimen must be identical to ensure compatible data.

New tensile tests are necessary, as the material data provided by [25] is not deemed reliable. The tensile test is to be conducted for several tensile test specimen manufactured at different orientations, in relation to the rolling direction, to ensure material is not anisotropic. In addition, these tests could indicate whether pearlite bands are present in the new material batch, and further investigate consequence of pearlite bands on material properties.

As new material is acquired, an improved FE-model can be established, which is evaluated to correspond better with the displacement-force data of Schenk 400 kN. Furthermore, though a monotonic FE-model is deemed sufficient, it is of interest to conduct a fatigue analysis in a FE-context.

Upon manufacturing new specimen, new LCF data can be obtained. By utilizing regression, new fatigue properties are determinable, which is based on specimen failing due to the weld, and not of stress concentration and microstructural flaws. The data can be compared to the analytic models. New approximations for the fatigue properties of welded specimen might even be introduced.

However, before conducting any new fatigue tests, the four point bending tool provided by Aalborg University must be repaired. Slippage occurs in the tool, which is detrimental to the acquired data. In addition, the machine Schenk 400 kN should be serviced with respect to the load control option.

Besides future work of this study, an investigation of the occurrence of pearlite bands in steels should be initiated by researchers. This microstructural phenomena is occurring in steel for the pipeline industry according to [9], however, the frequency of occurring pearlite bands is unknown to the authors of this study at this point. Consequently, a study regarding effect of hot rolling on microstructure would be beneficial.

Bibliography

[1] Schjødt-Thomsen J. & Andreasen J.H. *Low Cycle Fatigue Behaviour of Welded T-Joints in High Strength Steel*, Engineering Failure Analysis, vol. 93, (2018) 38-43

[2] Bruce E. Boardman *Crack Initiation Fatigue - Data, Analysis, Trends and Estimation*, SEA Transactions , vol. 91, (1984) 2312 - 2326

[3] M. L. Roessle, A. Fatemi *Strain-controlled fatigue properties of steels and some simple approximations*, International Journal of Fatigue , vol. 22, (2000) 495 - 511

[4] D. Pedersen, S. Hedegaard, Schjødt-Thomsen J. & Andreasen J.H. *Investigation of low-cycle fatigue behavior of welded T-joints.*, AAU Mechman , vol. -,

[5] A. Hvatov, C.S. Ahle, D.N. Pedersen, D.R. Andreasen, R. Stengaard, S. Hedegaard *Investigation of the low-cycle fatigue behavior of welded T-joints in high strength steel*, 3rd Symposium on Mechanical and Manufacturing Engineering, Aalborg University

[6] Abìlio M.P. de Jesus, Rui Matos, Bruno F.C. Fontoura, Carlos Rebelo, Luis Simôes da Silva, Milan Veljkovis *A comparison of the fatigue behavior between S355 and S690 steel grads*, Journal of Constructional Steel Research, 2012, Vol. 79, pp. 140-150

[7] Chaminda S. Bandara, Sudath C. Siriwardane, Udaya I. Dissanayake, Ranjith Dissanayake *Full range S-N curves for fatigue life evaluation of steels using hardness measurements*, International Journal of Fatigue, 2016, Vol. 82, pp. 325-331

[8] Zhenming Li, Qigui Wang, Alan A. Luo, Penghuai Fu, Liming Peng *Fatigue strength dependence on the ultimate tensile strength and hardness in magnesium alloys*, International Journal of Fatigue, 2015, Vol. 80, pp. 468-476

[9] M. S. Joo, D.-W Suh, H. K. H. Bhadeshia. *echanical Anisotropy in Steels for Pipelines*, International Journal of Fatigue, 2013, Vol. 53, number 8, pp. 1305 - 1314

[10] Robert D. Cook & David S. Malkus & Michael E. Plesha & Robert J. Witt *Concepts and Applications of Finite Element Analysis*, John Wiley & Sons, 2015, 4th Edition

[11] William D. Callister, jr & David G. Rethwisch *Materials Science and Engineering*, John Wiley & Sons, 2015, 9th Edition

[12] Materials Science and Engineering *Metal Fatigue in Engineering*, John Wiley & Sons, 2001, 2nd Edition

[13] Robert L. Norton *Machine Design: An Integrated Approach*, Pearson Education, Inc., 2014, 5th Edition

[14] Yung-Li Lee, Jwo Pan, Richard Hathaway, Mark Barkey *Fatigue Testing and Analysis: Theory and Practice*, Elsesvier Inc., 2005

[15] Serope Kalpakjian, Steven R. Schmid, K. S. Vijay Sekar *Manufacturing Engineering and Technology*, Pearson Education, Inc., 2014, 7th Edition

[16] James M. Gere, Barry J. Goodno *Mechanics of Materials*, Cengage Learning, 2009, 9th Edition

[17] Ole Ø. Mouritsen *Basic Uncertainty Evaluation by Measurements using strain gauges*, Department of Mechanical and Manufacturing Engineering, Aalborg University, 2013, 1st Edition

[18] Karl Hoffmann *An Introduction to Stress Analysis and Transducer Design using Strain Gauges* , HBM,-, 1st Edition

[19] Erik Lund & Esben Lindgaard *Notes for course on Finite Element Methods*, Aalborg University, 2018

[20] Erik Lund *Course: Engineering Optimisation - Concepts, Methods and Applications*, Aalborg University, 2018

[21] R. Mikael Larsen *Course: Materiallære*, Aalborg University, 2015

[22] Jan Schjødt-Thomsen *Course: Continumm Mechanics*, Aalborg University, 2015

[23] TML *Course: Continumm Mechanics*, Tokyo Measuring Intruments Laboratory Co., Ltd., 2019, *Published:* https://www.tml.jp/e

[24] Sharcnet *Abaqus Analysis Manual*, 2018, *Published:* https://www.sharcnet.ca/Software/Abaqus610/Documentation/docs/v6.10/books/usb/default.htm, Located: 14-03-2019

[25] Robin Krogh Olesen & Mads Guldbæk Poulsen, *Non-linear Assessment of Non Full-Strength Welded Joints*, 2018, *Published:* https://projekter.aau.dk/projekter/files/281139767/Non_linear_Assessment_of_Non_Full _Strength _Welded_Joints_2209A.pdf, Located: 13-03-2019

[26] TNO DIANA BV. *Equivalent Von Mises Strain*, 2012, *Published:* https://dianafea.com/manuals/d944/Analys/node405.html?fbclid=IwAR015Tpf8PFeZNOm_ -h6T-9aTnetLyUNv3n1-Edr9jwTi73-OiUSGRMijNw, Located: 06-05-2019

[27] MIT.edu *Eight-node brick element (C3D8 and F3D8)*, 2014, *Published:* http://web.mit.edu/calculix_v2.7/CalculiX/ccx_2.7/doc/ccx/node26.html, Located: 16-04-2019

[28] MIT.edu *Ten-node tetrahedral element (C3D10 and F3D10)*, 2014, *Published:* http://web.mit.edu/calculix_v2.7/CalculiX/ccx_2.7/doc/ccx/node33.html, Located: 16-04-2019

[29] Erke Wang & Thomas Nelson & Rainer Rauch *Back to Elements - Tetrahedra vs. Hexahedra*, 2004, *Published:* https://support.ansys.com/staticassets/ANSYS/staticassets/resourcelibrary/confpaper/2004-Int-ANSYS-Conf-9.PDF, Located: 06-04-2019

[30] Engineers Edge *Brinell and Rockwell Hardness Conversion Table Chart*, -, *Published:* https://www.engineersedge.com/hardness_conversion.htm, Located: 25-03-2019

[31] Dansk Standard *DS/EN 10025-2*, Dansk Standard, 2004

[32] Dansk Standard *DS/EN ISO 3834-2*, Dansk Standard, 2006

[33] Dansk Standard *DS/EN ISO 5817:2014*, Dansk Standard, 2014

[34] Dansk Standard *DS/EN ISO 10042:2018*, Dansk Standard, 2018

[35] Euripean Committee for Standardization *Eurocode 3*, European Standard , (2005)

Analytic Models A

In this appendix, graphical representation of the models of section 2.3 is presented.

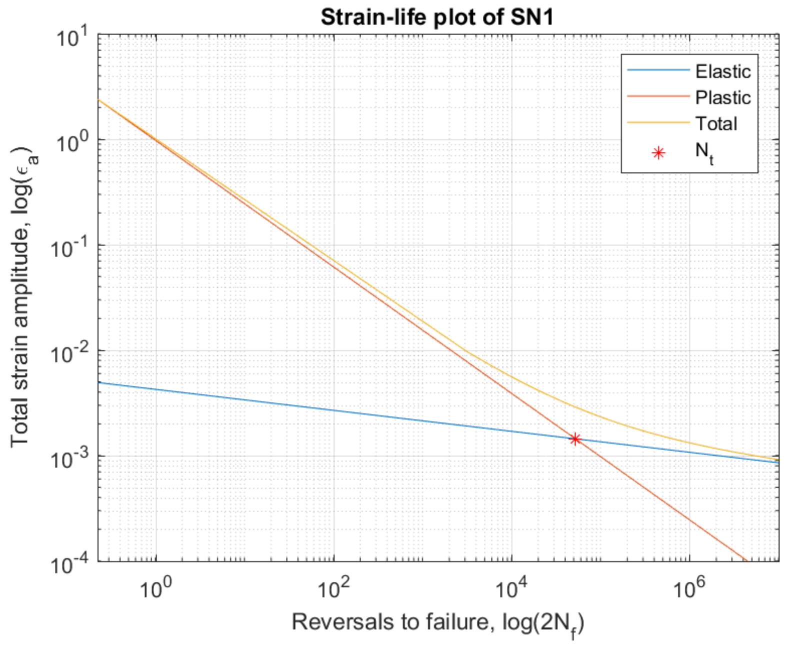

Figure A.1: Total, plastic and elastic strain based on approximations for approach SN1.

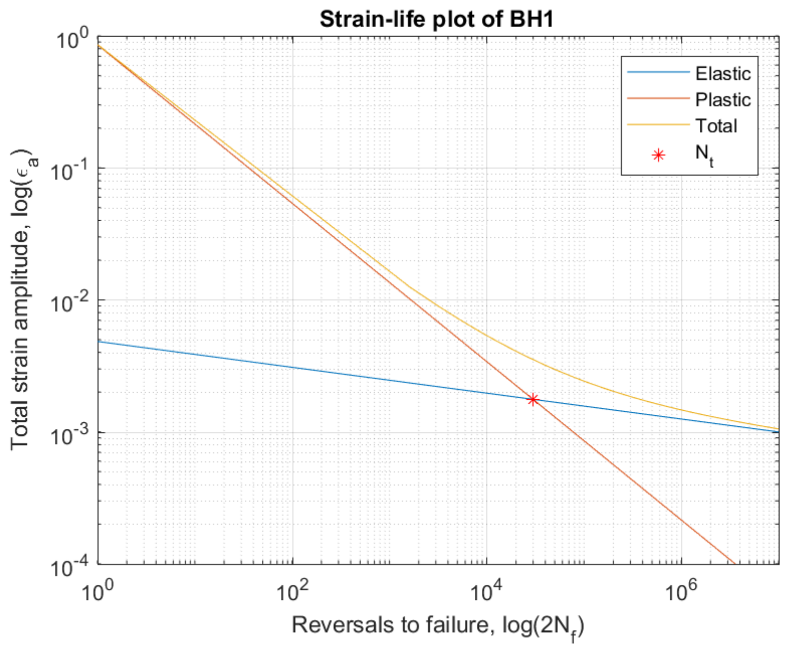

Figure A.2: Total, plastic and elastic strain based on approximations for approach BH1.

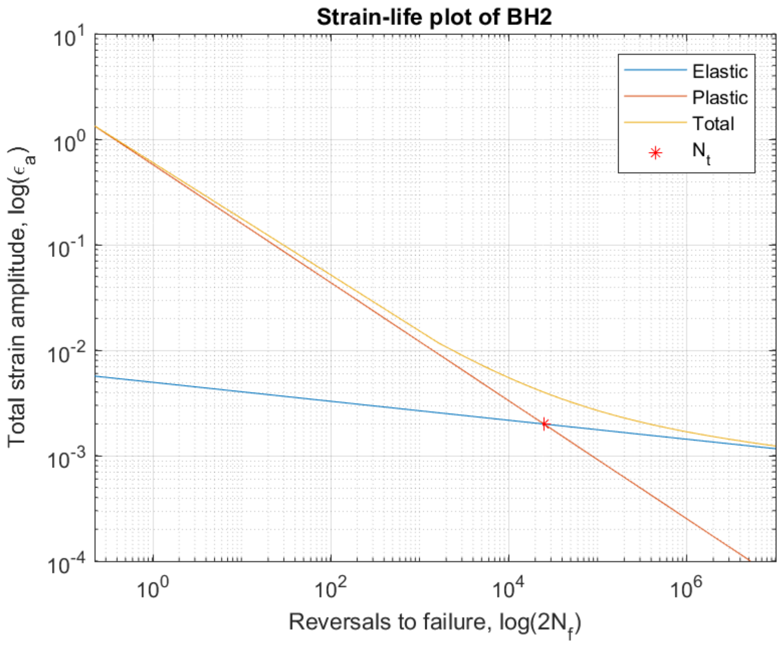

Figure A.3: Total, plastic and elastic strain based on approximations for approach BH2.

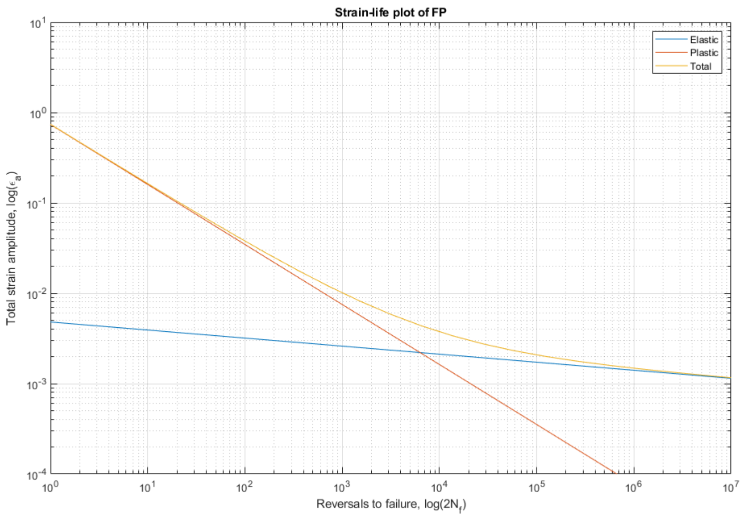

Figure A.4: Total, plastic and elastic strain based on approximations for approach FP.

Brinell Hardness B

This appendix briefly presents the data points utilized in section 3.8. The data points are presented in figure B.1 and table B.1, respectively. Note, "Excluded" refers to certain points being removed due to large deviations. For 14S1 points 16 - 19 are removed, no points are removed for 14S2_1 and point 1 is removed for 14S2. The points in table B.1 correspond to the points in figure B.1 for the given test surface.

	14S1 (HRC)	14S2_1 (HRC)	14S2 (HRB)
1	2.8	3.7	76.1
2	4.6	4.9	87
3	4.4	6.3	87.1
4	4.1	5.5	91.5
5	4.1	4.2	88.1
6	3.8	5.5	88.1
7	4.6	5.5	87.9
8	4.6	5.7	87.3
9	4.9	3.1	89.3
10	5	3.8	89.3
11	5.2	4.5	89.5
12	5	4.2	90
13	4.4	3	90
14	5.1	3.7	89.5
15	4.8	3.7	90.1
16	7.1	3.9	84.9
17	6.7	3.5	NaN
18	7.1	5.3	NaN
19	6.6	5.4	NaN
20	4.9	4.4	NaN
21	4.4	NaN	NaN
22	4.4	NaN	NaN
23	5	NaN	NaN
24	4.7	NaN	NaN
25	3.9	NaN	NaN
26	5.1	NaN	NaN
27	4.6	NaN	NaN
28	4.5	NaN	NaN
29	4.5	NaN	NaN
30	4.9	NaN	NaN
Average	4.86	4.49	87.86
Excluded	4.55	4.49	88.64

Table B.1: Tabular of hardness.

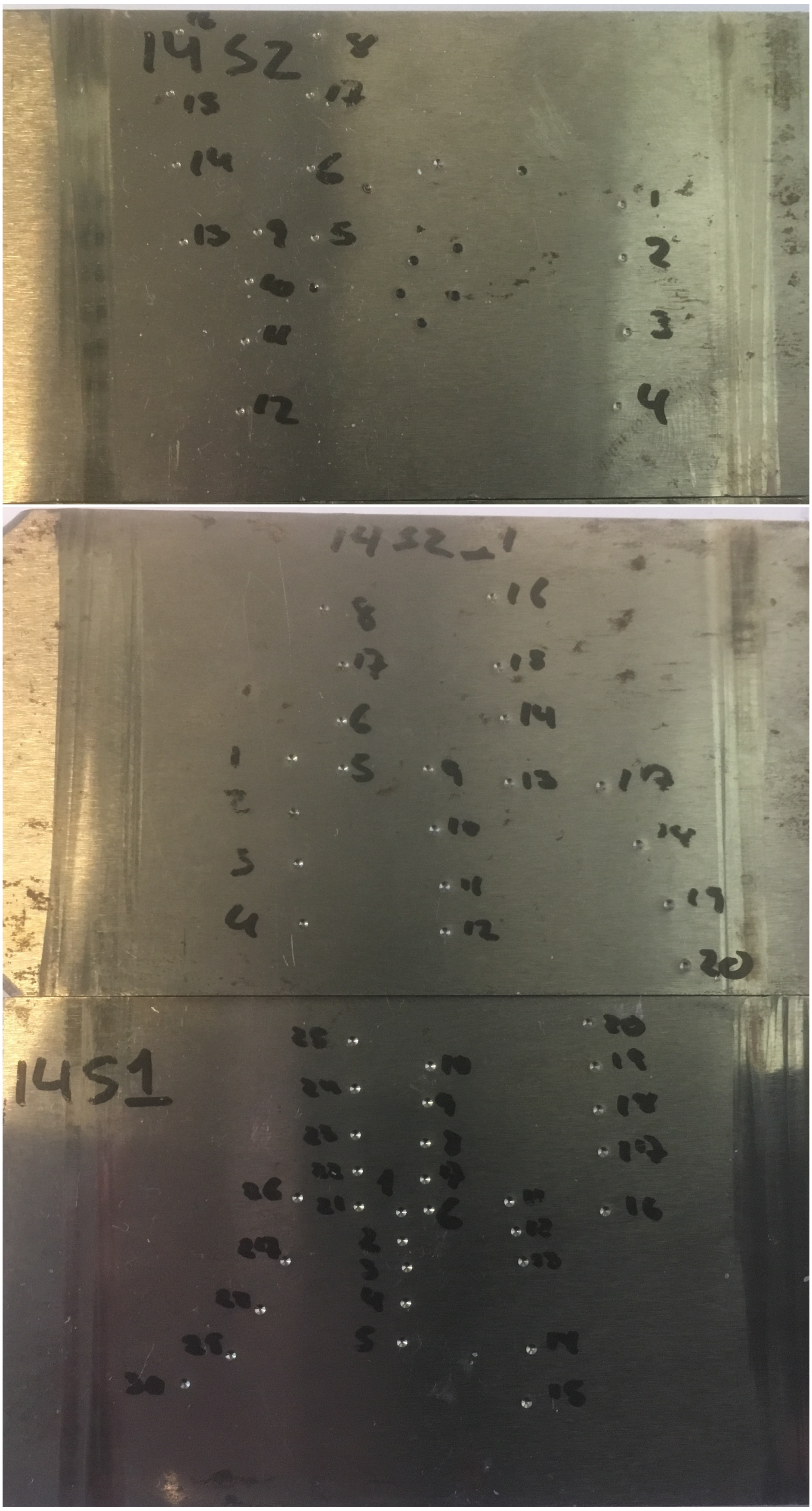

Figure B.1: Hardness measurements of specimen surface.

Standard Deviations of Experimental Data from Schenk 400 kN

C

This appendix presents the acquired results and corresponding standard deviations of Schenk 400 kN. In figures C.1 to C.10 are the measured data along with standard deviations presented.

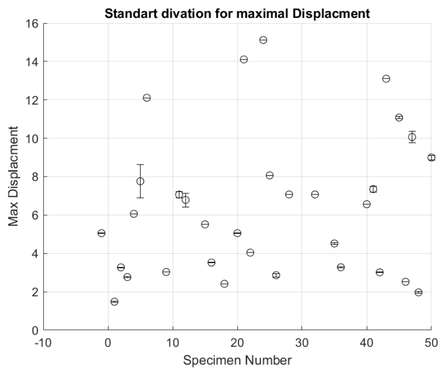

Figure C.1: Standard deviation for max. displacement.

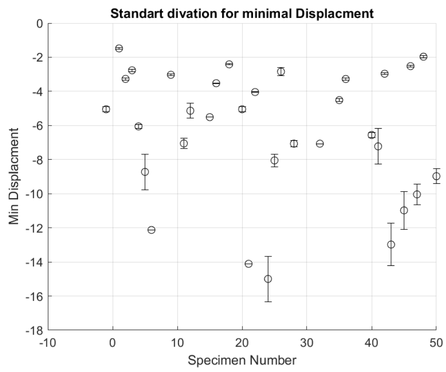

Figure C.2: Standard deviation for min. displacement.

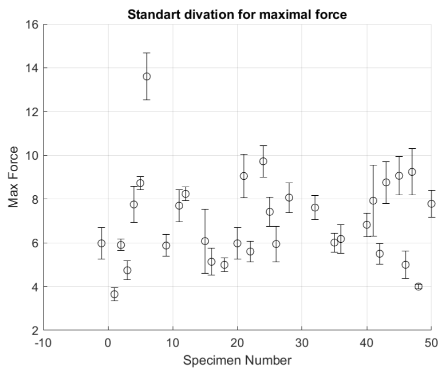

Figure C.3: Standard deviation for max. force.

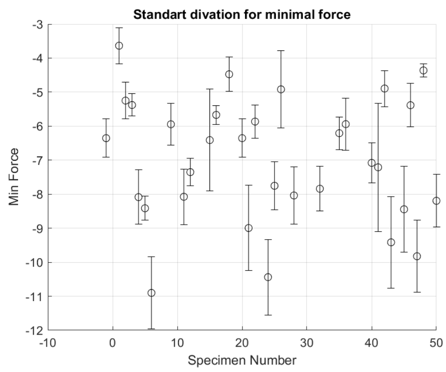

Figure C.4: Standard deviation for min. force.

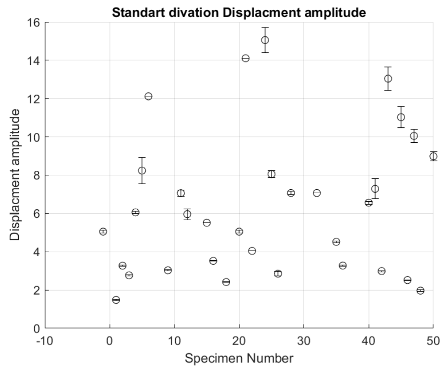

Figure C.5: Standard deviation for displacement amplitude.

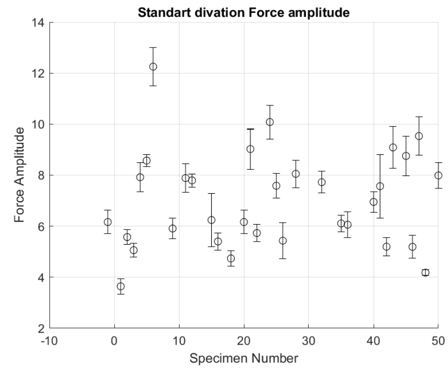

Figure C.6: Standard deviation for force amplitude.

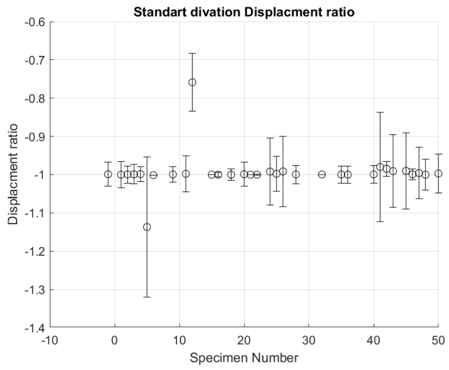

Figure C.7: Standard deviation for displacement ratio.

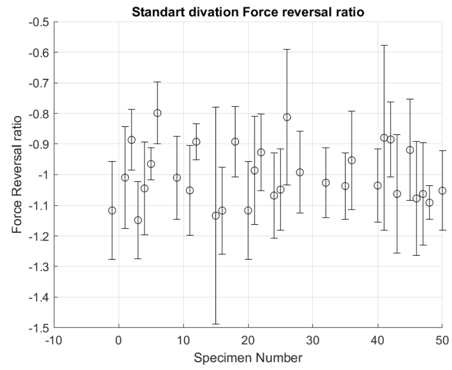

Figure C.8: Standard deviation for force ratio.

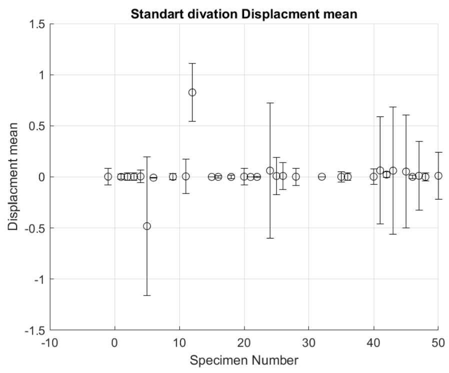

Figure C.9: Standard deviation for displacement mean.

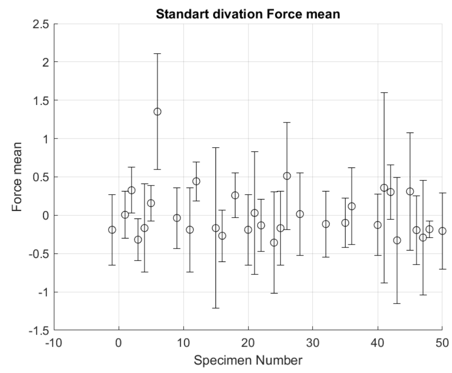

Figure C.10: Standard deviation for force mean.

Four Point Bending Tool D

In this chapter the four point bending tool is presented and described, with respect to parts and assembling. Note, the tool is briefly presented. This is intended to give the reader an improved understanding of the utilized equipment. In figure D.1 all components of the tool are presented, which includes rollers, bolts, rotational joints etc. The rotational joints are presented in figure D.2 in an assembled configuration.

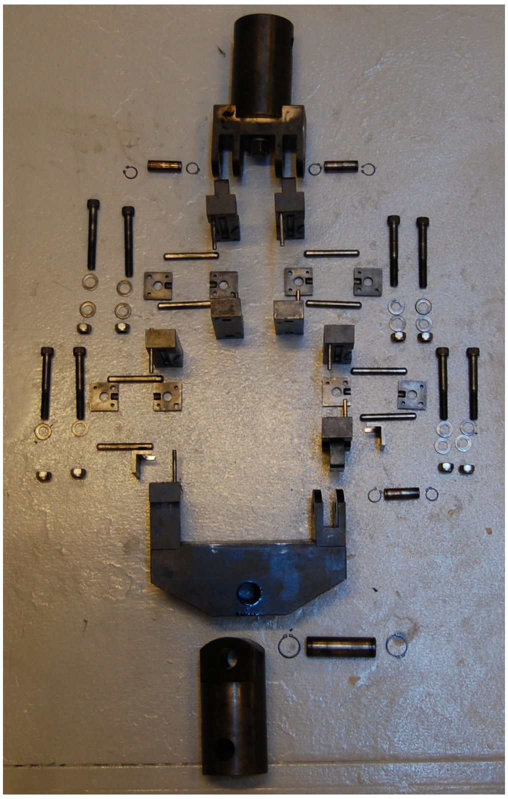

Figure D.1: Disassembled four point bending tool.

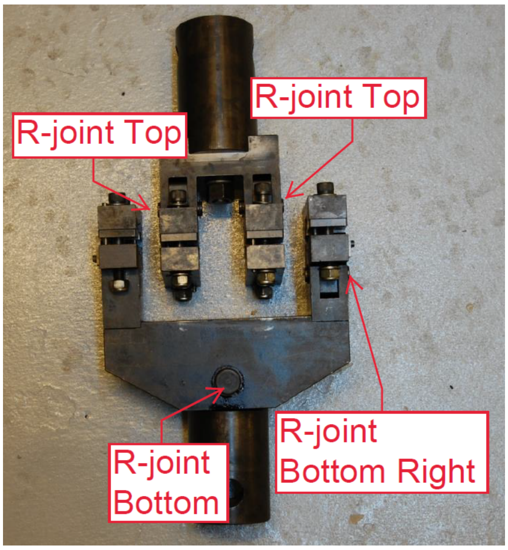

Figure D.2: Tool assembled, with marked R-joints

In figures D.3 and D.4, the rotational joint of the bottom part are presented.

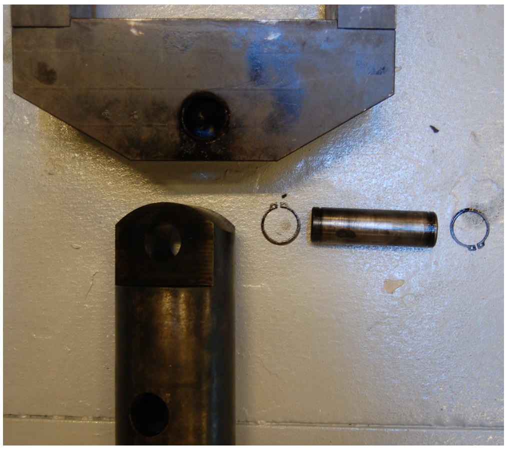

Figure D.3: Lower rotational joint.

Figure D.4: Lower rotational joint.

In the figure D.5 the parts surrounding the bottom right rotational joint is displayed. The clamps, with rollers, of the right side, is identical to the left side, though with exception of the rotational joint. The bottom part assembled without clamps, is displayed in figure D.6, where the rollers and end fixtures that fix the specimen from rotating in the z direction is visible; in the lower left and top right part of part.

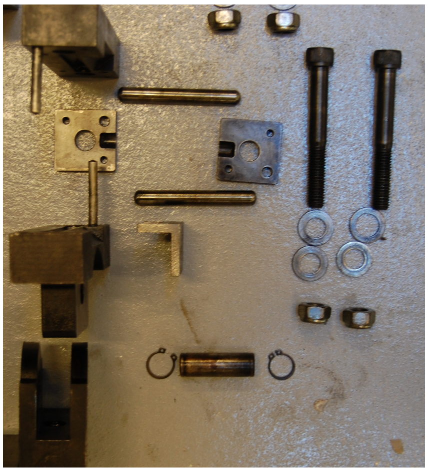

Figure D.5: Bottom right rotational joint, and clamps.

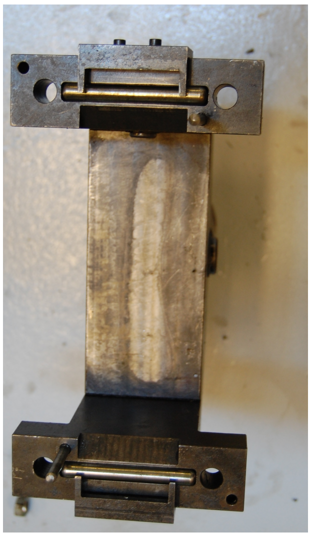

Figure D.6: Lower part without clamps displaying rollers.

In the figure D.7 the disassembled clamps are displayed, which consist of a roller and clamps for the roller. In figure D.8, the clamps with rollers displayed from the right side of the tool without a specimen and main bolts are presented.

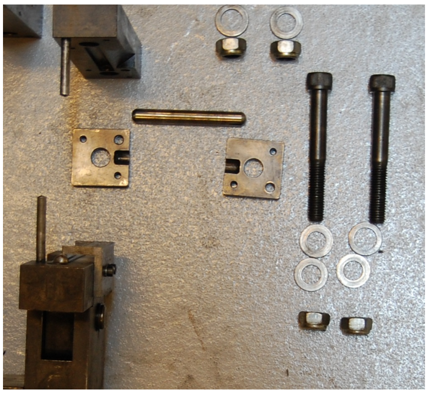

Figure D.7: Disassembled clamps.

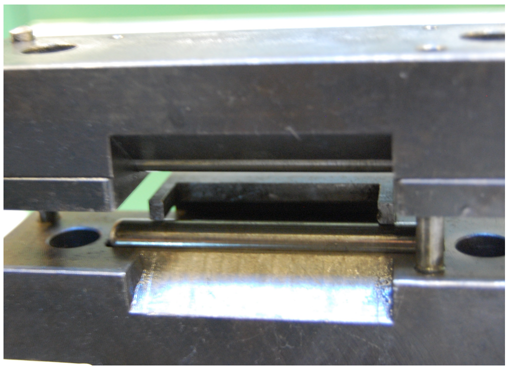

Figure D.8: Side view of clamps and rollers.

The top part of the tool, pertaining the two rotational joints which are attached to the clamps, is displayed in figure D.9. These joints are believed responsible for the major part of the slippage in the tool, consequently newly manufactured rotational joints is desired. The clamps and rollers for the top of the tool, displayed in figure D.10, is identical clamps and rollers of the lower part.

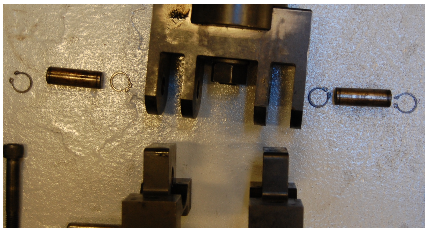

Figure D.9: Top rotational joints.

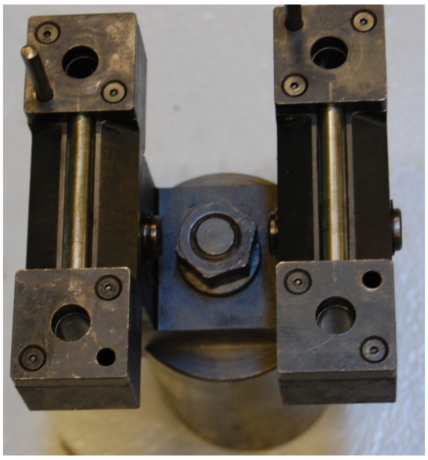

Figure D.10: Clamps and rollers for the top part.

The disassembled and assembled tool is displayed in figures D.11 and D.12, respectively.

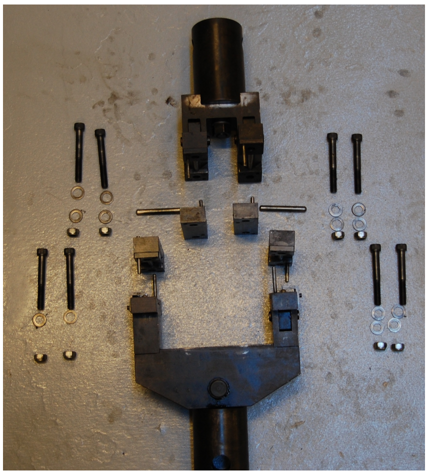

Figure D.11: Disassembled tool.

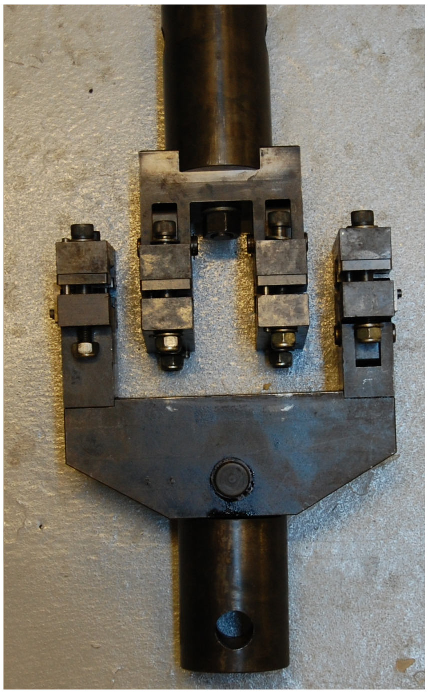

Figure D.12: Assembled tool.